A FIELD DISLOCATION MECHANICS APPROACH TO MODELLING THE INFLUENCE OF MICROSTRUCTURE ON FATIGUE BEHAVIOUR OF NICKEL-BASED SUPERALLOYS

by

JOSEPH RANGEL

A thesis submitted to the University of Birmingham for the degree of

DOCTOR OF PHILOSOPHY

School of Metallurgy and Materials

College of Engineering and Physical Sciences

University of Birmingham

March 2019

Acknowledgements

First and foremost I have to thank my supervisor Professor Hector Basoalto for introducing me to world of dislocation dynamics and crystal plasticity. For many unorthodox yet effective meetings guiding me through the PhD research, he has been a great teacher, mentor and friend throughout, always making time to help me, even when I was on the opposite side of the planet. It has been both an honour and a pleasure to work with you.

Thanks for all the help from my friends and colleagues in the PRISM^2 research group who made the whole experience so enjoyable. A special mention goes to Dr Gavin Yearwood and Dr James Little for their collaboration on the code development as well as their enlightening company for many an hour spent in the office, brought together by dislocations.

I am grateful for the financial support from the Engineering & Physical Sciences Research Council and Rolls-Royce plc giving me the opportunity to undertake this research.

A huge thank you to my partner Dr Eleanor McCance, who has had to live with me and my ongoing PhD research (often through to the early hours of the morning), her constant motivation and relentlessly positive attitude has kept me working. Finally an equally huge thank you to my very supportive and even more so patient family. My mum and dad who have always provided their unwavering support of my studies despite me spending an aeon in higher education, and my brother Dr Cyprian Rangel for blazing the academic trail inspiring me to follow on, providing many words of wisdom and warning about undertaking a PhD. Without all of their love and ongoing support I could never have completed this research.

Contents

List of Figures

Nomenclature

$\underline{\boldsymbol{b}}$	Burgers vector
$\underline{\boldsymbol{t}}$	Tangent line vector
$\underline{\boldsymbol{\tau}}$	Shear stress
$\underline{\underline{\boldsymbol{\Sigma}}}$	Macroscale stress field
$\underline{\underline{\boldsymbol{\sigma}}}$	Microscale stress field
$\underline{\underline{\boldsymbol{g}}}$	Edge dislocation stress field
$\underline{\underline{\boldsymbol{\beta}}}$	Displacement gradient (distortion)
$\underline{\underline{\boldsymbol{F}}}$	Deformation gradient
$\underline{\underline{\boldsymbol{L}}}$	Velocity gradient tensor
$\underline{\underline{\boldsymbol{\alpha}}}$	Dislocation density tensor
$\underline{\underline{\boldsymbol{G}}}$	Green's strain tensor
$\underline{\boldsymbol{B}}$	Total displacement
$\underline{\boldsymbol{u}}$	Displacement field
$\underline{\boldsymbol{v}}$	Velocity field
κ	Dislocation line curvature
$\dot{A}^{+}$	Rate of dislocation generation
$\dot{A}^{-}$	Rate of dislocation annihilation
ν	Poisson's Ratio
M	Mobility
μ	Shear Modulus
Φ_s	Secondary particle volume fraction
Φ_t	Tertiary particle volume fraction
Γ	Line energy

.

Chapter 1

Introduction

Understanding the causal relationship between microstructure and the mechanical response of a material is fundamental in developing stronger alloys with increased operational lifespan. To achieve this aim, physics-based modelling approaches can provide a means of extracting such relations. These modelling methods allow study of variability in deformation and fatigue behaviour with microstructure, and identify potential failure modes to predict lifespan of components. Using these modelling techniques provides the ability to test the physical behaviour for multiple scenarios simultaneously to improve the speed of development for future alloys. Nickel-based superalloys are an important class of materials in aerospace applications due to their high temperature strength arising from their two phase microstructure, this strengthening characteristic is essential to their function. The microstructure of an alloy is not homogeneous and varies throughout the component due to the temperature gradient across it during the forging process, this leads heterogeneous γ' distributions and a mixture of fine grain and coarse grain structures.

Field dislocation mechanics (FDM) is a theory based on dislocation transport where the line defects are treated as a continuous field. It accounts for the combined elastic stress fields of dislocations providing a framework to study the interaction of dislocations with

microstructure over large length scales. The dislocation field is represented by the dislocation density tensor, which describes a discrete dislocation ensemble within the computation domain. The length scale used to describe the dislocation density is key to recreating the correct physical behaviour for the continuum dislocation mobility.

The aims were to firstly inform the FDM model through discrete dislocation interactions, using a discrete dislocation dynamics (DDD) model to determine an accurate scaling of the continuum description. Then validate the governing equation for the transport of the dislocation field derived from the theory. Understand the impact of local stress fluctuations on the FDM model and the impact on slip band development in two-phase microstructures. Predict fatigue behaviour using the FDM approach for temperature dependent microstructures, and identify the correlation between dislocation and γ' interaction, shear events and the stress-strain response.

This study has focused on the prediction of the macroscale response from the development of dislocation slip bands in a microstructure representative of a disc Nickel-based superalloy, based on RR1000. Slip band evolution was studied within a simple computational domain representing a single grain of 5 microns in width, to capture the dislocation behaviour within individual grains with the γ' particles and grain boundaries. The grain boundaries were taken as impenetrable for the simulations. The dislocation interactions with the γ' particles were measured by their domain stress strain response with the evolution of the dislocation field.

To commence, the relevant literature was reviewed focusing on the relationship between the microstructure and deformation mechanics, relevant to two-phase polycrystalline Nickel-based superalloys. Following this, continuum dislocation dynamics models were reviewed to understand the different approaches to modelling continuum dislocation mechanics and their applied scenarios.

The full derivation of the theory is presented in Chapter 3 including a break-down of the different dislocation mobility terms. The field dislocation mechanics theory was derived from Nye and Kroner [1], to form a spatio-temporal transport equation for the dislocation field. Constitutive relations for the dislocation velocities are presented. Following this Chapter 4 explains numerical methods used to solve the transport equation and how the FDM code was integrated into the commercial finite element software. The set-up of the simulation domain, material parameters and how the γ' particles were treated in the model was also covered.

The first set of numerical results looks at the discrete dislocation considerations of the continuum using a discrete dislocation dynamics model. The minimum length scale required for application of the FDM theory is addressed in Chapter 5. This involved simulating the development of discrete dislocation pile-ups and comparing them to analytical solutions [2]. For the length scale determined, the initial FDM simulations were carried out to recreate a continuum dislocation pile-up which was verified by the analytical solutions. The DDD model was also used to investigate how the dislocation configuration within the density can be accounted for. The rate term for annihilation of dislocations in the transport equation was characterised using DDD simulations over the scale of the dislocation density.

The second set of results in Chapter 6 implement the full FDM model coupled with the finite element software for two unimodal γ' particle distributions based on Nickel-based superalloy microstructure. Simulations investigate the stochastic nature of the field dislocation stress fields. The local stress fluctuations caused by different dislocation configurations were characterised using DDD simulations to create probability distribution functions. Adapted FDM simulations added the local stochastic dislocation stress fluctuations into the stress field calculations using a scalable probability distribution function. Comparison was made

between simulations with and without the stochastic stress fluctuation term to see the difference in dislocation density distributions and the influence on the flow stress for the unimodal γ' particle distributions.

The final set of numerical results in Chapter 7 investigate the causal relationship between the microstructure and fatigue behaviour using the field dislocation mechanics approach. Three temperature dependant microstructures, representative of those found in Nickel-based superalloy turbine discs, were simulated using several heterogeneous particle distributions at each temperature. Cyclic fatigue behaviour was compared using the peak stresses and the plastic strain range. The asymmetry due to initial load direction was investigated. The findings of the FDM fatigue model temperature dependant microstructures were discussed and compared to experimental results. Finally Chapter 8 reviews the conclusions from the development of the FDM model presented in this research. The limitations of the theory and implementation are discussed, as are improvements for the FDM model.

Chapter 2

Literature review

The relevant literature is explored in two parts. Initially looking at Nickel-based superalloys intended for the field dislocation mechanics model, understanding their microstructure and deformation mechanics to guide model requirements. The second part looks at existing continuum dislocation dynamics models to understand the current mathematical approaches and their model assumptions.

The high temperature turbine section of the engine is located just after the combustion chambers of the turbine, see Figure 2.0.1, the hot compressed air passes through the turbine blades driving the engine. The materials which form the blades and discs components, that experience the maximum engine temperature and stress, are composed of Nickel superalloys. These alloys are designed to give high-temperature creep resistance, high yield strength and fracture toughness. The alloy systems of interest in this study are Nickel-based superalloys used in the discs which hold the high pressure turbine blades. The discs are subjected to a range of temperatures (approximately 700°C to 900°C) and low cycle fatigue loading. Design requirements are to reduce engine weight and increases rotation speed, this increases the stress on the disc thus alloy development is focused on increasing yield stress and inhibiting crack initiation and growth [3].

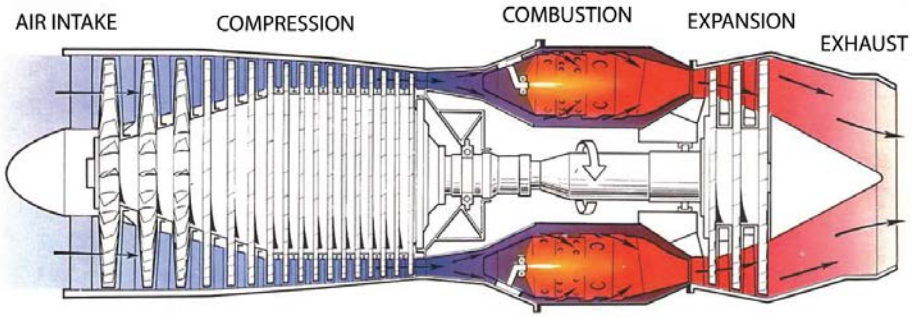

Figure 2.0.1: Illustration of a Turbojet engine [4]

2.1 Composition and microstructure

All Nickel superalloys stem from the Ni-Al-Ti-Cr precipitation strengthened alloy, Nimonic 80A. This was developed at the Mond Nickel company as a suitable turbine blade material for the first British gas turbine for aircraft propulsion [3]. The Nickel superalloy consists of a face-centred-cubic γ-matrix interspersed with γ' particles, which has a primitive cubic structure, these are shown in Figure 2.1.1. The γ' precipitates in disc alloys come in a range of sizes referred to as primary, secondary and tertiary to describe the sizing groups in descending order which have been obtained by multi-stage heat treatments. The two-phase microstructure is key to strengthening the material [5]. Aluminium increases the volume fraction of the γ' precipitates. Elements cobalt, aluminium, titanium and molybdenum act as solid-solution strengtheners in both the γ and γ' phases [6].

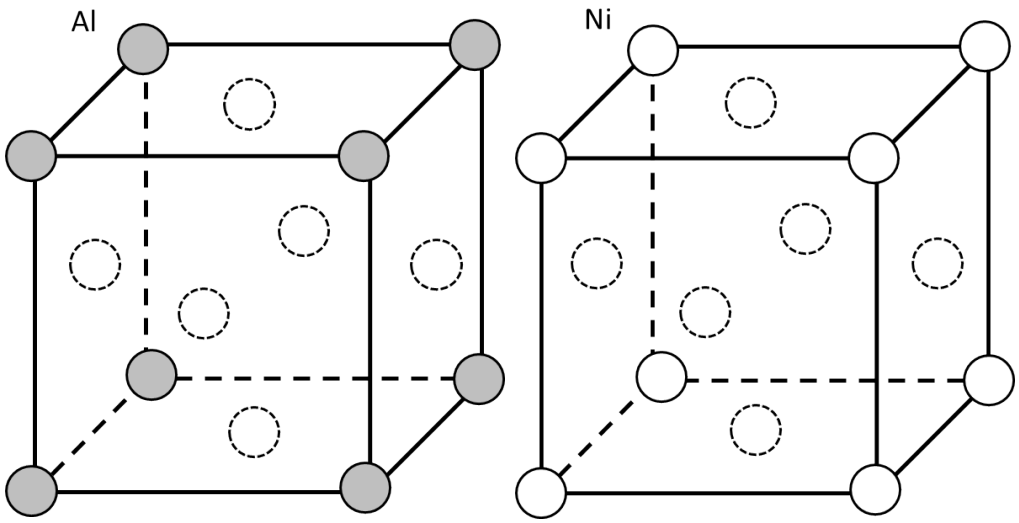

(a) L_{12} ordered structure of precipitates (b) FCC structure of γ matrix

Figure 2.1.1: FCC crystal structures of Nickel-based superalloys

Precipitate distributions are controlled by heat treatments which are carried out whilst forging the alloy. During processing these precipitates can vary across the disc due to the temperature gradient across it. The heat treatments determine the size distribution and volume fraction of the precipitate particles. It also determines the grain size in the polycrystalline alloys. The control of grain size is an important factor in the high temperature mechanical behaviour of superalloys. Crystals nucleate and grow at random orientations and their size is dependent on the orientation of neighbouring grains. Yield strength and resistance to fatigue is known to increase with decrease in grain size [7, 8], as the grain boundaries act as obstacles to dislocation motion. For resistance to creep grains need to be larger, but fatigue behaviour deteriorates with increased size [9], this demonstrates how alloy microstructure has to be optimized for its purpose. The high temperature single crystal turbine blades microstructure designed to resist creep using a large grain size and closely packed, seen in Figure 2.1.2. The fine grain size of the polycrystalline alloy of the disc to resist fatigue crack growth, seen in Figure 2.1.3, which operate at lower temperatures and high stress where fatigue is the life limiting property.

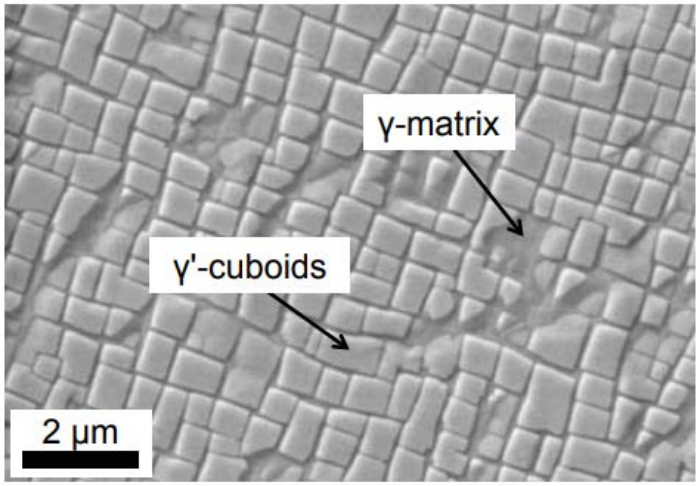

Figure 2.1.2: Example of single crystal precipitate particles [10]

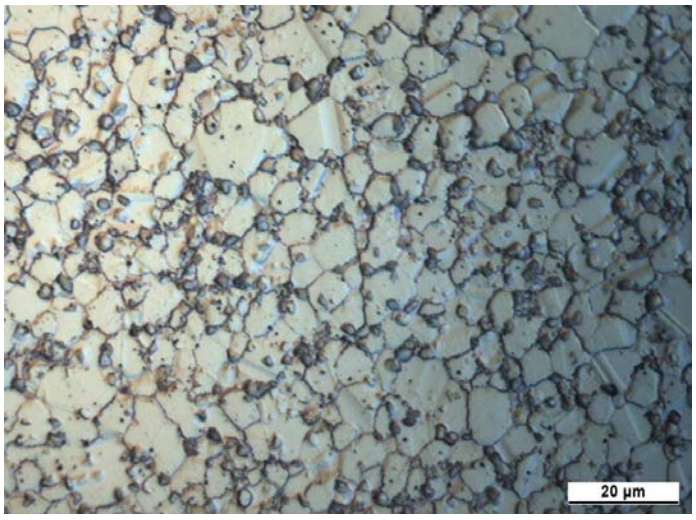

Figure 2.1.3: Example of fine grain microstructure of RR1000 [11]

Elements to form MC carbides and M_3B_2 borides are introduced to strengthen the grain boundaries at elevated temperatures. Their formation at the grain boundaries prevents grain-boundary sliding and increases the creep strength [6].

2.1.1 γ' precipitates

The γ' precipitates add strength to a material by acting as obstacles to dislocation movement. They have an ordered $L1_2$ type structure which requires increased energy for dislocations to shear these particles during deformation. Heat treatments are designed to control the γ' size distribution by controlling nucleation and growth of these precipitates. Turbine blades have a very high γ' volume fraction which are cuboidal in morphology, see Figure 2.1.2. Within a turbine disc the morphology of the precipitates can vary with composition, lattice misfit and processing heat treatments. The γ' precipitates can take a range of shapes including spherical, cuboidal or octodendritic seen in Figure 2.1.4. Given the size of a disc component, the temperature gradients across it during heat treatments, mean the γ' morphology varies within the component.

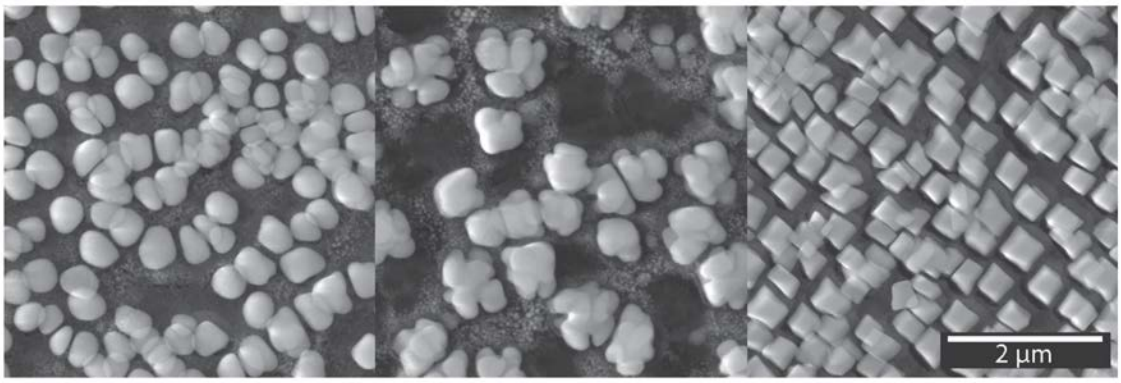

Figure 2.1.4: Examples of γ' precipitate morphology, spherical (left), octodendritic (centre) and cuboidal (right) [12].

Multi-stage heat treatments result in multi-modal distributions, as seen in Figure 2.1.5. There are large primary γ' particles (typically of size 1-5 μm) which form at the boundary of grains. Then there are the secondary particles (radii of 50 to 200 nm), which form within the γ matrix of the grains, and then the smaller tertiary particles (radii of 5 to 25nm), each forming at different solvus temperatures. Given that γ' form as a result of heat treatments, the morphology of the alloy can change as operation temperatures increase. At high tem-

peratures the particles are observed to coarsen and drop in volume fraction, and tertiary particles dissolve into the matrix, shown in the right hand column of Figure 2.1.5. This diffusion-controlled coarsening of the multimodal precipitate distribution occurs at elevated temperature because smaller precipitates, with a higher surface area to volume ratio, coarsen to form larger particles in lower volume, lowering the energy of the system [13].

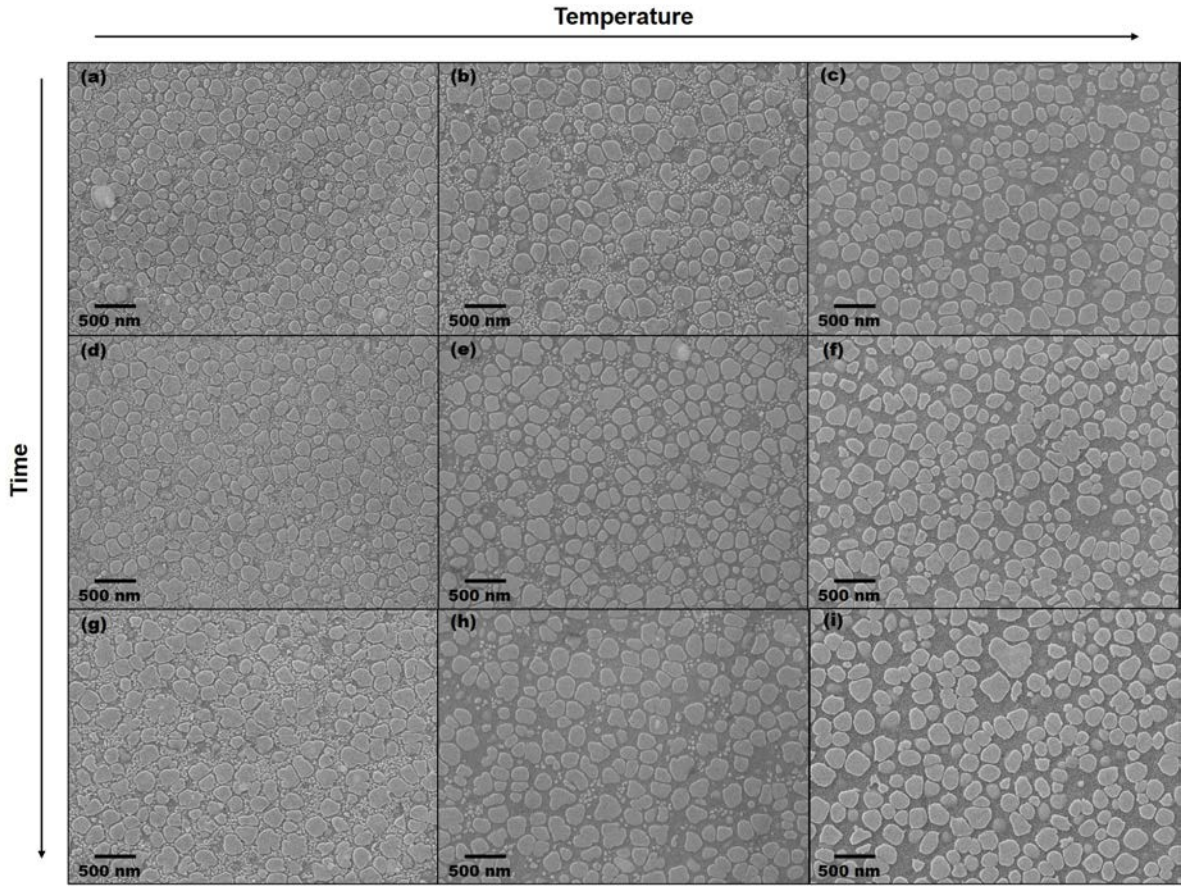

Figure 2.1.5: Images detailing the coarsening of particles with temperature over time for RR1000 [14].

2.2 Deformation mechanisms

When the material experiences sufficient stress it deforms due to changes happening at the microscale. A brief overview of the basic deformation mechanisms will now be presented.

Starting with the dislocations, their motion and interactions with the microstructure, then expanding onto their larger scale influence as they begin to group and form structures. A dislocation is a line defect bounding an area along a periodic crystal lattice that has slipped by an amount $\underline{\boldsymbol{b}}$, which is the Burgers vector. Such a domain introduces a discontinuous displacement field, such that the contour integral of the dislocation displacements leads to a non-closure condition. This is illustrated in Figure 2.2.1 for the case of an edge dislocation. The dislocation line has two characters; the edge dislocation where the Burgers vector is perpendicular to the line of the dislocation along the slip direction, and the screw dislocation where the Burgers vector is parallel to the line of the dislocation. The edge dislocation can be positive or negative depending on the location of the extra half plane is above or below core location respectively. The screw dislocation twists the lattice such that half of the domain above the screw dislocation slips parallel to the line of the dislocation.

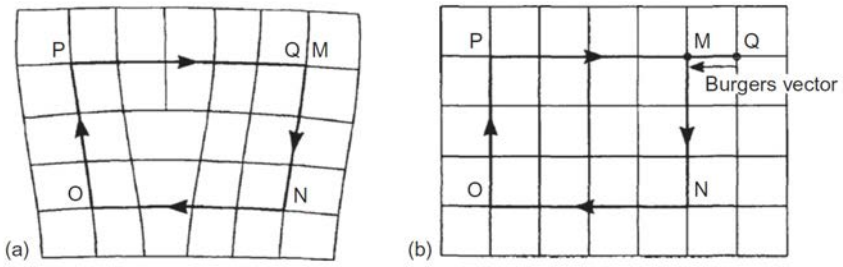

Figure 2.2.1: An edge dislocation in a lattice surrounded by a Burgers circuit (a) with same circuit in perfect crystal showing the failure to close as the Burgers vector (b) [15]

2.2.1 Dislocation motion

In face centred cubic (FCC) materials the dislocations are confined to moving along the {111} slip planes. Figure 2.2.2 shows an example of a {111} slip plane in an FCC structure.

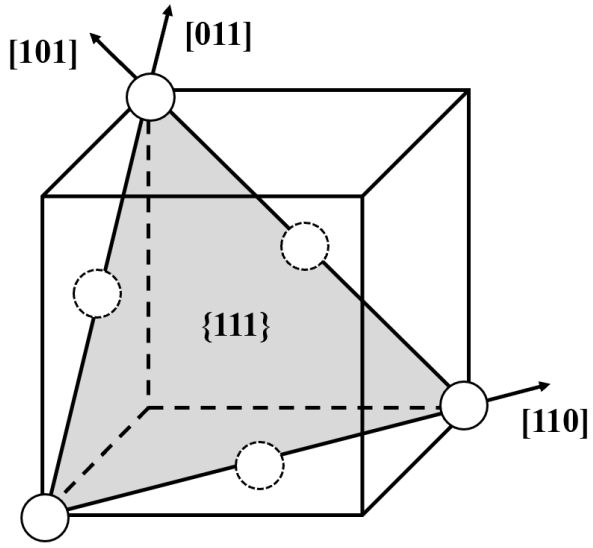

Figure 2.2.2: The {111} slip system in a cubic structure

Under sufficient applied stress to overcome drag coefficients the dislocation glides along the slip plane. Dislocations are initially confined to the slip plane they are generated on, but can move onto a parallel slip plane or transmit onto other slip-systems at energetically favourable angles through different mechanisms. One such mechanism is cross-slip. Forces preventing motion of the dislocation in the slip plane cause cross-slip to another slip system, see Figure 2.2.3, this is an important mechanism in causing slip onto neighbouring slip planes forming slip bands and increased dislocation populations.

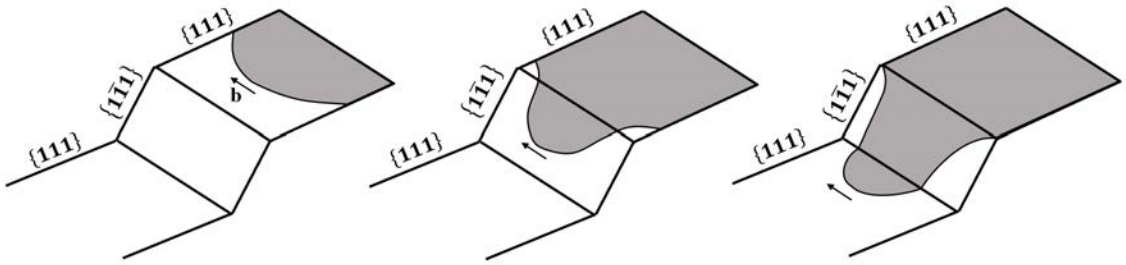

Figure 2.2.3: Cross slip mechanism of a screw dislocation segment.

Another mechanism to move perpendicular to the slip direction when unable to glide, is vacancy diffusion climb. Climb of dislocations is driven by the diffusion of vacancies through

the crystal lattice. Positive climb occurs as a vacancy moves close to the extra half plane, an atom can move up to fill the vacancy that moves in-line with the half plane of atoms shifting the dislocation up, see Figure 2.2.4 (a). Climb is observed more frequently as the temperature increases due to increased vacancy motion, the velocity of climb and relationship to temperature is detailed in Chapter 3.

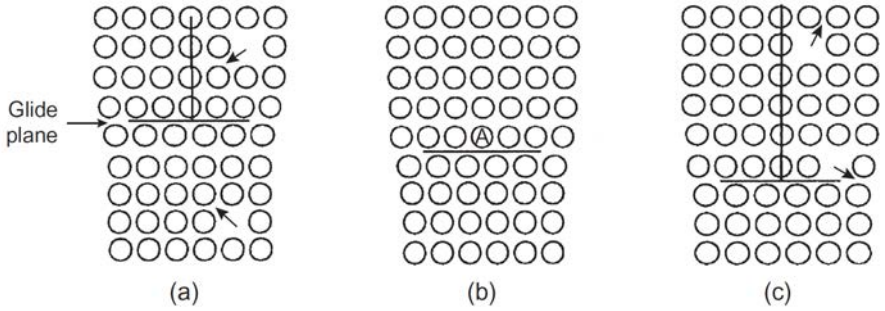

Figure 2.2.4: (a) Positive climb as dislocation shifts up. (b) Dislocation centered on A. (c) Negative climb as dislocation shifts down [15]

.

Initially, hardening occurs as a result of increased dislocation density, through foresting of dislocations and formation of Cottrell-Lomer locks which prevent the motion of mobile dislocations [15–17]. Continued generation of dislocations leads to plastic deformation and softening of the material. The combinations of dislocation types and movement mechanisms configure the dislocations into structures influenced by their stress fields and concentrated plastic stress fields.

2.2.2 Dislocation generation

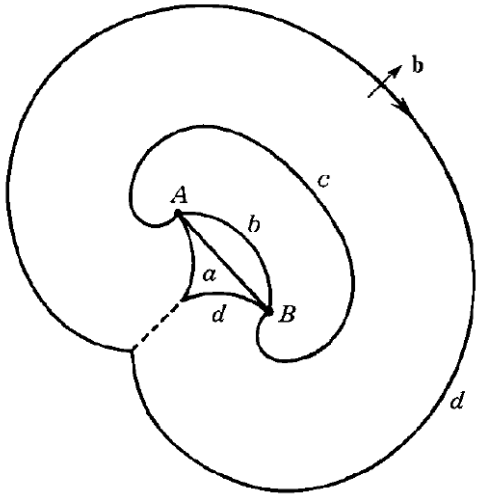

Figure 2.2.5: Stages of the Frank-Read source. Dislocation segment pinned (a) and bowing (b), passing the critical stress and operating as a source(c) and (d) [2]

Dislocations can originate from the microstructure, for example at grain boundaries and phase interfaces, and when striking other dislocations. One of the most common generation mechanisms is the Frank-Read source. This is where a dislocation line is pinned at two points and bows out and around itself upon surpassing a critical applied stress. When the dislocation line bows all the way around the pinning particles sections of the bowing segments annihilate forming a loop and leaving a dislocation line segment between the pinning points which can go onto repeat the mechanism producing more dislocation loops [2, 15]. The mechanism is shown in Figure 2.2.5. When observed as a cross section of the dislocation slip plane this mechanism one positive and one negative edge dislocation forming on a slip plane at a specified distance apart know as the nucleation length, described by

$$L_{nuc} = \frac{\mu}{2\pi(1-\nu)} \frac{b}{\tau_{nuc}} \tag{2.2.1}$$

where τ_{nuc} is the nucleation stress of the source.

2.2.3 Dislocation pile-up theory

Dislocation pile-up is a key physical mechanism in the localisation of deformation. Pile-up of dislocations with obstacles, such as grain boundaries or slip bands, are known to be initiation sites of cracks once a sufficient number of dislocations have congregated. This is well documented mechanism and makes it a strong physical characteristic of dislocation dynamics to use to determine the continuum length scale [2, 18, 19].

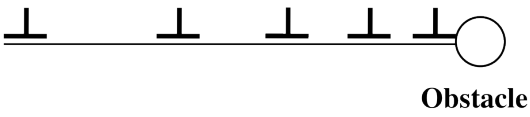

Figure 2.2.6: Diagram of dislocation pile-up

When the dislocations move along the slip planes their path is soon impeded by an obstacle. The lead dislocation is locked by the short range stress field of the boundary. Trailing dislocations of the same sign on the same slip plane are pushed towards the lead dislocation under the applied stress. They then pile-up as they cannot pass the lead dislocation due to the repulsive forces acting between their dislocation stress fields. The equilibrium positions are obtained through the condition that the total force on each free dislocation is zero [2].

$$\frac{Ab}{x_j} + \sum_{i=1, i\neq j}^{n-1} \frac{Ab}{x_j - x_i} - \sigma b = 0, \quad j = 1, 2, ..., (n-1) \tag{2.2.2}$$

For single pile-up the equilibrium positions of dislocations have been calculated by Eshelby [19], a list of these positions are provided by Mura and Cottrell [18], which have been compared to the positions from pile-up in our dislocation dynamics simulations. This confirmed the accuracy of the DDD model. A continuum description of pile-up has been calculated by Leibfried [20]. The dislocation density, $\rho(x)$, in the cases of both unstressed and stressed pile-up of same sign dislocations are given for a specific pile-up length, L are

given by the following equations

$$\rho(x) = \frac{N}{\pi \left[(L/2)^2 - x^2 \right]^{1/2}} \tag{2.2.3}$$

$$\rho(x) = \frac{2\,(1-\nu)\,\sigma}{\mu b} \left[\frac{(L/2) + x}{(L/2) - x} \right]^{1/2} \tag{2.2.4}$$

Along a slip plane there are often dislocations of opposite Burgers vector orientation which will pile-up at opposite ends to one another. This double-ended pile-up is described by

$$\rho(x) = \frac{2\,(1-\nu)\,\sigma}{\mu b} \frac{x}{\left[(L/2)^2 - x^2 \right]^{1/2}} \tag{2.2.5}$$

2.2.4 Shearing γ' particles

Nickel-based superalloys derive their strength from the γ' precipitates and their ordered $L1_2$ crystal structure. In order for the dislocations to transition from the γ matrix to the ordered γ' precipitate it must overcome the associated anti-phase boundary (APB) energy. Dislocations travel in pairs through the precipitate to restore the γ' structure. The lead dislocation creates the anti-phase boundary which is restored by the following dislocation. Whilst dislocation motion is inhibited by the particles, the line segments between particles in the γ matrix bow forward whilst pinned by the γ', see Figure 2.2.7, which influences the mobility of the dislocations. The strength from the precipitates increases with volume fraction. The total amount of plastic deformation of Nickel-based superalloys depends on the precipitate size and volume fraction. Larger precipitates have a larger APB energy. The anti-phase region created between dislocations disrupts the ordering of the aluminium and nickel atoms and increases the energy, this is why it is less favourable for the dislocations to transmit through the ordered precipitate [12]. The shearing of the precipitates, as shown in Figure 2.2.8, gives way to the formation of slip bands and increased shear rates.

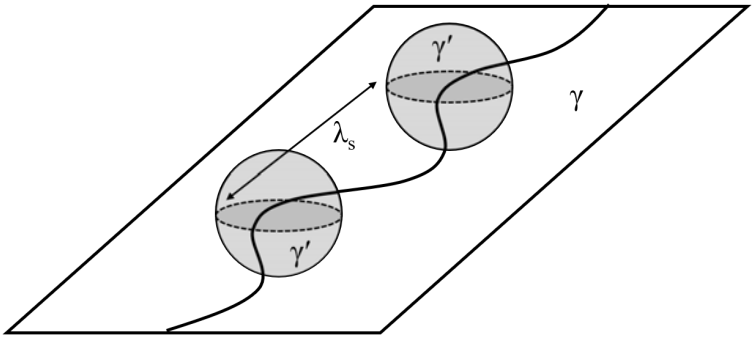

Figure 2.2.7: Sketch showing a dislocation shearing γ' particles and bowing of dislocation segments between the particles

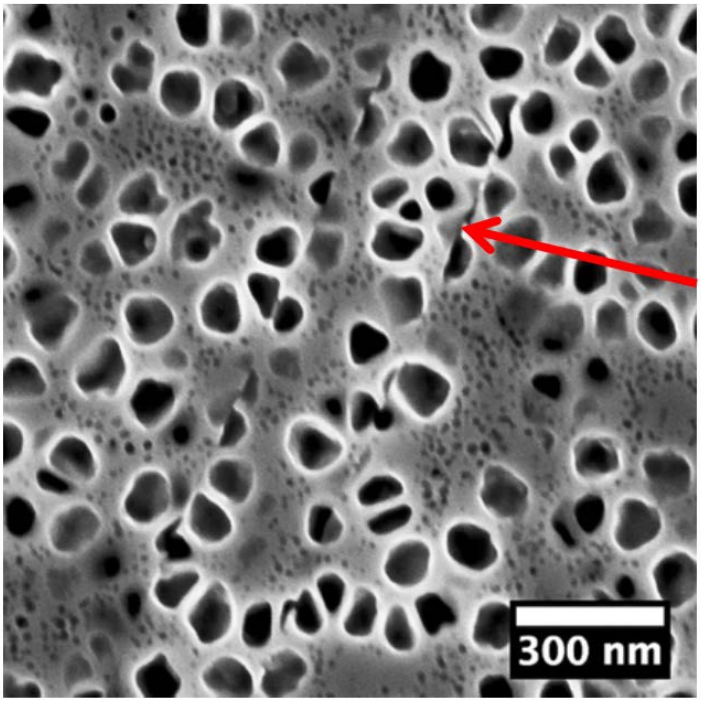

Figure 2.2.8: SEM of shear of fine γ' particles in RR1000 [21]

2.2.5 Dislocation structures

The continued generation of dislocations and the interaction between dislocation stress fields causes them to arrange into dislocation structures. Experimentally these concentrations of dislocations are observed as areas of increased strain in SEM images as seen in Figure 2.2.9.

The strain increase indicates the local displacement of the sample due to the presence of multiple dislocations. When many dislocations are generated on neighbouring parallel slips planes they form slip bands [22]. Slip bands form heterogeneously across the grain, see Figure 2.2.9. Slip bands shear the γ' precipitates, the shearing weakens the precipitate particles lowering the APB energy required to move through the γ' precipitate. This allows further dislocations to shear the precipitate, further weakening it. Slip bands are suspected to promote slip on neighbouring slip planes causing widening of the slip bands.

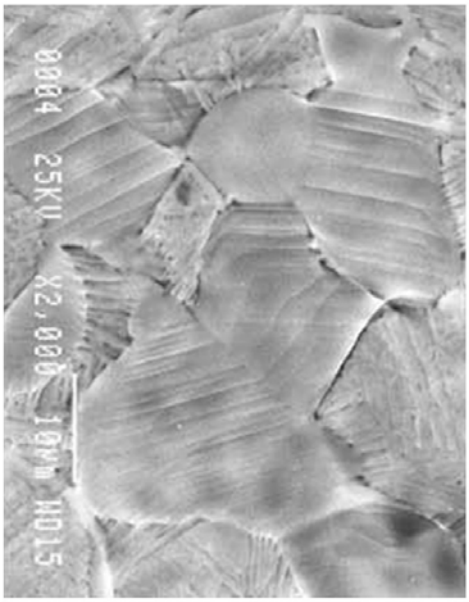

Figure 2.2.9: Slip traces in Titanium alloy [23]

Dislocations can also form more complex arrangements, one is the ladder structure of the persistent slip band (PSB) consisting of regular spaced rungs of high dislocation concentration, see Figure 2.2.10 and Figure 2.2.11.

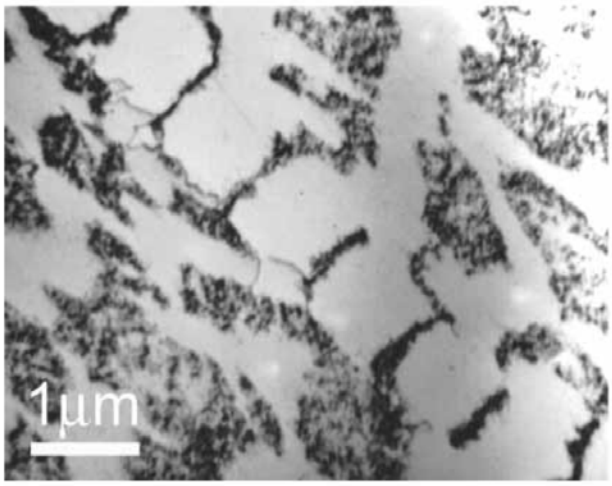

Figure 2.2.10: Image of PSB in Cu [24]

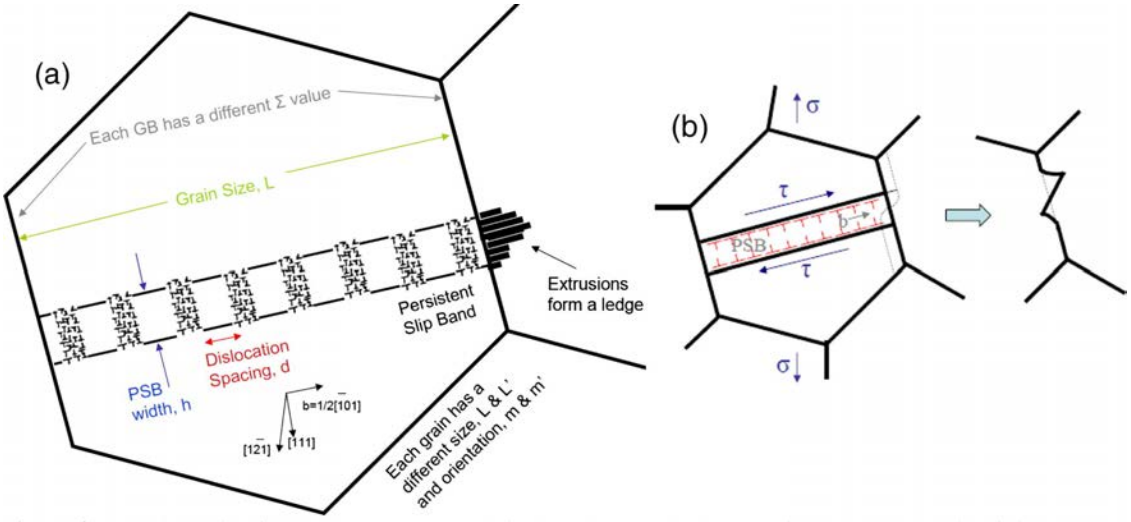

Figure 2.2.11: Schematic of PSB geometry within a polycrystal [25]

Large concentration of dislocations in slip bands and PSBs are stopped at the grain boundary, the displacement caused by the dislocation pile-up forms intrusions and extrusions, see Figure 2.2.12. Stress fields created by these intrusions and extrusions promote slip in the neighbouring grain as well as crack formation. With cyclic loading the size of the extrusions and intrusions increases as more dislocations are generated on the plane with each loading cycle. At low temperature the dislocations are restricted to the same system.

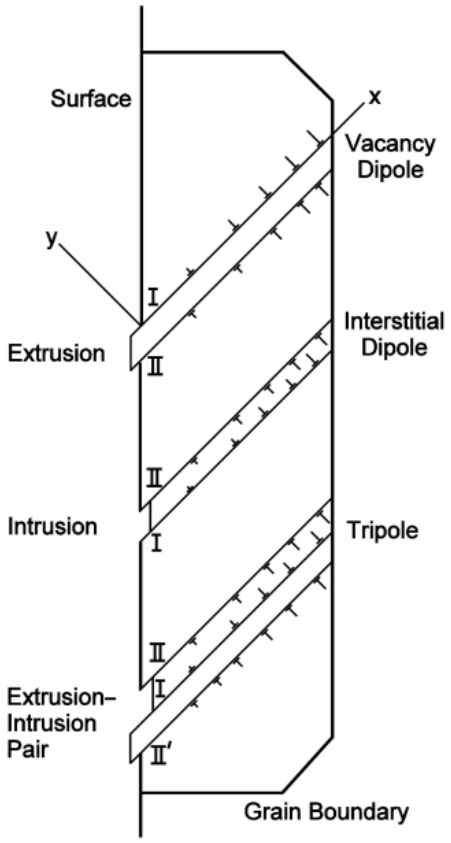

Figure 2.2.12: Schematic of intrusions and extrusions formation [26]. The dislocation pile-ups on layers I and II are under tension and compression, respectively.

The external conditions acting on the component have a very strong effect on the behaviour of the dislocations and their mobility within the alloy. High temperature conditions experienced by the turbine blades make dislocation creep the rate controlling process. Whereas at the cooler temperatures of the disc it is fatigue and the dislocation structures it creates which determine the life of the component. The literature of fatigue of these polycrystalline Nickel-based superalloys is now reviewed to better understand the physics of fatigue and how the alloy micostructure is designed to maximise fatigue life.

2.3 Fatigue of superalloys

As stated previously the life limiting factor of the turbine disc is fatigue life. There are two phases of fatigue life: the number of cycles required to initiate a crack, and the number of cycles to propagate it to failure. Experimentally it is easier to determine the number of cycles to propagate a crack to failure but crack initiation is much harder to identify experimentally. During fatigue, dislocations are generated and begin to glide on preferentially oriented slip planes, when the shear acting on the slip plane reaches a critical value. With each cycle the dislocation density increases. A dislocation continues to glide until it reaches an obstacle which could be a precipitate, grain boundary or another dislocation. Upon further loading dislocations can pass the obstacle by mechanisms like climb, shearing and cross-slip. As the dislocations propagate through these different methods they accumulate as slip irreversibilities, which are early signs of fatigue damage in the material. With further loading the dislocations follow the low energy pathways. As slip continues on these pathways persistant slip bands (PSBs) are formed [23].

Dislocations arrange into low energy configurations and annihilate creating vacancies. These vacancies diffuse within the material edges in ledges, extrusions and intrusions at grain boundaries. These defects create stress concentrations at the boundaries which initiate slip in neighbouring grains. As these effects accumulate, highly concentrated regions of dislocations begin to form. Once enough dislocations are localised into close proximity under sufficient force, the dislocations coalesce to initiate a micro-crack [27, 28]. The fatigue response of the material depends heavily on dislocation mechanics, which in turn are strongly dependent on the applied strain amplitude, stacking fault energy of the material and slip characteristics. Interaction between dislocations and microstructural features, are linked directly to the physics of crack initiation. Thus the material microstructure is optimised for components that experience fatigue.

Discs undergo low cycle fatigue, with the engines experiencing high strain ranges for sustained periods of time. Low cycle fatigue tests are designed to replicate cyclic loading histories relevant to service conditions through stress or strain controlled loading cycles with a dwell time in the loading cycle. The strain range can vary from $\Delta\epsilon = 1\%$ to 2%. During low cycle fatigue the stress amplitude is large enough such that plasticity is induced in each cycle; there is a large plastic strain component [23]. Low cycle fatigue behaviour is commonly described by the Coffin-Manson relationship

$$\frac{\Delta\epsilon_p}{2} = \epsilon'_f(2N_f)^c \tag{2.3.1}$$

where ϵ'_f and c are the fatigue ductility coefficient and exponent respectively, and $2N_f$ is the number of reversals to failure [29]. For low cycle fatigue, LCF, the plastic strain amplitude is larger than the elastic strain range. During LCF fatigue life is short, on the order of 10^4 cycles. Alternatively there is high cycle fatigue, HCF, which has a much smaller stress amplitude operating within the elastic strain range, this takes more cycles to failure (more than 10^4). HCF stems from aero-elastic excitation of the aerodynamic flow field through the blades causing excitation. Figure 2.3.1 shows the relationship between the stress amplitude, $\Delta\sigma$, and number of cycles to failure alongside hysteresis loops for different stress ranges indicated on the curve. The smaller the applied fatigue stress range is the less plastic deformation. Hysteresis loops do not form if the stress range applied stays within the elastic strain limit of the material.

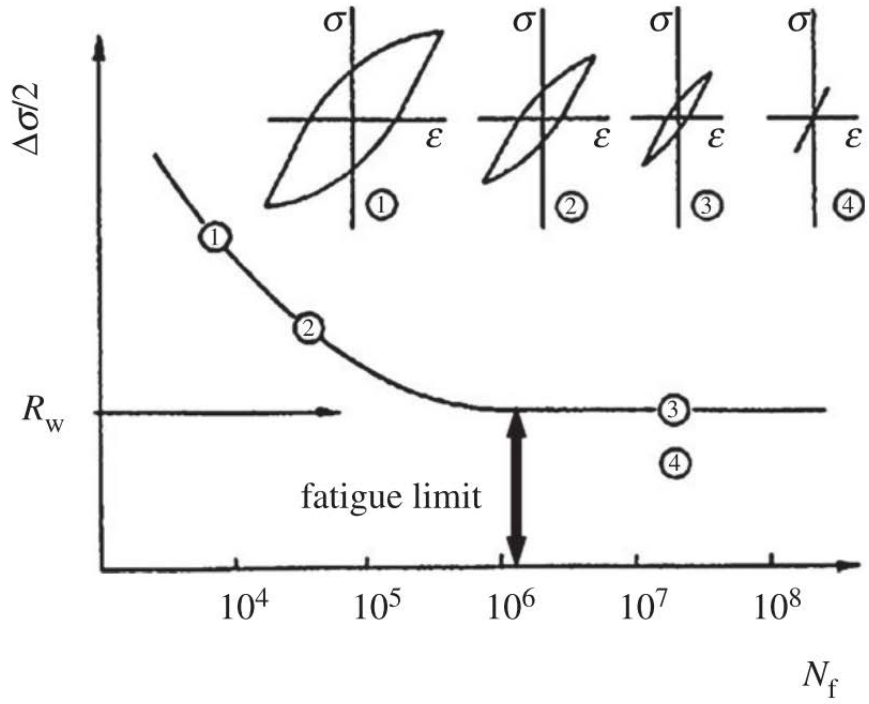

Figure 2.3.1: Schematic of Wöhler curve with hysteresis loops indicated for different stress amplitudes and number of cycles to failure [30]

2.3.1 Hysteresis loops

Under fatigue loading conditions the plastic response of the material due to the dislocation mechanics are reflected in stress-strain plots of hysteresis loops. These show the continuous change of stress and strain during fatigue testing, the shape of the loop changes during the test. With increasing numbers of cycles the stress-strain relation trends toward a steady state hysteresis loop which can be used to characterise the fatigue behaviour of the material. Figure 2.3.2 illustrates the experimentally observed Bauschinger effect which highlights a drop in yield stress due to irreversible plastic microstrain under cyclic loading. After an amount of forward plastic deformation the material yields at a lower stress for reverse loading [5].

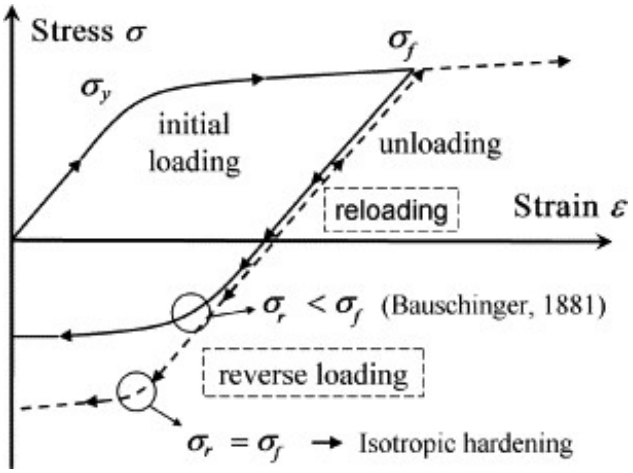

Figure 2.3.2: A schematic of the typical stress-strain curve of the Bauschinger effect [31]

Fatigue loading of a material does not always produce symmetrical loops and there are a few other observed features in the fatigue plots which reflect the accumulation of strain in the system. One feature observed during fatigue loading is shakedown which is the initial build-up in residual stresses that tend towards a steady state elastic-plastic fatigue loop after a number of cycles, Figure 2.3.3. When there is no more net accumulation of plastic strain with each cycle, the system is said to have undergone shakedown upon reaching this point known as the shakedown limit [5]. When the shakedown limit is exceeded then ratchetting is observed, i.e. plastic strains continue to accumulate as the stress is cycled.

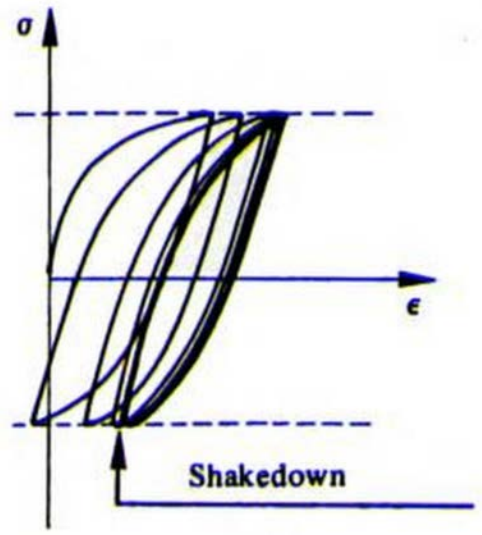

Figure 2.3.3: Diagram of stress controlled elastic shakedown of strain [32]

Ratchetting, also known as cyclic creep, is when the plastic deformation is not matched by an equal amount of yielding with the reverse load, resulting in progressive increase of strain [5]. The plastic strain is accumulated with each cycle, demonstrated in Figure 2.3.4. This is observed more in non-symmetric stress controlled tests.

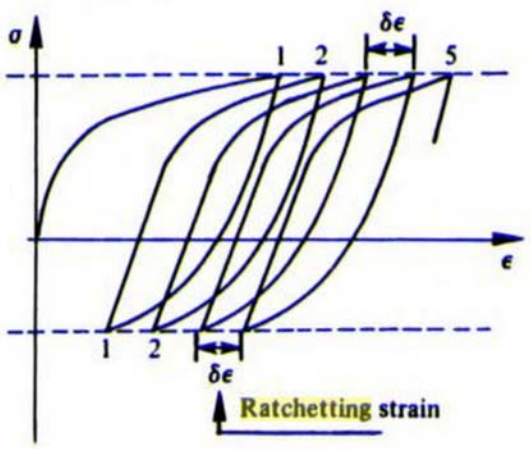

Figure 2.3.4: Diagram of stress controlled strain ratchetting [32]

Understanding the physics reflected by the shape of the fatigue curves assists in analysis of the final results set generated by the FDM model investigating the microstructural influence

on fatigue behaviour.

2.3.2 Crack nucleation sites

Fatigue life is divided into two stages, the first is the number of cycles to fatigue crack initiation, the second is the fatigue crack propagation. The difficulty in the fatigue life to initiation stage is how to define crack initiation. Understanding where the cracks initiate is key to understanding the influence of the microstructure on life span. Researchers have managed to indicate preferable sites for crack initiation.

The role PSBs in fatigue is linked directly to crack initiation, they represent cyclic plastic strain localization where cracks initiate along the fatigue slip bands [24]. They also play a role in initiation at grain boundaries and twin boundaries, and in some cases inhomogeneities. The onset of fatigue damage due to PSBs is indicated by surface roughness created by extrusions, see Figure 2.3.5, this is observed more in single crystals than polycrystals. It is PSB interaction with grain boundaries (GB) which determines crack initiation, the extrusions and intrusions formed at the surface or grain boundaries increase in size with each cycle. The density of dislocation dipoles within the PSB, increase with the number of loading cycles, increasing the elastic strain energy and creating a steep strain gradient between the PSB and the matrix. This elastic strain energy is relieved by crack initiation along the PSB [33]. PSBs can transmit easily from one grain to another at low-angle grain boundaries so that cracking does not occur here, but at large-angle boundaries the strain builds up as the the PSB cannot transmit. Crack initiation due to localization of plastic strain in PSBs is prominent in FCC metals subjected to high-cycle fatigue [30, 34].

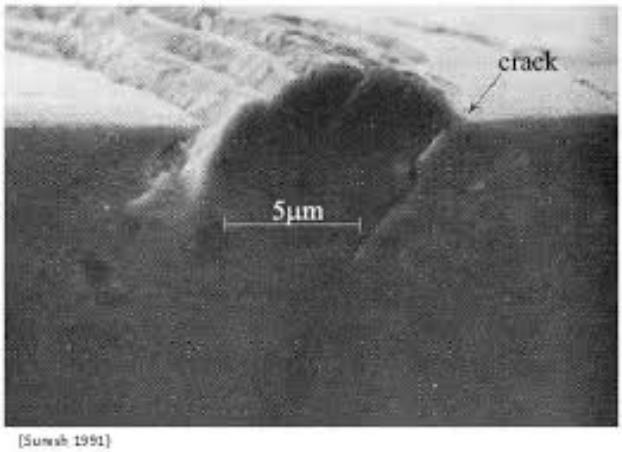

Figure 2.3.5: SEM micrograph of crack initiation along a PSB extrusion at a surface [5]

Grain size and grain boundary characteristics play a role in crack initiation. There are a combination of characteristics which contribute to fatigue crack initiation at grain boundaries. These include grain size, grain boundary structure and the misorientation between neighbouring grains. In polycrystalline metals, the difference in crystallographic orientations is linked to stress localisation and crack nucleation. Grain clusters connected by low-angle grain boundaries allow for slip transmission, their similar orientations mean that they form a 'super grain' and represent a preferred site for crack initiation. Large grains allow more slip of dislocations, these are stopped at the 'super grain' boundary causing a large stress concentration. Typically grain size is kept small in polycrystalline alloys as larger grains allow the formation of persistent slip bands. PSBs can transmit through low-angle grain boundaries, which are described as less than 15° [35]. Cracks are more likely to nucleate at high-angle grain boundaries where slip cannot transfer to the neighbouring grain creating a localisation of stress. Initiation at the grain boundaries is more common in high-strain fatigue due to the larger strain amplitudes applied during cyclic loading [36]. Larrouy et al. [37] studied the interaction of slip bands with grain boundaries for cyclic loading of Udimet 720Li. Identifying a twist angle of more than 55° between grains promotes nucleation of micro-volumes, in particular with slip activated on both sides of the boundary.

Twin boundaries (TBs) are also known to nucleate cracks as they are sites of dislocation pile-up, impinging dislocations similar to grain boundaries. When PSBs form perpendicular the twin boundary, steps or extrusions begin to form. Enhanced stress on slip systems close to the twin boundary promotes secondary glide, this secondary slip facilitates crack formation along the twin boundary [38, 39]. An example of this is shown in Figure 2.3.6. Coherent twin boundaries form from a change in stacking sequence that does not disturb the atomic density, making them a low energy boundary. The orientation of the twin boundary influences the density and growth of twin boundary cracks [40].

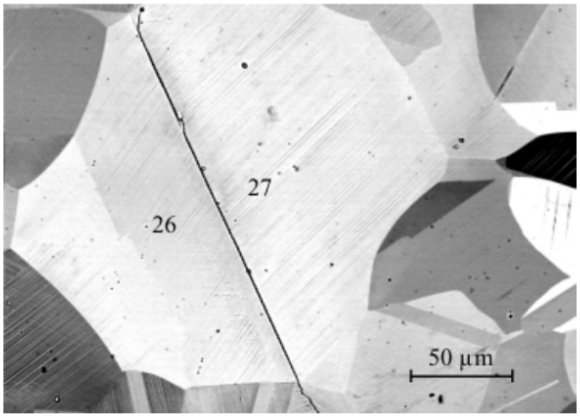

Figure 2.3.6: SEM image of a twin boundary crack [40]

2.3.3 Modelling fatigue crack initiation

Some physical models have been proposed to predict crack initiation at different scales. A dislocation model for crack initiation has been created by Mura [18, 26, 33]. Focusing on the dislocation dipole distribution and the number of cycles it takes for the energy balance of the dipole distribution and surface energy to initiate a crack. Brinkmann and Van der Giessen have used discrete dislocation dynamics to see if fracture stresses were met within the domain [41]. It was not, but they found it very computationally expensive to use this approach. Mughrabi et al. [34, 42] formed a model for intrusions and extrusions from PSBs

as well as initiation of grain boundary cracks by dislocation pile-ups in single crystals based on experimental observations.

Molecular dynamics simulations have been used by Sangid et al. [43, 44] to study slip-GB interaction and dislocation nucleation at the grain boundaries by calculating the energy barriers for slip transmission for different grain boundary misorientations. Sangid also created an expression for the total energy of a PSB and created a failure criterion for the energy of the PSB reaching a minimum value with respect to plastic deformation [23, 25]. The overall energy consisting of the stacking fault energy, anti-phase boundary energy, internal dislocation stress fields, externally applied stress fields, and the energies associated with dislocation nucleation and transmission. This molecular dynamics model produced the correct trends associated with microstructural parameters showing the significant impact of grain boundary character on fatigue life [25]. A traction model was created by Heinz and Neumann [45] to calculate the local stress concentration at twin boundaries promoting crack initiation in LCF. Cracks initiate at both LCF and HCF, but during LCF stresses are high enough to initiate at other sites and thus are observed more frequently.

Finite element crystal plasticity models have been used to analyse the stress and strain distribution across grain distributions under fatigue loading. The effects of grain size distributions and precipitate size distributions on crack initiation have been modelled in a crystal plasticity model specifically for the polycrystalline Nickel-based superalloy turbing disc alloy IN100 [46, 47]. The micromechanics of the dislocations on a slip system were described by a flow rule for the microstructure which determined the mean free path of dislocations.

A polycrystal plasticity model used a simple crack initiation condition for a range of LCF and HCF behaviour in Nickel-based superalloys [48]. The crack initiation condition is determined a critical value for the accumulated effective slip calculated at each point, this

critical value was taken from experimental results. The plasticity model reproduced the Coffin-Manson relationship for LCF failure and both Basquin's rule (stress range to number of cycles relationship) and Goodman's rule (stress range relationship to number of cycles with a mean stress) for HCF crack initiation.

From the literature it is clear that there are a wide range of modelling approaches to fatigue crack initiation. Slip band formation and the interaction with boundaries are essential in understanding fatigue crack nucleation and needs to be considered in potential models.

2.4 Continuum dislocation models

The primary motivation to using a continuum approach to dislocations is that the behaviour of vast numbers of dislocations can be modelled which would not be viable using discrete dislocation mechanics. Modelling this collective behaviour allows for an increase in scale of the simulations hence the larger scale effects of dislocations can be observed. With an increase in computational capability more readily available it is becoming more attractive to use these physically based models to test material properties. The basis of the continuum model is that for a unit area the number of dislocations present within that area is represented via a dislocation density. The dislocation density evolves with time due to dislocation velocity and reaction terms. The theory behind the dislocation density mechanics will influence the dislocation patterns that evolve.

In recent years physically motivated theories of continuum dislocation dynamics have come to the forefront for modelling bulk motion of dislocations to form dislocation structures, as discrete models to do so are far too computationally expensive. The advantages of the continuum approaches are to observe the large scale propagation of the dislocations across grains, formation of dislocation structures, and pile-up of dislocations at grain boundaries

and other obstacles. These different forms of strain localisation can indicate potential sites for crack initiation [22, 23, 25, 35]. The challenge of representing dislocation interactions through a continuum scale is capturing discrete behaviour of dislocations distributed across multiple slip planes. Each point in the continuum model represents a number of dislocations within a unit area that would be distributed over multiple slip planes. The model has to account for these small scale interactions that occur within this unit area that result in the larger dislocation structures formed. Using multi-scale modelling to study the motion of dislocations across different microstructures will help focus the target microstructural parameters when forging future alloys.

Existing continuum based models have been reviewed to inform the present theory of this research, examining what terms are essential to capture the physical behaviour of dislocations on the continuum scale. There are a variety of approaches to continuum theories of dislocations each with their own model assumptions. These assumptions are made to culminate the individual dislocation interactions into reaction terms that describe the collective behaviour of dislocations to increase the scale of modelling and computational efficiency. Starting with the foundation of the dislocation density tensor derived by Nye and Kosevich [49] followed by several different theories for the evolution of a continuum of dislocations. Walgraef and Aifantis [50–52] investigated a reaction diffusion equation description of the dislocation density evolution in the 1970s. Bakó and Groma [53–55] have shown a link between the discrete and continuum models through a stochastic approach to the continuum description. While Hochrainer [56], Acharya [57] and Sandfeld [58] have used models based on a dislocation density tensor and plasticity theory.

2.4.1 Dislocation density tensor

A continuous description of dislocations was first proposed in 1953 by Nye [1] and in 1957 by Kröner [59], this was later built upon from 1965 onwards by Kosevich [17,49]. A brief outline will be provided as it is implemented into the model theory in more detail in Section 3.2. The dislocation density tensor, $\underline{\underline{\boldsymbol{\alpha}}}$, is a representation of dislocations with Burgers vectors and line vectors, it is the number density of lines piercing the plane:

$$\underline{\underline{\boldsymbol{\alpha}}} = \underline{\boldsymbol{\nabla}} \times \underline{\underline{\boldsymbol{\beta}}} \tag{2.4.1}$$

the displacement gradient tensor $\underline{\underline{\boldsymbol{\beta}}}$ is a component of the total distortion. The dislocation density is defined as the net Burgers vector of dislocation lines crossing a unit area. For a single straight dislocation the density can be defined as

$$\underline{\underline{\boldsymbol{\alpha}}} = \underline{\boldsymbol{b}} \cdot \underline{\boldsymbol{t}} \delta(\Gamma) \tag{2.4.2}$$

where $\underline{\boldsymbol{t}}$ represents the line tangent vector of the dislocation and $\delta(\Gamma)$ is the dislocation arc segment [60]. Given that dislocations form as loops and cannot end within the crystal it follows that the Kröner-Nye tensor satisfies the condition

$$div \underline{\underline{\boldsymbol{\alpha}}} = 0 \tag{2.4.3}$$

This is the static description of the the dislocation density tensor. The time evolution of the dislocation density is determined by taking the partial time derivation of Equation (2.4.1) to give

$$\dot{\underline{\underline{\boldsymbol{\alpha}}}} + \underline{\boldsymbol{\nabla}} \times \underline{\boldsymbol{j}} = 0 \tag{2.4.4}$$

with $\underline{\boldsymbol{j}}$ as the dislocation flux through the contour. The right hand side is equal to zero indicating the density is conserved. This is the equation which most continuum descriptions of

dislocations use as the foundation to their model, which they supplement with phenomenological assumptions for dislocations which are not geometrically necessary [61]. Differences between the models arise from the mechanics describing collective dislocation motion. These terms determine how the dislocation density evolves with time.

2.4.2 Reaction diffusion equation

Walgraef and Aifantis [50–52, 62] recognised that the continuity equation can be represented as a reaction diffusion equation, similar to that of a heat diffusion or chemical reaction equation. The total dislocation density is split into populations of mobile (ρ_M) and immobile (ρ_I). Dislocation interactions are treated like reaction rates and their macroscopic motion treated as a diffusion. The diffusion term D_i in front of the second order spatial derivative represents the self interaction of same sign dislocations, this causes large densities of same sign dislocations to 'diffuse' out replicating how they would repel one another. The diffusion term is of the form $D \sim \langle v \rangle \langle l \rangle$ where $\langle v \rangle$ is an average dislocation velocity and $\langle l \rangle$ a characteristic length [63]. The reaction rates for the immobile dislocation density, ρ_I, and mobile dislocation densities, ρ_M, are as follows

$$\partial_t \rho_I = g(\rho_I) + D_I \nabla^2_{xx} \rho_I - b\rho_I + \rho_M \rho_I^2 \tag{2.4.5}$$

$$\partial_t \rho_M = D_M \nabla^2_{xx} \rho_M + b\rho_I - \rho_M \rho_I^2 \tag{2.4.6}$$

where the term $-b\rho_I$ is the rate at which immobile dislocations are breaking free producing mobile dislocations, the b coefficient acts in a Heaviside-like fashion depending on the external stress. The term $\rho_M \rho_I^2$ is the rate at which mobile dislocations are immobilized by dipoles of immobile dislocations. In Equation (2.4.5) the $g(\rho_I)$ function represents a source term for the immobile dislocations. This framework was created to model a ladder like pattern formation of a PSB and vein formation. The competition between the stress induced mobilization of

dislocations and their immobilisation by dipoles, governed by wave vectors (fully described by Walgraef and Aifantis [50–52]) results in formation of spatial patterns. The wave vectors, which make the dislocations form the ladder structure, correspond to the intrinsic wavelength of patterns from experimental observations. For example, the width of veins (dislocation rich) and channels (dislocation poor) was measured at $1.2\,\mu$m, and the wavelength of the PSB patterns was found to centre on $1.4\,\mu$m for the regularly spaced walls of high density [62]. The model is designed to create patterns with increasing stress, the behaviour is described in discrete stages:

1. At low stress the mobilities are very small, there is a stable homogeneous dislocation density of purely sessile dislocations.

2. As the stress increases, but is still below the threshold stress, mobility increases but the rate of annihilation events is negligible. The wave vector can become positive leading to an instability of homogeneous density, the maximum of dislocations are distributed on rodlike patterns.

3. The stress is equal to the threshold stress, inhomogeneous wave functions favour wave functions in the x-direction due to dislocations becoming mobile. Periodic ladder structures form alongside rod-like vein structures.

4. Under further stress it reaches a new threshold where the rodlike structures become unstable verses the ladderlike. These ladderlike patterns fill the domain.

The focus of the model is tailored specifically to the wavelengths of the dislocation pattern formation of veins and PSBs, neglecting other potential forms of dislocation localisation. The model describes one dislocation density of both positive and negative dislocations. One major assumption of this model is that there is no term to describe the long range interaction of dislocations, in particular attraction between those of opposite Burgers vector. This neglects

the promotion of slip elsewhere in the simulated grain by the dislocation stress fields from sites of stress localisation.

2.4.3 Stochastic continuum dislocation dynamics

Using statistical physics is an obvious approach to describe large numbers of dislocations as it links the microscopic and macroscopic behaviour, greatly reducing the large number of calculations that would be required. A statistical mechanics type approach uses probability distribution functions of stress values to select stress values randomly from a specific range, increasing computational efficiency [64].

Dislocation patterning is caused by the intrinsic fluctuations acting on an ensemble of dislocations and is observed on a mesoscopic scale. Hähner [65–67] proposed a stochastic approach that utilises strain rate fluctuations of collective dislocation glide to induce the cell patterning process. This approach considered plastic deformation of a crystal on a mesoscopic scale as an effective medium exhibiting spatio-temporal fluctuations of stress and strain rate.

The stochastic concept of dislocations was really focused on by Groma et al. [53–55, 68–70]. It utilised probability distribution functions that described the short range correlation functions to form dislocation patterning. These stochastic approaches have been applied to both discrete and continuum dislocation descriptions. This concept was thought of after observing the stochastic nature of the stress field created by dislocations irregular fluctuation of stress around an average. Mathematically, the work is based on the Markovian method for the random flights of particles. It is applied to the probability distribution of the internal stress of a dislocation density function $w_N(\underline{\boldsymbol{r}}_1, \underline{\boldsymbol{r}}_2, ...\underline{\boldsymbol{r}}_N)$. This stochastic model closely followed the Markovian model described by Chandrasekhar [71]. The stochastic aspect to the model is

the probability distribution function of the localised stress,

$$P(\tau_0)d\tau_0 = \int ... \int w_N(\underline{\boldsymbol{r}}_1, \underline{\boldsymbol{r}}_2, ...\underline{\boldsymbol{r}}_N)d\underline{\boldsymbol{r}}_1, d\underline{\boldsymbol{r}}_2, ...d\underline{\boldsymbol{r}}_N \tag{2.4.7}$$

where the dislocations positions are given by $\underline{\boldsymbol{r_i}} = (x_i, y_i)$, and $P(\tau_0)d\tau_0$ is the probability of τ occurring in a range, used to select a stress fluctuation value for a density. As stress fields do not need to be calculated from every other point to total the inter-dislocation stresses using instead the stochastic nature to assign a stress improving efficiency of the simulations. From short discrete dislocation dynamics simulations the internal stress can be decomposed into two independent components, mean field force from the dislocation distribution and a stochastic stress fluctuation component

$$\tau_0 - \frac{d\tau_0}{2} \leq \tau^{fluc}(\underline{\boldsymbol{r}}) \leq \tau_0 + \frac{d\tau_0}{2} \tag{2.4.8}$$

where τ_0 is a preassigned value for τ, or mean internal stress. The stress per point is selected depending on the probability generated and used in the simulation. Taking into account the stochastic character of the internal stress into the stress term, the dislocations obey the following Langevin equation for the velocity [54]

$$\underline{\boldsymbol{v}}(\underline{\boldsymbol{r}}) = M\underline{\boldsymbol{b}}\left[\tau^{int}(\underline{\boldsymbol{r}}) + \tau^{ext} + \tau^{fluc}(\underline{\boldsymbol{r}})\right]^{\frac{1}{m}} \tag{2.4.9}$$

where M is the dislocation mobility and m is the velocity-stress exponent. The first moment of $P(\tau_0)$ is an important characteristic value described by

$$\langle\tau(\underline{\boldsymbol{r}})\rangle = \int \rho(\underline{\boldsymbol{r}})b\tau^{int}(\underline{\boldsymbol{r}} - \underline{\boldsymbol{r}}_1)d\underline{\boldsymbol{r}}_1 \tag{2.4.10}$$

this is the probability distribution, $\langle\tau(\vec{r})\rangle$, of values the stress can take [68]. Groma and Bakó then took the second moment of the probability distribution function. Due to the $1/r$ nature

of the straight dislocation stress field it results in a singularity in the integrand making the second moment infinite. Using the Langevin equation (2.4.9) the equation for the evolution of the dislocation density allowing dislocation creation and annihilation is given by

$$\frac{\partial \rho(\underline{\boldsymbol{r}},t)}{\partial t} + (\underline{\boldsymbol{b}}\Delta)\{Mk(\underline{\boldsymbol{r}},t)\left[\tau^{int}(\underline{\boldsymbol{r}},t) + \tau^{fluc}(\underline{\boldsymbol{r}},t) + \tau^{ext}\right]^{1/m}\} = f(\rho,\bar{\tau},\tau^{ext},...) \qquad (2.4.11)$$

where f on the right hand side is source term dependent on variables like the dislocation density and stress components, and $k(\underline{\boldsymbol{r}},t) = \rho^{+}(\underline{\boldsymbol{r}},t) - \rho^{-}(\underline{\boldsymbol{r}},t)$ is the sign density [54]. The statistical-mechanics description detailed by Groma has extended the theory to multiple slip systems using correlation functions and phenomenological approaches [72, 73]. Yefimov also introduced interaction events for dislocation generation and annihilation [74]. For this theory the response of plastic deformation shows similar behaviour to those from discrete dislocation results.

2.4.4 Crystal plasticity from continuum dislocations

Some approaches tie the continuum dislocations dynamics directly into the crystal plasticity calculations, giving the material response to the dislocation density evolution. This is the type of approach utilised in the present theory of field dislocation mechanics. Existing theories based on the Nye-Kröner dislocation density tensor resolve the slip deformation to get the elasto-plastic response of the deformation. Acharya and Roy [57, 75] proposed a theory of crystal plasticity based on dislocation density as the primary internal variable described by a partial differential equation. Their theory used the sum of the possible dislocation fluxes of dislocation line directions and velocities, along with the applied loads to determine the current state of stress in the body by updating the displacement gradient. The link between the dislocation density tensor and the elasto-plastic calculations are well described by Acharya [57, 76] and result in the additive decomposition of the elastic and

plastic parts for the velocity gradient tensor,

$$\underline{\underline{\boldsymbol{L}}} = \underline{\underline{\dot{\boldsymbol{F}}}}^{e}\,\underline{\underline{\dot{\boldsymbol{F}}}}^{e-1} + (\underline{\underline{\boldsymbol{F}}}^{e}\underline{\underline{\boldsymbol{\alpha}}}) \times \underline{\underline{\boldsymbol{V}}} \tag{2.4.12}$$

where $\underline{\underline{\dot{\boldsymbol{F}}}}^{e}\,\underline{\underline{\dot{\boldsymbol{F}}}}^{e-1}$ is the elastic part and $(\underline{\underline{\boldsymbol{F}}}^{e}\underline{\underline{\boldsymbol{\alpha}}}) \times \underline{\underline{\boldsymbol{V}}}$ is the plastic part. The plastic part is defined by the rate of deformation produced by the flow of dislocation lines, $\underline{\underline{\boldsymbol{V}}}$ is the dislocation velocity field transporting the dislocation line density field [76]. A least squares finite element discretization method was used to integrate dislocation density dependent displacement field calculations into finite element software ABAQUS [77]. These descriptions of $\underline{\underline{\boldsymbol{\alpha}}}$ are taken to be equivalent to the geometrically necessary dislocation densities, ρ_{GND}, these are dislocations with the same line direction. The geometrically necessary dislocation density is propagated by a combination of the internal and external stress, to provide a plastic response. To account for the influence of dislocation curvature on motion, the dislocation density tensor is given in circular coordinates;

$$\underline{\underline{\boldsymbol{\alpha}}}(r,\phi) = \int_{0}^{2\pi} \rho(r,\phi)\underline{\boldsymbol{l}}(\phi)d\phi \otimes \underline{\boldsymbol{b}} \tag{2.4.13}$$

where the curvature density, $\underline{\boldsymbol{l}}(\phi)$, accounts for line tension effects which are reflected in the shear stress. The model presented by Hochrainer et al. [78] is a description of dislocation density for one slip system, where the kinematics are described as a function of the net shear stress

$$\underline{\boldsymbol{v}} = \frac{\boldsymbol{b}}{B}\{\underline{\boldsymbol{\tau}}^{0} + \underline{\boldsymbol{\tau}}^{1} + \underline{\boldsymbol{\tau}}^{b} + \underline{\boldsymbol{\tau}}^{y}\} \tag{2.4.14}$$

where B is the drag coefficient. The net shear stress is the sum of multiple terms including a reference shear stress, $\underline{\boldsymbol{\tau}}^{0}$, shear stress related to the shear, $\underline{\boldsymbol{\tau}}^{1}$, a yield stress, $\underline{\boldsymbol{\tau}}^{y}$, and the back stress, $\underline{\boldsymbol{\tau}}^{b}$, which is a function of curvature. Partial derivative of the total dislocation density,

$$\partial_t \rho = (div(\rho \boldsymbol{v}) + \partial_\phi(\rho\vartheta)) + \rho \boldsymbol{v} k \tag{2.4.15}$$

with ϑ as the rotation velocity of the segments and k as mean curvature of dislocations, the partial differential of which is

$$\partial_t k = -vk^2 + \nabla_L(\vartheta) - \nabla_V(k) \tag{2.4.16}$$

where $\nabla_L(\vartheta)$ is the derivative of the rotation velocity along the line direction and $\nabla_V(k)$ is the derivative of curvature along the generalised velocity direction. Equation (2.4.15) and Equation (2.4.16) are coupled from systematic averaging of configurations [56, 58, 78]. A statistical description of the dislocation interactions in terms of a Taylor-type yield stress and a back stress use geometry dependent parameters to describe the short-range repulsion of dislocations, recreating behaviour observed in DDD simulations [58]. These methods go on to work out the shear from the dislocation density, and from that the plastic distortion rate which is used to calculate the plastic displacement locally created by the dislocations [56,58,61,78]. These models link to crystal plasticity calculations by the generalised Orowan equation;

$$\partial_t \underline{\underline{\boldsymbol{\beta}}}^p = \dot{\gamma} \underline{\boldsymbol{n}} \cdot \underline{\boldsymbol{b}} \tag{2.4.17}$$

this relates the plastic distortion rate, $\partial_t \underline{\underline{\boldsymbol{\beta}}}^p$, to the density by the shear rate, $\dot{\gamma}$, created by its velocity on the slip system. Although designed for three dimensional flexible lines these models have been simplified to two dimensions.

Shulz et al. [79] uses the simplified two dimensional CDD model proposed by Hochrainer et al. [56] and Sandfeld et al. [58] and tests the pile-up behaviour against that of discrete simulations and literature descriptions for continuous distributions of dislocations referred to as geometrically necessary dislocations, ρ_{GND}. The model is driven by the stress composed of the external stress, the internal stress contributions and a corrective stress to account for stress contributions from the dislocations contained within the unit area of density. The corrective stress allows them to use a larger mesh whilst maintaining accuracy [79]. These

simulations tested the mechanics of the dislocations and showed accurate reproduction of pile-up effects for a closed system where the total density is conserved. The conservation of the dislocation density is one place where this crystal plasticity modelling by continuum dislocations is still in its infancy. Terms for generation and annihilation often included in formulation but are not utilised.

Chapter 3

Theoretical framework - Field dislocation mechanics

The following section describes a field dislocation mechanics (FDM) formulation proposed by Basoalto and Little [80] which is a type if continuum dislocation dynamics approach. This physically based theory is a bottom up approach and builds on the transport of the Kröner-Nye dislocation density tensor [1, 17] and leads to a continuity equation for a scalar dislocation density field, $\rho(\underline{\boldsymbol{x}}, t)$. The mobility of the density field is determined by the total force acting on the dislocation field and dislocation line mobility considerations. The velocity field is dictated by internal stress fields of the dislocation density, physical dislocation behaviour and interaction with the crystal microstructure, and external loading conditions on the system. From the advection of dislocation fields the elastic and plastic displacement distortions are calculated to update the micro stress state of the domain.

3.1 Boundary value problem

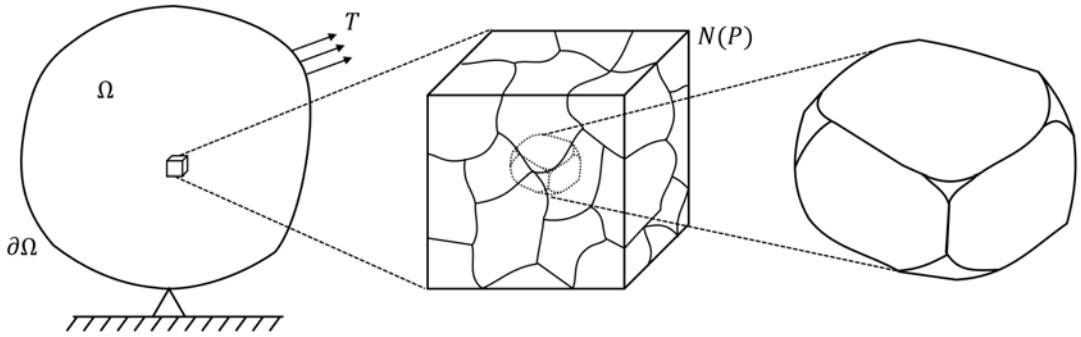

Figure 3.1.1: Schematic illustrating length scales from macroscale deformation (left) to a local neighbourhood of grains (centre) to the representative volume element (right)

This section sets up conditions of the domain in which the field dislocation mechanics is applied. Let the material domain at the macroscale be defined by a set of points $\Omega\{\boldsymbol{X} \in \mathbb{R}\}$ with a boundary $\partial\Omega$ as demonstrated in Figure 3.1.1. Suppose a traction $\underline{\boldsymbol{T}}$ acting on the boundary $\partial\Omega$ which gives rise to a stress field within the material domain $\underline{\underline{\boldsymbol{\Sigma}}}$. The stress satisfies the local equilibrium conditions

$$\underline{\boldsymbol{\nabla}} \cdot \underline{\underline{\boldsymbol{\Sigma}}} = 0 \tag{3.1.1}$$

$$\underline{\boldsymbol{T}} = \underline{\boldsymbol{\nu}} \cdot \underline{\underline{\boldsymbol{\Sigma}}} \tag{3.1.2}$$

where $\underline{\boldsymbol{\nu}}$ is the vector normal to the boundary. This loading is treated as a quasi-static problem in the finite element simulations where the load rate is slow enough that there is no acceleration effects like inertia. Defining a neighbourhood about a point P in the material, see Figure 3.1.1. Let us suppose the material neighbourhood has a structure composed of crystallographic grains and defines a representative volume element (RVE). The macroscale properties can be derived through appropriate homogenisation of the microscale fields distributed within the RVE [80].

3.2 Continuum theory of dislocations

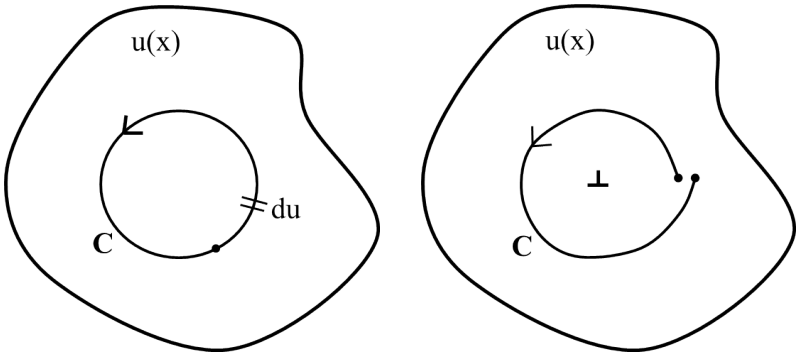

(a) Closed loop (b) Open loop

Figure 3.2.1: Path integral over a contour, C: (a) taken around a perfect crystal, (b) around a dislocation

The dislocation density tensor will now formally be introduced. The presence of a dislocation loop will result in a displacement field which is singular at the dislocation line. A characteristic of this displacement field is that evaluation of a path integral over the dislocation displacement field, $d\boldsymbol{u}^d(\boldsymbol{x})$, along any arbitrary contour C results in a non-closure condition given by

$$\underline{\boldsymbol{B}} = \oint_C d\underline{\boldsymbol{u}}^d \tag{3.2.1}$$

where $\underline{\boldsymbol{B}}$ is the Burgers vector. This is illustrated in Figure 3.2.1. If there are multiple dislocations enclosed in C the non-closure condition will measure the sum of the burgers vectors. By definition the gradient of the elastic displacement field arising for the dislocation loop is given by

$$\underline{\underline{\boldsymbol{\beta}}}^d(\boldsymbol{x}, t) = \underline{\boldsymbol{\nabla}}\, \underline{\boldsymbol{u}}^d(\underline{\boldsymbol{x}}, t) \tag{3.2.2}$$

Inserting the last expression into Equation (3.2.1) and using Stokes' theorem the contour integral defining the Burgers vector becomes

$$\begin{aligned}\underline{\boldsymbol{B}} &= \oint_C \underline{\boldsymbol{\nabla}}\, \underline{\boldsymbol{u}}^d(\underline{\boldsymbol{x}}, t) d\underline{\boldsymbol{x}} \\ &= \oint_C \underline{\underline{\boldsymbol{\beta}}}^d(\underline{\boldsymbol{x}}, t) d\underline{\boldsymbol{x}} \\ &= \iint_S \underline{\boldsymbol{\nabla}} \times \underline{\underline{\boldsymbol{\beta}}}^d(\underline{\boldsymbol{x}}, t) d\underline{\boldsymbol{S}} \\ &= \iint_S \underline{\underline{\boldsymbol{\alpha}}}(\underline{\boldsymbol{x}}, t) d\underline{\boldsymbol{S}}\end{aligned} \tag{3.2.3}$$

Equation (3.2.3) defines the Nye dislocation density tensor as the curl of the plastic distortion

$$\underline{\underline{\boldsymbol{\alpha}}}(\underline{\boldsymbol{x}}, t) = \underline{\boldsymbol{\nabla}} \times \underline{\underline{\boldsymbol{\beta}}}^d(\underline{\boldsymbol{x}}, t) \tag{3.2.4}$$

3.2.1 Transport equation for the dislocation field

This section focuses on deriving the governing equation for the transport of the dislocation field. The approach has derived local conditions for the advection of the dislocation field from the rate of change of the Burgers vector as defined by Equation (3.2.3). The rate of change of $\boldsymbol{B}$ is balanced by the flux of dislocations crossing the contour C and by any dislocation reactions taking place in C, see Figure 3.2.2.

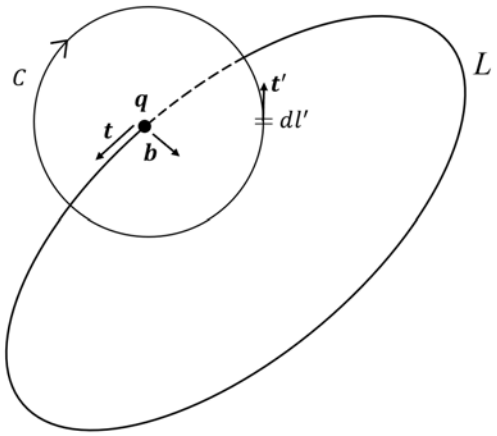

Figure 3.2.2: Dislocation configuration

The number of lines crossing line element on C, dl, corresponds to the flux of total Burgers vector,

$$d\dot{\underline{\boldsymbol{B}}}(\boldsymbol{x},t) = \underline{\boldsymbol{b}}\rho(\underline{\boldsymbol{x}},t)\dot{\underline{\boldsymbol{q}}} \cdot (\underline{\boldsymbol{n}} \times \underline{\boldsymbol{t}})dl \tag{3.2.5}$$

when $\boldsymbol{n}$ is normal to dl on C and $\underline{\boldsymbol{q}}$ is a point on the dislocation, thus $\dot{\underline{\boldsymbol{q}}}$ is the velocity of the dislocation at that point, as shown in Figure 3.2.2.

$$\underline{\underline{\boldsymbol{\alpha}}}(\underline{\boldsymbol{x}},t) = \underline{\boldsymbol{b}}\rho(\underline{\boldsymbol{x}},t)\underline{\boldsymbol{t}} \tag{3.2.6}$$

Using the vector triplet product identity and the substitution of Equation (3.2.6) the flux of the Burgers vector can be described in terms of the plastic velocity gradient tensor

$$\begin{aligned} d\dot{\underline{\boldsymbol{B}}}(\underline{\boldsymbol{x}},t) &= \underline{\boldsymbol{b}}\rho(\underline{\boldsymbol{x}},t)\underline{\boldsymbol{t}} \cdot (\dot{\underline{\boldsymbol{q}}} \times \boldsymbol{n})dl \\ &= \underline{\underline{\boldsymbol{\alpha}}}(\underline{\boldsymbol{x}},t) \cdot (\dot{\underline{\boldsymbol{q}}} \times \underline{\boldsymbol{n}})dl \\ &= \underline{\underline{\boldsymbol{L}}}^p \cdot \underline{\boldsymbol{n}}dl \end{aligned} \tag{3.2.7}$$

using the relationship, $\underline{\underline{\boldsymbol{L}}}^p = \underline{\underline{\boldsymbol{\alpha}}}(\underline{\boldsymbol{x}},t) \times \dot{\underline{\boldsymbol{q}}}$. The total flux of Burgers vector for the number of dislocations crossing the circuit C is obtained by integrating Equation (3.2.7) and applying

Stokes' theorem

$$\begin{aligned}\dot{\underline{\boldsymbol{B}}}(\underline{\boldsymbol{x}},t) &= \oint_C \underline{\underline{\boldsymbol{L}}}^p \cdot d\underline{\boldsymbol{l}} \\ &= \iint_S \underline{\boldsymbol{\nabla}} \times \underline{\underline{\boldsymbol{L}}}^p \, d\underline{\boldsymbol{S}}\end{aligned} \tag{3.2.8}$$

To account for dislocation reactions generation and annihilation rates $\dot{A}^+(\underline{\boldsymbol{x}},t)$ and $\dot{A}^-(\underline{\boldsymbol{x}},t)$ are introduced respectively [80]. From these considerations the rate of change in the Burgers vector can be written as

$$\frac{d}{dt}\left(\iint_S \underline{\underline{\boldsymbol{\alpha}}}(\boldsymbol{x},t)d\underline{\boldsymbol{S}}\right) = \iint_S \underline{\boldsymbol{\nabla}} \times \underline{\underline{\boldsymbol{L}}}^p \, d\underline{\boldsymbol{S}} + \iint_S \left[\dot{A}^+(\underline{\boldsymbol{x}},t) - \dot{A}^-(\underline{\boldsymbol{x}},t)\right] d\underline{\boldsymbol{S}} \tag{3.2.9}$$

The time derivative of the integral in the left hand side of Equation (3.2.9) becomes

$$\frac{d}{dt}\iint_S \underline{\underline{\boldsymbol{\alpha}}}(\underline{\boldsymbol{x}},t)d\underline{\boldsymbol{S}} = \iint_S \left[\dot{\underline{\underline{\boldsymbol{\alpha}}}}(\underline{\boldsymbol{x}},t)d\underline{\boldsymbol{S}} + \underline{\underline{\boldsymbol{\alpha}}}(\underline{\boldsymbol{x}},t)\frac{d}{dt}(d\underline{\boldsymbol{S}})\right] \tag{3.2.10}$$

Using Nanson's formula for surface change from the initial to the immediate configuration is $d\underline{\boldsymbol{S}} = |\underline{\underline{\boldsymbol{F}}}^p|(\underline{\underline{\boldsymbol{F}}}^p)^{-T}dS_0$, and substituting $\underline{\underline{\boldsymbol{L}}}^p = \dot{\underline{\underline{\boldsymbol{F}}}}\underline{\underline{\boldsymbol{F}}}^p$ the time derivative of the element is $d\dot{\underline{\boldsymbol{S}}} = -(\underline{\underline{\boldsymbol{L}}}^p)^T dS_0$. It follows that Equation (3.2.10) can be expressed as

$$\frac{d}{dt}\iint_S \underline{\underline{\boldsymbol{\alpha}}}(\underline{\boldsymbol{x}},t)d\underline{\boldsymbol{S}} = \iint_S \left[\dot{\underline{\underline{\boldsymbol{\alpha}}}}(\underline{\boldsymbol{x}},t)d\underline{\boldsymbol{S}} - \underline{\underline{\boldsymbol{\alpha}}}(\underline{\boldsymbol{x}},t)(\underline{\underline{\boldsymbol{L}}}^p)^T d\underline{\boldsymbol{S}}\right] \tag{3.2.11}$$

Moving all the terms in Equation (3.2.9) to one side and using the expansion given by Equation (3.2.11) gives the continuity equation

$$\iint_S \left[\dot{\underline{\underline{\boldsymbol{\alpha}}}}(\underline{\boldsymbol{x}},t) - \underline{\underline{\boldsymbol{\alpha}}}(\underline{\boldsymbol{x}},t)(\underline{\underline{\boldsymbol{L}}}^p)^T - \underline{\boldsymbol{\nabla}} \times \underline{\underline{\boldsymbol{L}}}^p - \dot{A}^+(\underline{\boldsymbol{x}},t) + \dot{A}^-(\underline{\boldsymbol{x}},t)\right] d\underline{\boldsymbol{S}} = 0 \tag{3.2.12}$$

As all the terms are integrated over the surface, S, it follows that the integrand is also equal

to zero which presents the final evolution equation

$$\dot{\underline{\underline{\boldsymbol{\alpha}}}}(\underline{\boldsymbol{x}},t) - \underline{\underline{\boldsymbol{\alpha}}}(\underline{\boldsymbol{x}},t)\cdot(\underline{\underline{\boldsymbol{L}}}^p)^T - \underline{\boldsymbol{\nabla}}\times\underline{\underline{\boldsymbol{L}}}^p = \dot{A}^+(\underline{\boldsymbol{x}},t) - \dot{A}^-(\underline{\boldsymbol{x}},t) \tag{3.2.13}$$

The material derivative of the dislocation density, $\dot{\underline{\underline{\boldsymbol{\alpha}}}}$, can be split into temporal and spatial components

$$\dot{\underline{\underline{\boldsymbol{\alpha}}}}(\underline{\boldsymbol{x}},t) = \frac{\partial\underline{\underline{\boldsymbol{\alpha}}}(\underline{\boldsymbol{x}},t)}{\partial t} + \underline{\boldsymbol{v}}^k(\underline{\boldsymbol{\nabla}}\cdot\underline{\underline{\boldsymbol{\alpha}}}(\underline{\boldsymbol{x}},t)) \tag{3.2.14}$$

where $\underline{\boldsymbol{v}}^k$ is the material velocity. This expansion is put in Equation (3.2.13) The dislocation density tensor is related to the scalar density by Equation (3.2.6) this was substituted into Equation (3.2.13) to give the two dimensional formulation of the equation. Using the scalar density $\rho(\underline{\boldsymbol{x}},t)$ the vector product of $\underline{\underline{\boldsymbol{\alpha}}}(\underline{\boldsymbol{x}},t)\cdot(\underline{\underline{\boldsymbol{L}}}^p)^T$ goes to zero, and using vector calculus the term $\underline{\boldsymbol{\nabla}}\times\underline{\underline{\boldsymbol{L}}}^p$ simplifies to $\underline{\boldsymbol{\nabla}}\cdot(-\rho(\underline{\boldsymbol{x}},t)\underline{\boldsymbol{v}}(\underline{\boldsymbol{x}},t))$ giving the scalar density form of the continuity equation

$$\frac{\partial\rho(\underline{\boldsymbol{x}},t)}{\partial t}+\underline{\boldsymbol{v}}^k(\underline{\boldsymbol{\nabla}}\cdot\rho(\underline{\boldsymbol{x}},t))+\rho(\underline{\boldsymbol{x}},t)(\underline{\boldsymbol{\nabla}}\cdot\underline{\boldsymbol{v}}^k)-\underline{\boldsymbol{\nabla}}\cdot(-\rho(\underline{\boldsymbol{x}},t)\underline{\boldsymbol{v}}(\underline{\boldsymbol{x}},t)) = \dot{A}^+(\underline{\boldsymbol{x}},t)-\dot{A}^-(\underline{\boldsymbol{x}},t) \tag{3.2.15}$$

inserting the term $\rho(\underline{\boldsymbol{x}},t)(\underline{\boldsymbol{\nabla}}\cdot\underline{\boldsymbol{v}}^k)$ which has a zero value due to the incompressible domain. This extra term allows $\underline{\boldsymbol{v}}^k$ terms to be grouped into $\underline{\boldsymbol{\nabla}}\cdot\left(\underline{\boldsymbol{v}}^k\rho(\underline{\boldsymbol{x}},t)\right)$ to give

$$\frac{\partial\rho(\underline{\boldsymbol{x}},t)}{\partial t} + \underline{\boldsymbol{\nabla}}\cdot\left(\underline{\boldsymbol{v}}^k\rho(\underline{\boldsymbol{x}},t)\right) + \underline{\boldsymbol{\nabla}}\cdot(\rho(\underline{\boldsymbol{x}},t)\underline{\boldsymbol{v}}(\boldsymbol{x},t)) = \dot{A}^+(\underline{\boldsymbol{x}},t) - \dot{A}^-(\underline{\boldsymbol{x}},t) \tag{3.2.16}$$

Assuming the material velocity is much less than velocity of dislocation field, $\underline{\boldsymbol{\nabla}}\cdot\left(\boldsymbol{v}^k\rho(\underline{\boldsymbol{x}},t)\right) \ll \underline{\boldsymbol{\nabla}}\cdot(\rho(\underline{\boldsymbol{x}},t)\boldsymbol{v}(\underline{\boldsymbol{x}},t))$, it is removed from Equation (3.2.16) and the evolution of the dislocation density field is modelled in the present research by solving the following partial differential equation

$$\frac{\partial\rho(\underline{\boldsymbol{x}},t)}{\partial t} + \underline{\boldsymbol{\nabla}}\cdot(\rho(\underline{\boldsymbol{x}},t)\underline{\boldsymbol{v}}(\underline{\boldsymbol{x}},t)) = \dot{A}^+(\underline{\boldsymbol{x}},t) - \dot{A}^-(\underline{\boldsymbol{x}},t) \tag{3.2.17}$$

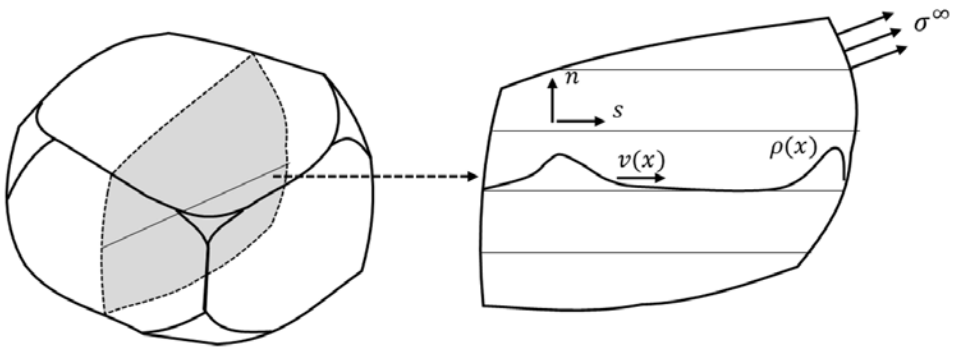

Figure 3.2.3: Sketch of the dislocation density on a slip plane

Consider a cross section of a grain, Figure 3.2.3, the dislocation density for a given slip system can be evolved depending on the applied stress and interaction with surrounding density on other slip systems. If accounting for mixed dislocation densities the following expressions are required for transport of the scalar dislocation field for both the positive $\rho^{+}(\underline{\boldsymbol{x}}, t)$ and negative $\rho^{-}(\underline{\boldsymbol{x}}, t)$ dislocation distributions

$$\frac{\partial \rho^{+}(\underline{\boldsymbol{x}}, t)}{\partial t} + \underline{\boldsymbol{\nabla}} \cdot \left(\rho^{+}(\underline{\boldsymbol{x}}, t) \underline{\boldsymbol{v}}(\underline{\boldsymbol{x}}, t) \right) = \dot{A}^{+}(\underline{\boldsymbol{x}}, t) - \dot{A}^{-}(\underline{\boldsymbol{x}}, t) \tag{3.2.18}$$

$$\frac{\partial \rho^{-}(\underline{\boldsymbol{x}}, t)}{\partial t} - \underline{\boldsymbol{\nabla}} \cdot \left(\rho^{-}(\underline{\boldsymbol{x}}, t) \underline{\boldsymbol{v}}(\underline{\boldsymbol{x}}, t) \right) = \dot{A}^{+}(\underline{\boldsymbol{x}}, t) - \dot{A}^{-}(\underline{\boldsymbol{x}}, t) \tag{3.2.19}$$

The positive and negative density fields are propagated separately but share the same force field although the force experienced for the opposite sign burgers vector distributions are inverted. Equation (3.2.18) and Equation (3.2.19) are solved numerically using a finite differencing approximations described in Chapter 4 to evolve the dislocation density distributions.

The velocity of the dislocations is dependent on the force acting on the dislocation. The Peach-Koehler equation describes how the stress field is translated into the force field, $\boldsymbol{f}(\underline{\boldsymbol{x}}, t)$,

acting on the dislocation in the glide direction

$$\underline{\boldsymbol{f}}(\underline{\boldsymbol{x}},t) = \underline{\boldsymbol{t}} \times \underline{\underline{\boldsymbol{\sigma}}}(\underline{\boldsymbol{x}},t) \cdot \underline{\boldsymbol{b}} \tag{3.2.20}$$

where the micro-stress field, $\underline{\underline{\boldsymbol{\sigma}}}(\underline{\boldsymbol{x}},t)$, formed of two stress components which influence dislocation motion including; the externally applied stress on the material, $\underline{\underline{\boldsymbol{\sigma}}}^{\infty}(\underline{\boldsymbol{x}},t)$, the internal dislocation stress fields, $\underline{\underline{\boldsymbol{\sigma}}}^{d}(\underline{\boldsymbol{x}},t)$. The velocity field components resolved onto the slip plane dictate the rate of propagation of $\rho(\underline{\boldsymbol{x}},t)$ in the glide direction and how the density evolves. The driving force felt by the dislocation is calculated by putting the components of the externally applied stress tensor and internal stress field due to the dislocations acting on the dislocation into the Peach-Koehler equation (3.2.20) to give

$$\underline{\boldsymbol{f}}(\underline{\boldsymbol{x}},t) = \underline{\boldsymbol{t}} \times \left[\underline{\underline{\boldsymbol{\sigma}}}^{\infty}(\underline{\boldsymbol{x}},t) + \underline{\underline{\boldsymbol{\sigma}}}^{d}(\underline{\boldsymbol{x}},t) \right] \cdot \underline{\boldsymbol{b}} \tag{3.2.21}$$

resolving the force applied to the slip direction of the dislocation. The treatment of the dislocation density stress field is essential to the FDM theory.

3.3 Two-dimensional theory

The stress fields of the dislocations create compressive and tensile fields either side of themselves causing attraction and repulsion between other dislocations. A point within the domain will be influenced by the sum of all the stress field components acting on the point. These stress fields are long range but are much stronger at close range, the effect which is observed through events like dislocation pile-up. To obtain the full stress map of the domain the internal stress fields generated from every point were calculated and summed across the domain.

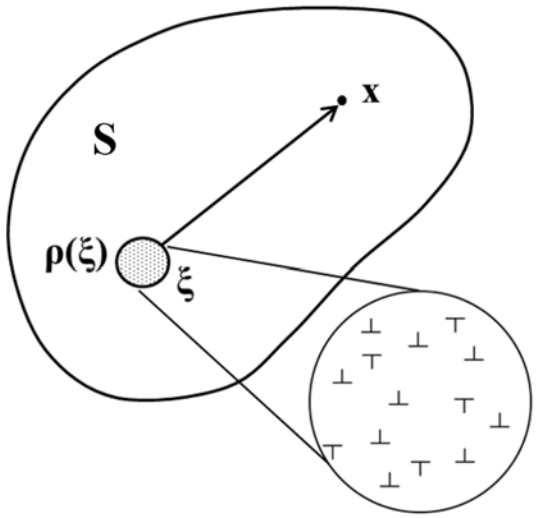

Figure 3.3.1: Displays an area S where a 'super-dislocation' at $\boldsymbol{\xi}$ with a dislocation density $\rho(\boldsymbol{\xi})$ influencing a point $\boldsymbol{x}$

To calculate the total internal stress field for any given point within our area S, see Figure 3.3.1, the stress field exerted on the density at $\underline{\boldsymbol{x}}$ by all surrounding density distribution at $\rho(\underline{\boldsymbol{\xi}}, t)$ for $\underline{\boldsymbol{\xi}} \neq \underline{\boldsymbol{x}}$ was calculated. Taking the combined Burgers vector of the point as $d\underline{\boldsymbol{b}} = \underline{\boldsymbol{b}}\rho(\underline{\boldsymbol{\xi}}, t)dS$, where $\rho(\underline{\boldsymbol{\xi}}, t)dS$ is the number of dislocations at that point. Thus the infinitesimal stress field at a point $\underline{\boldsymbol{x}}$ is given by

$$\begin{aligned} d\underline{\underline{\boldsymbol{\sigma}}}^d(\underline{\boldsymbol{x}}, t) &= \frac{\mu d\underline{\boldsymbol{b}}}{2\pi(1-\nu)}\underline{\boldsymbol{g}}(\underline{\boldsymbol{x}} - \underline{\boldsymbol{\xi}}, t) \\ &= \frac{\mu \underline{\boldsymbol{b}}}{2\pi(1-\nu)}\rho(\underline{\boldsymbol{\xi}}, t)\underline{\boldsymbol{g}}(\underline{\boldsymbol{x}} - \underline{\boldsymbol{\xi}}, t)dS \end{aligned} \tag{3.3.1}$$

where $\underline{\boldsymbol{g}}(\underline{\boldsymbol{x}} - \underline{\boldsymbol{\xi}}, t)$ represents the stress component matrix for edge dislocations. This theory assumes that the configuration of dislocations at any density has the same stress fields as that of a single edge dislocation scaled by the density value. The stress components of edge dislocation stress tensor are as follows

$$g_{11}(\underline{\boldsymbol{x}} - \underline{\boldsymbol{\xi}}) = \frac{(y-y')(3(x+x')^2 + (y-y')^2)}{((x-x')^2 + (y-y')^2)^2} \tag{3.3.2}$$

$$g_{22}(\underline{\boldsymbol{x}}-\underline{\boldsymbol{\xi}})=\frac{(y-y')((x+x')^2-(y-y')^2)}{((x-x')^2+(y-y')^2)^2} \tag{3.3.3}$$

$$g_{12}(\underline{\boldsymbol{x}}-\underline{\boldsymbol{\xi}})=g_{21}(\underline{\boldsymbol{x}}-\underline{\boldsymbol{\xi}})=\frac{(x-x')((x-x')^2-(y-y')^2)}{((x-x')^2+(y-y')^2)^2} \tag{3.3.4}$$

$$g_{33}(\underline{\boldsymbol{x}}-\underline{\boldsymbol{\xi}})=\nu(g_{11}(\underline{\boldsymbol{x}}-\underline{\boldsymbol{\xi}})+g_{22}(\underline{\boldsymbol{x}}-\underline{\boldsymbol{\xi}})) \tag{3.3.5}$$

$$g_{31}(\underline{\boldsymbol{x}}-\underline{\boldsymbol{\xi}})=g_{13}(\underline{\boldsymbol{x}}-\underline{\boldsymbol{\xi}})=g_{23}(\underline{\boldsymbol{x}}-\underline{\boldsymbol{\xi}})=g_{32}(\underline{\boldsymbol{x}}-\underline{\boldsymbol{\xi}})=0 \tag{3.3.6}$$

where $\underline{\boldsymbol{x}}=(x,y)$ is the position the stress component is being calculated from a dislocation at position $\underline{\boldsymbol{\xi}}=(x',y')$. Equation (3.3.1) represents the stress of an infinitesimal area segment, it was integrated to obtain the magnitude of the stress fields generated by all points $\rho(\underline{\boldsymbol{\xi}},t)$ acting on a point $\underline{\boldsymbol{x}}$ for $\underline{\boldsymbol{\xi}}\neq\underline{\boldsymbol{x}}$,

$$\underline{\underline{\boldsymbol{\sigma}}}^d(\underline{\boldsymbol{x}},t)=\frac{\mu\underline{\boldsymbol{b}}}{2\pi(1-\nu)}\iint_\Omega\rho(\underline{\boldsymbol{\xi}},t)\underline{\boldsymbol{g}}(\underline{\boldsymbol{x}}-\underline{\boldsymbol{\xi}},t)dS \tag{3.3.7}$$

The net stress field exerted by the dislocation density distribution is calculated for every point in the domain. This non-local theory makes the stress at single point dependent on the combined interaction of all the other points in the domain containing dislocations. The stress calculated in Equation (3.3.7) was used to calculate the dislocation field force on $\underline{\boldsymbol{x}}$ by substituting it into Equation (3.2.20) for the Peach-Koehler force to give

$$\underline{\boldsymbol{f}}^d(\underline{\boldsymbol{x}},t)=\frac{\mu\underline{\boldsymbol{b}}}{2\pi(1-\nu)}\iint_\Omega\rho(\underline{\boldsymbol{\xi}},t)\big[\underline{\boldsymbol{t}}\times\underline{\boldsymbol{g}}(\underline{\boldsymbol{x}}-\underline{\boldsymbol{\xi}},t)\cdot\underline{\boldsymbol{b}}\big]dS \tag{3.3.8}$$

For a single slip system of parallel straight edge dislocations the term, $\underline{\boldsymbol{t}}\times\underline{\boldsymbol{g}}(\underline{\boldsymbol{x}}-\underline{\boldsymbol{\xi}},t)\cdot\underline{\boldsymbol{b}}$, reduces down to the g_{12} component of the dislocation stress field given by Equation (3.3.4). The force due to the internal dislocation stress fields for the two-dimensional theory is calculated by solving

$$\underline{\boldsymbol{f}}^d(\underline{\boldsymbol{x}},t)=\frac{\mu\underline{\boldsymbol{b}}}{2\pi(1-\nu)}\iint\rho(\underline{\boldsymbol{\xi}},t)\frac{(x-x')((x-x')^2-(y-y')^2)}{((x-x')^2+(y-y')^2)^2}dx'dy' \tag{3.3.9}$$

The dislocation fields for positive and negative edge dislocations, $\rho^{+}(\boldsymbol{x},t)$ and $\rho^{-}(\boldsymbol{x},t)$, have inverted velocity fields of one another and move in the opposite direction under an applied load due to their Burgers vector orientation. At positions that have positive and negative dislocation densities the stress field is calculated for the net density $\rho(\underline{\boldsymbol{\xi}},t)=\rho^{+}(\underline{\boldsymbol{\xi}},t)-\rho^{-}(\underline{\boldsymbol{\xi}},t)$. This is the case for single slip system of parallel dislocation density but the field dislocation mechanics code does include all possible stress components in calculations to allow for the expansion of the code to multiple slip systems and rotating the simulation domain.

The integral of internal dislocation stress field components in Equation (3.3.9) was solved using numerical integration techniques. The internal dislocation stress field component governs self interaction dislocation density distributions, this changes the shape of the distribution. This results in the dispersion of the high concentration peaks in the dislocation density distribution, as well as pinning of dislocations due to stress fields of the opposite sign burgers vector dislocation distribution.

3.4 Dislocation mobility

In Nickel-based superalloys there are two glide mechanisms to be considered for the edge dislocations; drag controlled glide and jog controlled glide. These control the mobility of the dislocations under the applied force. The glide velocity, $\underline{\boldsymbol{v}}^{g}$, depends whether the the dislocation is moving under drag controlled or job controlled glide. It was implemented that the dislocation mobility that created the slower velocity under a given stress was used as the mobility. So if $\underline{\boldsymbol{v}}_{drag}(\underline{\boldsymbol{x}},t)<\underline{\boldsymbol{v}}_{jog}(\underline{\boldsymbol{x}},t)$ then $\underline{\boldsymbol{v}}^{g}(\underline{\boldsymbol{x}},t)=\underline{\boldsymbol{v}}_{drag}(\underline{\boldsymbol{x}},t)$, and if $\underline{\boldsymbol{v}}_{jog}(\underline{\boldsymbol{x}},t)<\underline{\boldsymbol{v}}_{drag}(\underline{\boldsymbol{x}},t)$ then $\underline{\boldsymbol{v}}^{g}(\underline{\boldsymbol{x}},t)=\underline{\boldsymbol{v}}_{jog}(\underline{\boldsymbol{x}},t)$. In practice this meant jog controlled glide was dominant at low stresses and then quickly accelerate to the lattice drag, which takes over as the dominant form of drag. Figure 3.4.1 illustrates the transition from jog controlled to drag controlled glide.

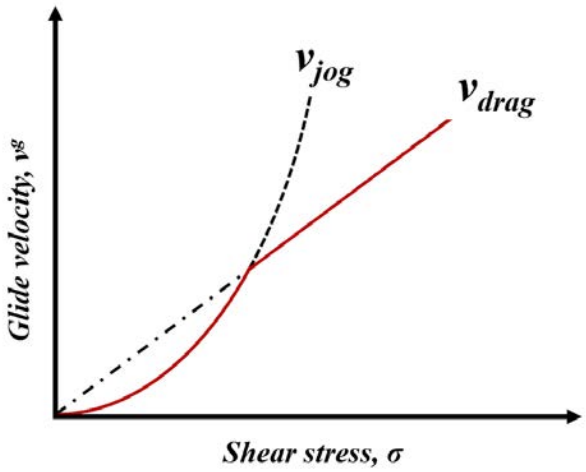

Figure 3.4.1: Velocity profile of the dislocation field (red line), transition from job controlled glide to drag controlled glide.

Within the superalloy microstructure there are numerous obstacles which impede the motion of dislocations. The primary obstacle to dislocations in superalloys are the strengthening γ' precipitates. There are mechanisms for the dislocations to move through or around γ' precipitates given the correct conditions, which were characterised in the continuum model for an accurate propagation of the dislocation density and are described. These interactions give rise to the line tension, $\underline{\boldsymbol{f}}^{lt}$ working against the external shear stress and internal stress field components. The motive force, $\underline{\boldsymbol{f}}^{mot}$, is the sum of the forces acting on the dislocations.

$$\underline{\boldsymbol{f}}^{mot} = \underline{\boldsymbol{f}}^{\infty} + \underline{\boldsymbol{f}}^{d} - \underline{\boldsymbol{f}}^{lt} \tag{3.4.1}$$

If $\underline{\boldsymbol{f}}^{\infty} + \underline{\boldsymbol{f}}^{d} < \underline{\boldsymbol{f}}^{lt}$ the dislocation remains immobile.

3.4.1 Drag controlled glide

Under drag controlled glide the dislocation moves at a speed $\underline{\boldsymbol{v}}(\underline{\boldsymbol{x}}, t) = M\underline{\boldsymbol{f}}(\underline{\boldsymbol{x}}, t) \cdot \underline{\boldsymbol{s}}$, where the drag mobility, M, describes the the phonon drag on the dislocation interacting with the thermal vibrations of the crystal lattice. The drag mobility can also be described as the

drag coefficient, B, related by, $B = 1/M$. It acts on the dislocation segment where the jog spacing λ_{jog} is equal or greater than the minimum particle spacing λ_{min}. The drag mobility can be calculated by

$$M = \frac{1}{kT} v_{sound} \left(\frac{3a_v^2}{4\pi} \right)^{1/3} \tag{3.4.2}$$

where v_{sound} is the velocity of sound in the alloy and a_v is the atomic volume.

3.4.2 Jog controlled glide

Jogs are a dislocation line segment climbing out of the glide plane, and also prevent glide of dislocations contributing to dislocation curvature in the slip plane, the average jog spacing, λ_{jog}, is incorporated into line tension calculations [15].

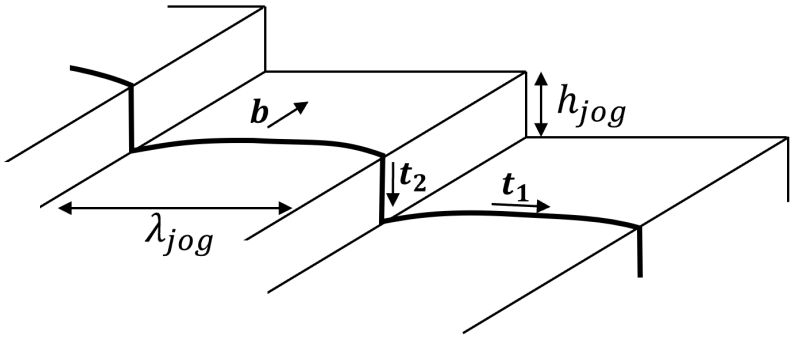

Figure 3.4.2: Schematic of dislocation line with jogs spaced at intervals, λ_{jog}, the line vector in the glide plane, $\boldsymbol{t}_1$, and the line vector of the perpendicular jog, $\boldsymbol{t}_2$.

Where the jog spacing is less that the minimum particle spacing it has a large effect on the mobility slowing the movement of the dislocation segments. The jogs can only propagate in the direction of the burgers vector of the dislocation line by the diffusion of vacancies given their orientation, see Figure 3.4.2. The diffusion of jogs limits the speed at which the dislocation line can move such that the jog velocity is described by

$$\underline{\boldsymbol{v}}_{jog} = \frac{4\pi D_s}{h_{jog}} \left[exp\left(\underline{\boldsymbol{s}} \cdot \underline{\boldsymbol{f}}(\underline{\boldsymbol{x}}, t) \frac{\underline{\boldsymbol{b}} \lambda_{jog}}{kT} \right) - 1 \right] \tag{3.4.3}$$

where the term $\underline{\boldsymbol{s}} \cdot \underline{\boldsymbol{f}}(\underline{\boldsymbol{x}}, t)$ is the force component resolved in the glide direction, D_s is the diffusivity and h_{jog} is the height of the jog.

3.4.3 Dislocation climb

One mechanism to get around obstacles is thermally activated climb which if the movement of the dislocation perpendicular to its slip plane at γ/γ' interface with the particle. Climb occurs by the diffusion of vacancies either emmitted or absorbed by the dislocation. If vacancies diffuse towards the dislocation, the extra half plane above the dislocation shifts up one plane resulting in positive climb. If the vacancy forms at the dislocation and diffuses away moving the dislocation down one atomic plane results in negative climb [15]. The velocity of the vacancy diffusion is described by,

$$\underline{\boldsymbol{v}}_{cl}(\underline{\boldsymbol{x}}, t) = \frac{4\pi D_s}{\underline{\boldsymbol{b}}} \left[\exp\left(\frac{\underline{\boldsymbol{n}} \cdot \underline{\boldsymbol{f}}(\underline{\boldsymbol{x}}, t) a_v}{\underline{\boldsymbol{b}} kT} \right) - 1 \right] \tag{3.4.4}$$

and $\underline{\boldsymbol{n}} \cdot \underline{\boldsymbol{f}}(\underline{\boldsymbol{x}}, t)$ is the climb force which is the force resolved along the normal of the slip plane. The thermally controlled diffusivity,

$$D_s = D_{s0} \exp\left(\frac{-Q}{kT} \right) \tag{3.4.5}$$

depends on the activation energy Q. The dislocation can only climb when it cannot glide thus occurs when dislocations are immobilised at precipitates and dislocation junctions. In the continuum model the climb applies to the density as it would a single dislocation, and it is assumed that the positive and negative dislocations experience positive and negative climb respectively.

3.5 Line tension and γ' precipitate shearing

The key feature of the FDM theory is to capture the interaction between the dislocations and γ' distribution. Although the model simulates infinitesimal dislocation segments it is important to capture the mobility of the dislocation segment relative to the dislocation line interaction with out of plane γ' particles.

The dislocation mobility is limited by the force due to the line tension, $\underline{\boldsymbol{f}}^{lt}(\underline{\boldsymbol{x}}, t)$, and drag terms from the matrix, obstacles and jogs pinning the dislocation line. This accounts for the motion of the dislocation perpendicular to the simulation domain. The force of the line tension comes from the curvature of the dislocation trying to straighten and minimise energy [81]. It is defined by the curvature of the dislocation line between pinning obstacles, these include precipitate particles and jogs, described by $\kappa(\underline{\boldsymbol{x}}, t)$. Line tension is the force that is required to expand the dislocation loop moving the edge dislocations through the bimodal distribution, modelled across the simulation domain. Moving through the bimodal particle distribution of the superalloy the dislocation line segments are pinned by the precipitates. The curvature of the bowing dislocation line segments, $\kappa(\underline{\boldsymbol{x}}, t)$, and line energy, approximated at $\Gamma = 0.5\mu b^2$, gives the line tension force. The tension force acting on the dislocation density to be overcome the dislocation density to glide is given by

$$\underline{\boldsymbol{f}}^{lt} = -\Gamma\kappa(\underline{\boldsymbol{x}}, t)\underline{\boldsymbol{s}} \tag{3.5.1}$$

The curvature is inversely proportional to the dislocation chord radius, R,

$$\kappa(\underline{\boldsymbol{x}}, t) = 1/R \tag{3.5.2}$$

and the chord radius is a function of the chord height, H, and the particle spacing as shown in Figure 3.5.1. Written here for the spacing of secondary γ' particles

$$R = \frac{H}{2} + \frac{\lambda_s^2}{8H} \tag{3.5.3}$$

where λ_s is the spacing of the secondary γ' particles. The chord height is how far the dislocation bows forward between the pinning particles under the force acting in the glide direction

$$H = \frac{f_x \lambda_s^2}{8\Gamma} \tag{3.5.4}$$

The line tension varies with the spacing, depending if the stress acting on the dislocations is sufficient to cut the γ' particles. If the stress is less than the cutting stress for the tertiary γ' particles then the space is that of the tertiary particles, λ_t. If the stress is large enough to cut the tertiary particles but not the secondary particles then the spacing λ_t. When the stress is large enough to cut the secondary particles then the spacing is defined as the size of the grain.

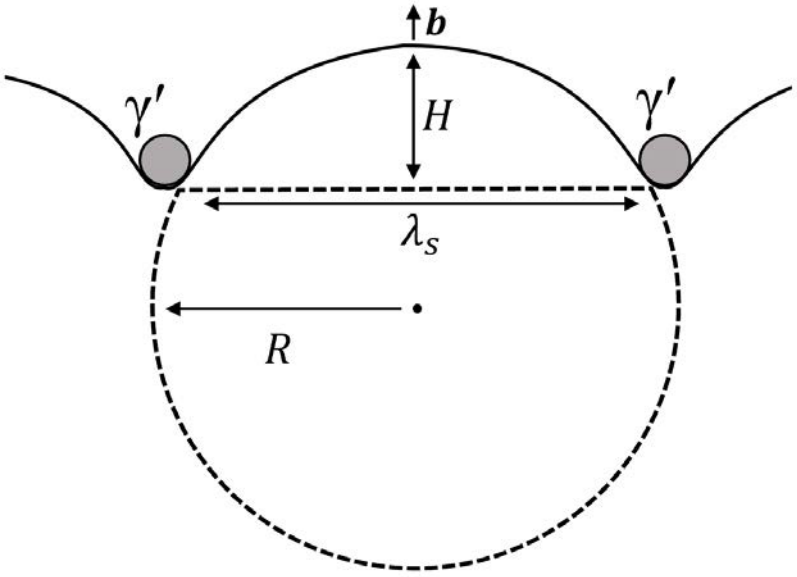

Figure 3.5.1: Schematic for the line tension of a dislocation line segment bowing between two γ' particles. The radius of the arc segment of the dislocation, R, which bows past the dislocations by distance H.

The mechanism dislocations use to pass particles is by shearing, or cutting, by overcoming the anti-phase boundary energy, E_{APB}. When the dislocation shears the particle it creates an anti-phase boundary along the slip plane in the structure having shifted the ordered precipitate structure. Dislocations move through in pairs with the following dislocation restoring the ordered structure of the precipitate. The γ' have a different $L1_2$ atomic arrangement to the γ matrix thus dislocations require an increase in the force to shear the particles, the criteria to cut the particles is described by

$$\tau_c = \frac{2R_s}{\lambda_s} E_{APB} \tag{3.5.5}$$

the dimensions R_s and λ_s are illustrated in Figure 3.5.2. The force required to shear the particle varies as a function of particle radius and spacing.

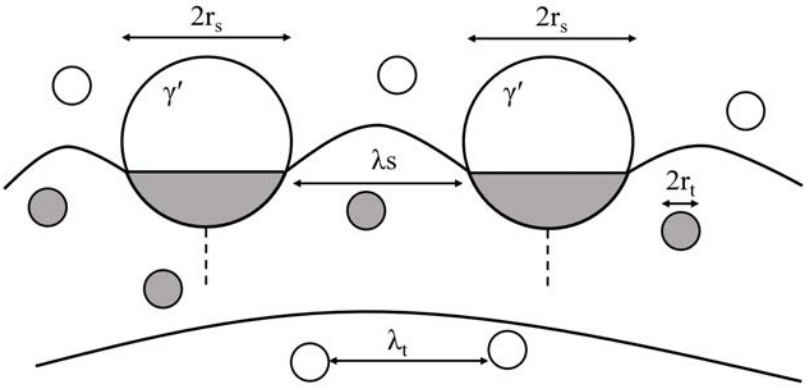

Figure 3.5.2: Schematic of precipitate particle shear

The particle spacing is calculated by the volume fraction ϕ_s and a mean particle radius R_s and the anti-phase boundary energy, E_{APB},

$$\lambda_s = 2R_s \left(\left(\frac{\pi}{4\phi_s} \right)^{1/2} - 1 \right) + 2R_s \tag{3.5.6}$$

3.6 Deformation kinematics

This section describes how the evolution of the dislocation field is used to update the stress state of the domain using the shear created by the dislocations. The link from the field dislocation mechanics to the deformation kinematics is bridged by the relation for the plastic velocity gradient tensor

$$\underline{\underline{\boldsymbol{L}}}^p = \dot{\gamma}(\underline{\boldsymbol{x}}, t)\underline{\boldsymbol{s}} \cdot \underline{\boldsymbol{n}} \tag{3.6.1}$$

where $\dot{\gamma}$ is the shear rate on an active slip system, $\boldsymbol{s}$ the slip direction and $\boldsymbol{n}$ the slip normal. Taking the dislocation field and corresponding velocity field the shear rate was calculated.

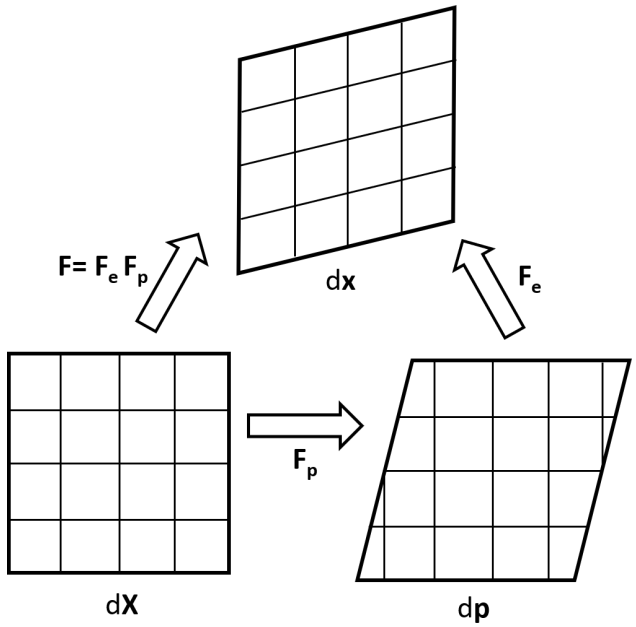

Figure 3.6.1: Lee multiplicative decomposition showing deformation of a crystal lattice in and initial state $d\boldsymbol{X}$ to the final deformed state $d\boldsymbol{x}$ via the intermediate plastic deformation state $d\boldsymbol{p}$.

Consider a material domain defined by a collection of points $\underline{\boldsymbol{X}}$ to be an initial configuration. Suppose that a deformation is imposed on the material such that it now is the current configuration described by the collection of points $\underline{\boldsymbol{x}}$. The mapping of the points from the initial to the final configurations is given by the total deformation gradient $\underline{\underline{\boldsymbol{F}}} = d\underline{\boldsymbol{x}}/d\underline{\boldsymbol{X}}$, where a neighbourhood $d\underline{\boldsymbol{X}}$ in the initial state is mapped to a neighbourhood $d\underline{\boldsymbol{x}}$ in the final state. To account for plastic distortions it is convenient to introduce an imtermediate configuration associated with the advection of the dislocation field [82]. Thus there is a transformation $\underline{\underline{\boldsymbol{F}}}^p$ which maps a point $\underline{\boldsymbol{X}}$ in the initial configuration to $\underline{\boldsymbol{p}}$ in the intermediate state, see Figure 3.6.1. The mapping of points $\underline{\boldsymbol{p}}$ to the final state is given by $\underline{\underline{\boldsymbol{F}}}^e$, which describes the elastic distortions. This is Lee's multiplicative decomposition of the total distortions into elastic and plastic contributions. Mathematically this is given by

$$d\underline{\boldsymbol{p}} = \underline{\underline{\boldsymbol{F}}}^p d\underline{\boldsymbol{X}} \tag{3.6.2}$$

$$d\underline{\boldsymbol{x}} = \underline{\underline{\boldsymbol{F}}}^e d\underline{\boldsymbol{p}} \tag{3.6.3}$$

$$\begin{aligned} d\underline{\boldsymbol{x}} &= \underline{\underline{\boldsymbol{F}}}^e \underline{\underline{\boldsymbol{F}}}^p d\underline{\boldsymbol{X}} \\ &= \frac{\partial \underline{\boldsymbol{x}}}{\partial \underline{\boldsymbol{p}}} \frac{\partial \underline{\boldsymbol{p}}}{\partial \underline{\boldsymbol{X}}} d\underline{\boldsymbol{X}} \\ &= \frac{\partial \underline{\boldsymbol{x}}}{\partial \underline{\boldsymbol{X}}} d\underline{\boldsymbol{X}} \\ &= \underline{\underline{\boldsymbol{F}}} d\underline{\boldsymbol{X}} \end{aligned} \tag{3.6.4}$$

The velocity gradient tensor, $\underline{\underline{\boldsymbol{L}}}$, is the rate of change of deformation gradient [83]. $\underline{\underline{\boldsymbol{L}}}^p$ is the plastic component of this coming for the plastic deformation gradients

$$\underline{\underline{\boldsymbol{L}}}^p = \dot{\underline{\underline{\boldsymbol{F}}}}^p \underline{\underline{\boldsymbol{F}}}^{(p)-1} \tag{3.6.5}$$

By solving Equation(3.6.5) for the plastic deformation gradient, $\underline{\underline{\boldsymbol{F}}}^p$, the elastic deformation gradient is obtained from $\underline{\underline{\boldsymbol{F}}}^e = \underline{\underline{\boldsymbol{F}}}\underline{\underline{\boldsymbol{F}}}^{(p)-1}$. The Cauchy-Green tensor describes the measure of how length of line elements and the angles between them change between configurations is given by $\underline{\underline{\boldsymbol{G}}} = \underline{\underline{\boldsymbol{F}}}^T \underline{\underline{\boldsymbol{F}}}$ [83]. The Green-Lagrange strain tensor was used to update the elastic strain using the Cauchy-Green tensor

$$\underline{\underline{\boldsymbol{E}}} = \frac{1}{2}\left(\underline{\underline{\boldsymbol{F}}}^{(e)T} \underline{\underline{\boldsymbol{F}}}^e - \underline{\underline{\mathbb{I}}}\right) \tag{3.6.6}$$

where $\underline{\underline{\mathbb{I}}}$ is the identity tensor. The new elastic strain calculated by Equation (3.6.6) is used to update the micro stress field, $\underline{\underline{\boldsymbol{\sigma}}}$, using the constitutive equation

$$\underline{\underline{\boldsymbol{\sigma}}} = \underline{\underline{\underline{\underline{\boldsymbol{C}}}}} : \frac{1}{2}\left(\underline{\underline{\boldsymbol{F}}}^{(e)T} \underline{\underline{\boldsymbol{F}}}^e - \underline{\underline{\mathbb{I}}}\right) \tag{3.6.7}$$

Thus the newly propagated dislocation density directly influences the crystal plasticity calculations through Equation (3.6.1) used to update the deformation gradient which is in turn used to update the stress through Equation (3.6.7).

Chapter 4

Numerical implementation

This chapter focuses on the numerical implementation for solving the FDM framework. Firstly the finite difference method used to solve the continuity equation is presented. Then the simulation set-up is presented to give the scenario in which the FDM model is applied and the sequence the equations in Chapter 3 are calculated. Following this integration of the FDM code with the commercial finite element (FE) software, ABAQUS, is described. This was introduced to produce the boundary conditions to the simulation domain and provide the deformation. This includes the set-up of the square simulation domain, how the load is applied, the relationship between the FE and FDM calculations and how they interact. The microstructural distributions and γ matrix and γ' properties are then presented. Explaining dimensions and volume fraction of the γ' particles used and how the particle dispersions are produced. The assumed behaviour of the dislocations between the γ matrix and γ' particles stated. Finally the key parameters and material constants used in the simulations are listed.

4.1 Finite difference method

The dislocation field evolution described by Equation (3.2.18) and Equation (3.2.19) cannot be solved analytically. These partial differential equations were solved using a finite difference

method and gradient approximations. A few finite difference methods were tested to find the one that produced the most stable solutions. The Gauss-Seidel method was chosen to solve the dislocation transport equation creating the most stable solutions. For a function represented by ϕ it takes the basic form

$$\phi_i^{(k+1)} = \frac{1}{a_{i,i}} \left(\sum_{j=1}^{n} a_{i,j}\phi_j^{(k)} - \sum_{j=1}^{i-1} a_{i,j}\phi_j^{(k+1)} - \sum_{j=i+1}^{n} a_{i,j}\phi_j^{(k)} \right) \quad (i = 1, 2, ..., n) \tag{4.1.1}$$

where $a_{i,j}$ represent matrix coefficients, $(k+1)$ indicates the value from the current iteration and (k) the previous [84]. The updated values are compared against the previous iteration to create residuals which are checked to be within a tolerance, if outside the tolerance another iteration is completed and the residuals checked again until convergence is achieved. If the solution did not converge within a set number of iterations the timestep is reduced and the iterative procedure is repeated.

To obtain the gradient of the dislocation flux, $\nabla J(x_{i,j}, t) = \nabla \left(\rho(x_{i,j}, t)v(x_{i,j}, t)\right)$, gradient approximations were applied opposite to the direction the velocity field was acting at the point $x_{i,j}$ being updated, this is the upwind approach. The data points used in the approximations are shown in Figure 4.1.1. The following forwards and backwards gradient two-point approximations were used;

$$\nabla J(x_i, t) = \frac{1}{dx} \left(\rho(x_{i+1}, t)v(x_{i+1}, t) - \rho(x_i, t)v(x_i, t)\right) \tag{4.1.2}$$

$$\nabla J(x_i, t) = \frac{1}{dx} \left(\rho(x_i, t)v(x_i, t) - \rho(x_{i-1}, t)v(x_{i-1}, t)\right) \tag{4.1.3}$$

The equivalent three point forwards and backwards numerical gradient approximations were used within the γ matrix and whenever enough points were available to produce more accu-

rate approximations

$$\nabla J(x_i,t) = \frac{1}{2dx}\left(-3\rho(x_i,t)v(x_i,t) + 4\rho(x_{i+1},t)v(x_{i+1},t) - \rho(x_{i+2},t)v(x_{i+2},t)\right) \tag{4.1.4}$$

$$\nabla J(x_i,t) = \frac{1}{2dx}\left(3\rho(x_i,t)v(x_i,t) - 4\rho(x_{i-1},t)v(x_{i-1},t) + \rho(x_{i-2},t)v(x_{i-2},t)\right) \tag{4.1.5}$$

The grid of values is updated in a sweeping pattern when scanning the array from $i = 1$ to $i = N$ and $j = 1$ to $j = N$. When calculating the value for $\rho(x_{i,j}, t + dt)$ if sampling points at positions less than the current i or j will use an already updated value for the iteration, and if sampling points at positions greater than the current i or j will use the value from the previous iteration, this is shown in Figure 4.1.1. The two point numerical differentiation methods were used within obstacles and near boundaries where the three point methods were not suitable due to the number of available points in the direction being sampled. Note at the edge of the simulation domain approximations are taken in the direction with available data points. The code has been designed to select the gradient approximations to minimise the truncation error wherever possible.

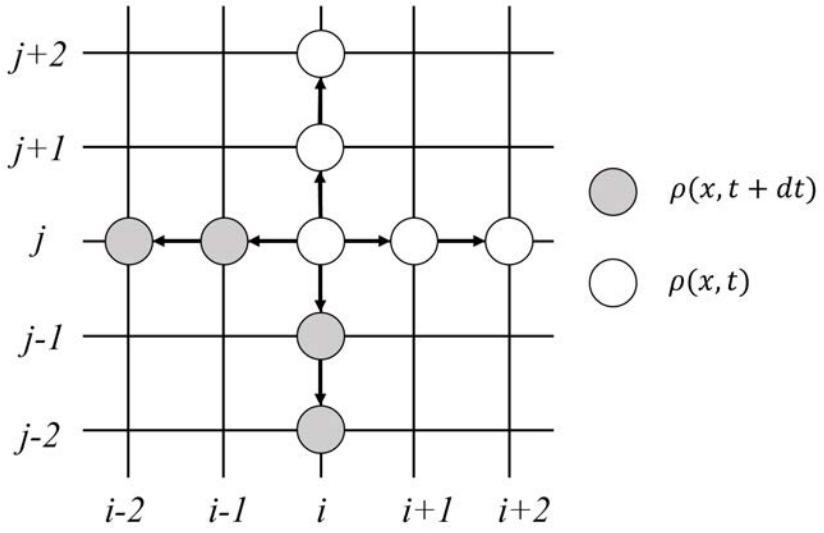

Figure 4.1.1: Sketch demonstrating the points used in the numerical gradient approximation for $\rho(x_{i,j}, t + dt)$

Substituting the spatial and temporal gradient approximations into Equation (3.2.17) for the dislocation field evolution, the new equation was rearranged for the updated dislocation density field at the next time increment

$$\rho(x_{i,j}, t + dt) = dt \left[-\nabla \cdot (\rho(x_{i,j}, t) v(x_{i,j}, t)) + \dot{A}^{+}(x_{i,j}, t) - \dot{A}^{-}(x_{i,j}, t) \right] \tag{4.1.6}$$

where the flux gradient, $\nabla \cdot (\rho(x_{i,j}, t) v(x_{i,j}, t))$, will differ depending on the number of points used in the approximation. For example at the grain boundaries or inside the secondary γ' particles resolved in the finite difference grid. An example of Equation (4.1.6) using a two point forward approximation for the flux would look like

$$\begin{aligned} \rho(x_{i,j}, t + dt) = & dt \Bigg[\frac{\rho(x_{i,j}, t) v(x_{i,j}, t) - \rho(x_{i+1,j}, t) v(x_{i+1,j}, t)}{dx} \\ & + \frac{\rho(x_{i,j}, t) v(x_{i,j}, t) - \rho(x_{i,j+1}, t) v(x_{i,j+1}, t)}{dy} + \dot{A}^{+}(x_{i,j}, t) - \dot{A}^{-}(x_{i,j}, t) \Bigg] \end{aligned} \tag{4.1.7}$$

where $dy = dx$ but indicates the gradient approximation in the y-direction. If the conditions are not suitable for climb, which is often the case, there is no climb velocity acting in the y-direction thus no gradient approximation. Another example of updated density using the a backwards three point approximation used if the velocity is acting in the positive x direction in the γ matrix between particles takes the form

$$\begin{aligned} \rho(x_{i,j}, t + dt) = & \\ & dt \Bigg[\frac{(3\rho(x_i, t) v(x_{i,j}, t) - 4\rho(x_{i-1,j}, t) v(x_{i-1,j}, t) + \rho(x_{i-2,j}, t) v(x_{i-2,j}, t))}{2dx} \\ & + \frac{(3\rho(x_{i,j}, t) v(x_{i,j}, t) - 4\rho(x_{i,j-1}, t) v(x_{i,j-1}, t) + \rho(x_{i,j-2}, t) v(x_{i,j-2}, t))}{2dx} \\ & + \dot{A}^{+}(x_{i,j}, t) - \dot{A}^{-}(x_{i,j}, t) \Bigg] \end{aligned} \tag{4.1.8}$$

The finite difference method was applied to solve Equation (4.1.6) for both the positive and negative dislocation fields separately. The reaction rate terms were calculated separately at the beginning of each timestep based on the initial distributions of positive and negative dislocations. Given the nature of the mathematics used to the solve the evolution equation for the dislocation field given by Equation (4.1.6) the simulation domain requires a grid to approximate the gradients. The grid points are a distance dx so the area the dislocation density value represents is dx^2. To focus on the field dislocation mechanics behaviour a simple square grid was used to represent a single square grain only where the internal stress field is influenced by its own dislocation distribution. The code was written in Fortran 77 as it compatible with the finite element software ABAQUS, used to create the loading conditions for the domain.

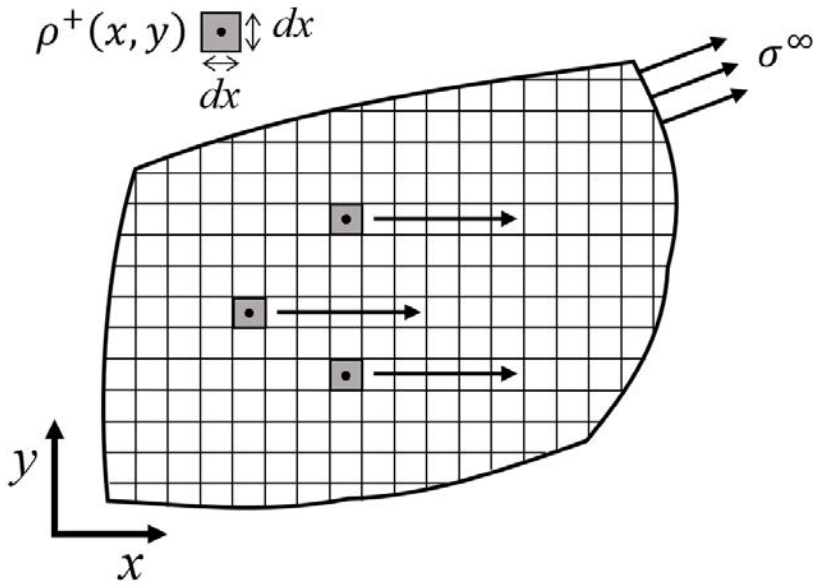

Figure 4.1.2: Sketch of a grain cross section divided into a grid to propagate the dislocation density, $\rho^+(x,y)$, using the finite difference method

Using the numerical gradient approximations to solve the evolution equation has limited the simulations to a single slip system where the the dislocation density travels parallel to the mesh directions. If the slip it oriented at different angles the density the approximations in the x and y axis 'bleeds' out of the slip direction rather than staying within the slip bands, resulting in the dislocations spreading out from the slip direction. The dislocations should only move out of plane by climb or cross-slip mechanism. Note that with the implicit method the gradient approximations of the flux uses both the updated and initial values for the dislocation density, but only the initial distribution of the velocity field for each timestep. This means after multiple iterations updating the dislocation field the velocity field of the dislocation field may not exactly correspond to that of the velocity field applied which is calculated before the finite difference calculations begin.

For the finite difference approximation to converge it needs to satisfy the Courant Friedrich Louis (CFL) condition,

$$\frac{|v|dt}{dx} \leq 1 \tag{4.1.9}$$

Given the scale of the FDM model a very small time step, starting at $dt = 1e^{-8}$, was required to capture the motion of the dislocation field in a the domain size of $5 - 10\mu m$ for solutions to converge accurately. Simulations with an incorrect timestep could see the collapse of distributions resulting in a sudden loss of dislocation density. Also given the speed of the dislocations relative to the domain size, with too large a timestep the dislocations can move too far between the calculations missing interactions with the microstructure or even moving outside of the domain. The applied load also influenced the timestep required as it directly influenced the velocity of the dislocation field.

Using the implicit Gauss-Seidel finite difference method sometimes resulted in a reduction of the timestep to propagate the dislocation field if it could not converge the new solution

within the tolerance limit. The timestep could drop to $dt = 1e^{-10}$ to converge the solutions but this meant that multiple iterations of the FDM code could take place between the finite element model timesteps, which created the new displacements on the domain.

4.2 FDM simulation set-up

All simulations of slip bands have been performed on a two-dimensional computational domain, such that the primary $[1\bar{1}0]$ slip direction is aligned with the x-axis, and [111] slip normal is oriented parallel the the y-axis. A domain length of $5\mu m$ and surface area $25\mu m^2$ was used as representative of a grain in fine grain RR1000. A schematic illustration of the model set-up is shown in Figure 4.2.1. Dislocation sources were placed on the vertical boundaries of the computational domain, with positive dislocation sources placed on the left boundary of the domain and negative dislocation sources on the right boundary. A Frank-Read generation mechanism is assumed with source lengths between $250\boldsymbol{b}$ and $350\boldsymbol{b}$ placed randomly along the vertical domain walls. A nucleation time, t_{nuc}, applies to a Frank-Read source, it signifies the time it takes for the dislocation to bow out to a critical distance to form a new dislocation loop. The dislocation velocity acting on the source influences the nucleation time, as the dislocation velocity increases from $1ms^{-1}$ to $100ms^{-1}$ the nucleation time decreases from $t_{nuc} = 37.5 \times 10^{-9}$s to $t_{nuc} = 0.375 \times 10^{-9}$s. The number of dislocations generated was calculated by dividing the timestep by the nucleation time. If the time step was decreased by a large amount to obtain a solution, this nucleation time was also tracked to prevent dislocations being generated too often. The mesh used to solve the finite difference scheme is shown in Figure 4.1.2. A mesh was required to propagate the dislocation field within the simulation domain. A mesh size $dx = 50nm$ was based on the numerical results of Chapter 5. The FDM simulations presented used a grid of 50×50 points in the majority of two dimensional calculations.

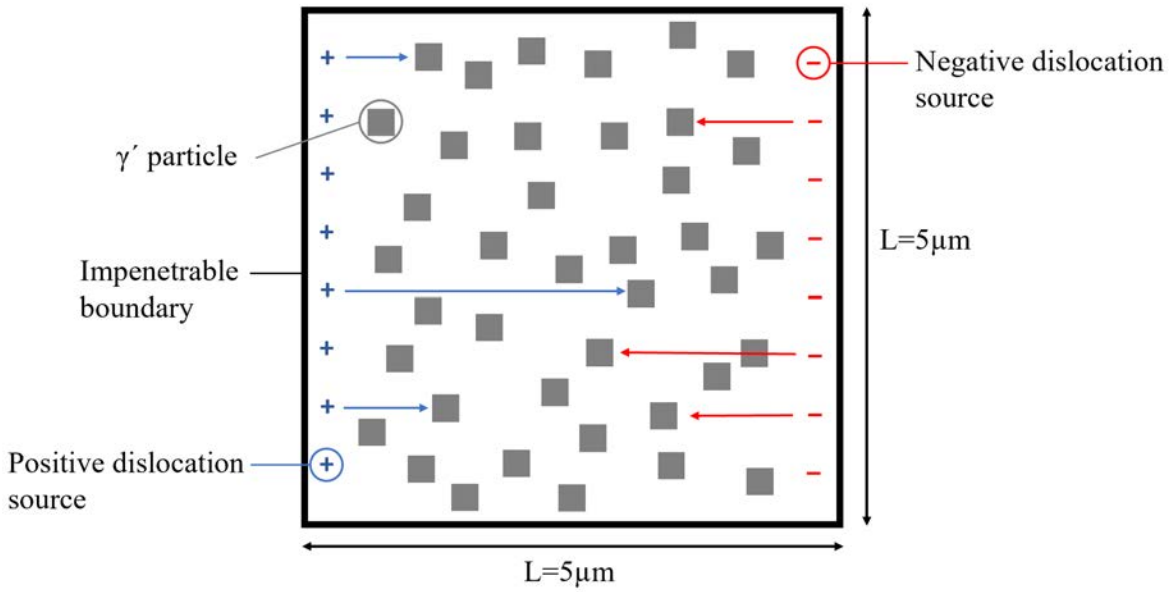

Figure 4.2.1: Sketch of simulation domain set-up

4.3 Coupling to finite element analysis

The commercial finite element software package ABAQUS was used to solve the quasi-equilibrium equations. A user-defined material subroutine (UMAT) was developed to solve for the micromechanical fields. This scheme was coupled to the finite difference scheme (section 4.1) used to solve the dislocation transport equation. The finite element model uses generalised plain strain elements with 'CPEG4R' elements: the four node quadrilateral, reduced integration with hourglass control.

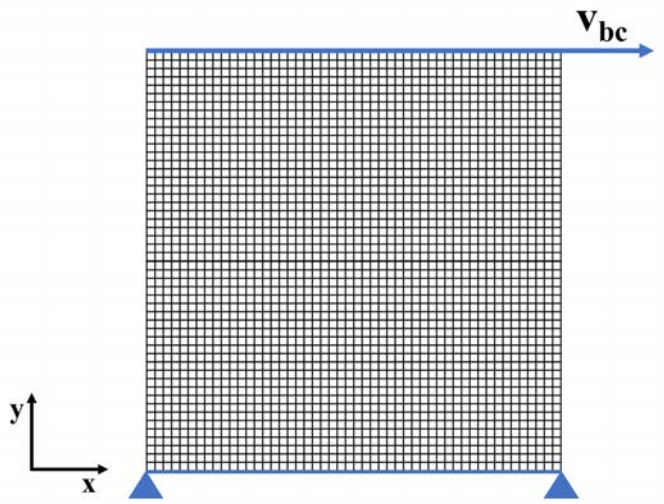

Figure 4.3.1: Finite element generalised plane strain model; 50 elements by 50 elements, and the applied boundary conditions from ABAQUS

The loading conditions applied to the domain are depicted in Figure 4.3.1, the bottom face of the domain was pinned in place and the top face of the domain was assigned a velocity in the x-direction. The constant velocity on the boundary provided a strain controlled loading scenario. The velocity of the top set of nodes provided a shear strain rate $100s^{-1}$ used throughout the simulations. Periodic boundary conditions were imposed on the edges of the finite element domain. No transmission of slip is allowed on the left and right hand side boundaries. The UMAT sets the material parameters like the stiffness matrix and performs the deformation kinematic calculations. It uses the dislocation shear from the previous dislocation distribution to update the stress of the domain which feeds into the user defined subroutine (URDFIL) to access results files during the simulations. The subroutine URDFIL contains the FDM code for the dislocation evolution and is used to access and update the results stored in the COMMON blocks whilst the finite element analysis is running. As already stated, the UMAT updates the stresses based on dislocation slip kinematics: determine plastic shear rates, calculate plastic velocity gradient; calculate Green-Langrange strain tensor; update stress. The updated stress and dislocation field are then passed to the URDFIL subroutine, where the FDM code is called for the new time step. The following list

details the order in which the FDM model performs calculations during a simulation:

1. Define the material constants, microstructure (the distribution of γ' particles and grain boundary) and orientation of slip system.

2. ABAQUS deforms the domain according to the loading conditions set and calculates the deformation gradient which is passed to the UMAT.

3. The UMAT has the key parameters and defines the constitutive behaviour of the material provided by the deformation kinematics equations. Using the most recent dislocation field shear rates from the FDM and deformation gradient from ABAQUS to calculate the new stress field.

4. The URDFIL is called at the end of the each step where it performs the FDM calculations using the applied stress field from the UMAT updating the dislocation positions and recording the shear rates.

5. Return to step 2.

4.4 γ/γ' dispersions

In this work, γ' dispersions representative of fine grain (FG) RR1000 have been adopted. The microstructures characterised by Schulz et al. [85] and Anderson et al. [14] have been used to generate precipitate dispersions in this work. Figure 4.4.1 shows precipitate dispersion after 50 hours thermal exposure at 700°C, 750°C and 800°C. Summary of the dispersion parameters for these microstructures are listed in Table 4.1. The model set-up described in the previous section, does not allow resolution of the tertiary γ' particles and these will not be explicitly modelled in this work. Instead they will be accounted for through a line tension approximation (Chapter 3). Based on some experimental characterisation of RR1000 [14,85], the secondary γ' particles of a mean radius of 100nm is assumed to be representative.

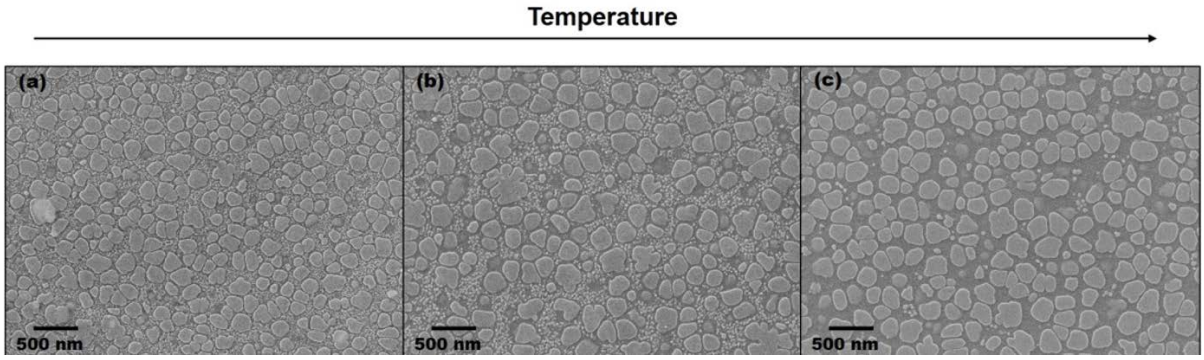

Figure 4.4.1: SEM images of RR1000 taken at temperatures; (a) 700°C, (b) 750°C, (c) 800°C. [14]

Table 4.1: Microstructure parameters for the temperature distributions

Temperature °C	R_s, nm	Φ_s, %	R_t, nm	Φ_t, %
700	100	35	10	8
750	100	33	20	5
800	100	30	0	0

To create the particle fields a MATLAB code was created to randomly distribute the particles within the mesh. Using the data in Table 4.1 particle distributions were created for the three temperatures. Three distributions were generated at each temperature, as seen in Figure 4.4.2, to compare how the heterogeneous secondary γ' particle distributions influence the flow stress at each temperature. The black squares indicate the presence of a γ' particle, when the dislocation density is at the point to the side of a particle it must overcome the critical shear stress to move through the particle. The spacing of the particles allowed a minimum distance between them to prevent overlap and to stop the faces of particles touching, creating larger particles. The code allowed the particle radius and volume fraction to be varied, using the square particles to fit the grid using the resolution of the spacing dx.

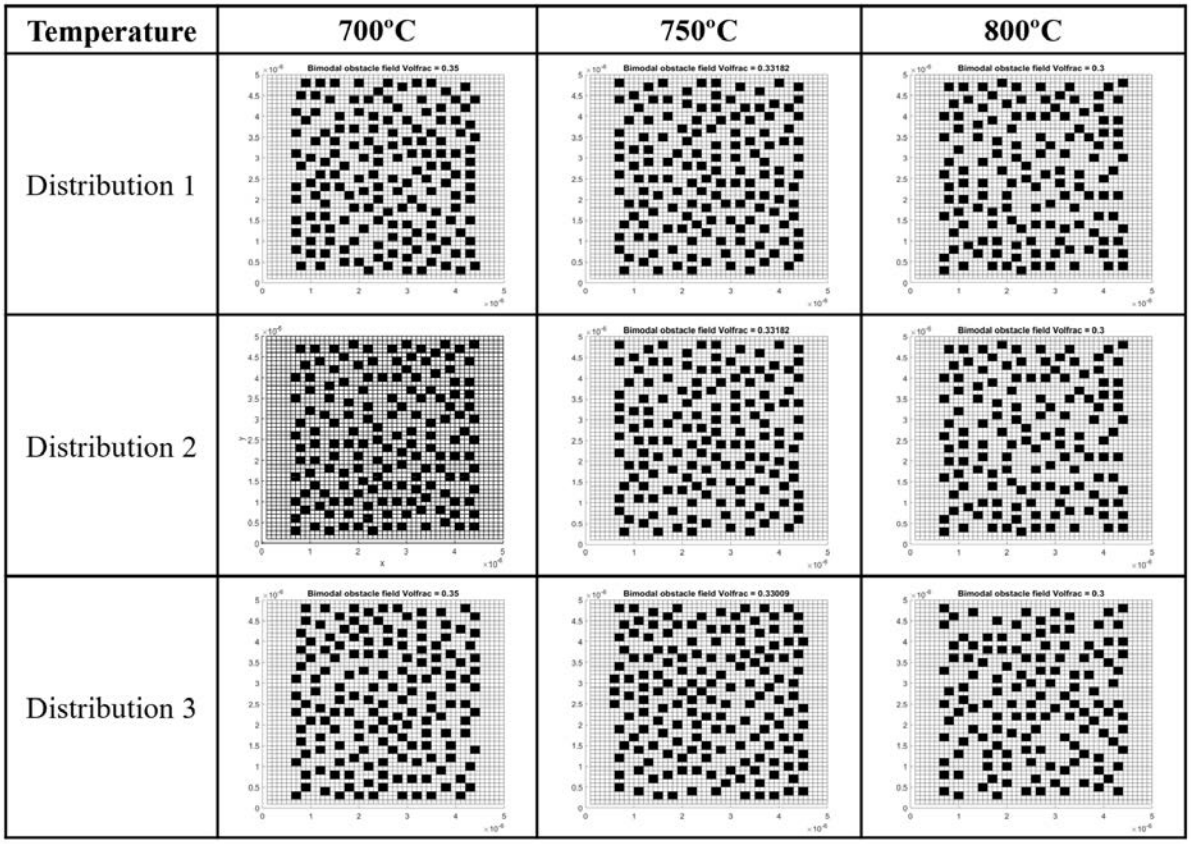

Figure 4.4.2: Particle distributions created for values provided in Table 4.1

The velocity of dislocations follow a velocity profile as they travel through the γ matrix and γ' particles. They initially follow the jog mobility profile and once this requires more energy it swaps to the linear drag mobility profile. The transition between the profiles is demonstrated in Figure 3.4.1. The velocity of the dislocations is capped however. The maximum velocity of the dislocations was limited to the speed of sound in relevant medium for γ matrix or γ' precipitate. The speed of sound calculated by

$$v_{sound} = \sqrt{\frac{\mu}{\varrho}} \tag{4.4.1}$$

The mobility term, M, for dislocations differs between the γ and γ' due to the difference in density and shear modulus and how it changes the speed of sound in the mediums. As

already stated the shear condition has to be met before the dislocations shear the particles. Several assumptions have been made to facilitate the calculations. Firstly the calculations assume that the dislocation stress field contributions are not significantly modified by the γ/γ' interfaces and grain boundaries, so that the homogeneous dislocation stress solutions can be used. Secondly, isotropic elastic solutions for the dislocation stress field are assumed. This approximation is reasonable when dealing with two-dimensional problems.

4.5 Model parameters

The key parameters and material constants found in the FDM theory presented in Chapter 3 are presented in Table 4.2. The values used are based on literature for Nickel-based superalloys to obtain accurate dislocation mechanics which produce similar stress-strain properties as observed experimentally. Constants that can be obtained using the equations have been used to make sure they are physically correct relative to the other parameters used. The temperature dependent constants shown in Table 4.2 are calculated at a temperature of $973K$.

Table 4.2: Material constants and key model parameters

Parameter	Value	Reference
Burgers vector, b (m)	2.54×10^{-10}	-
Material density γ, ϱ_γ (gcm^{-3})	7.98	[86]
Material density γ', ϱ_p (gcm^{-3})	7.50	[87]
Shear modulus in γ, μ_γ (GPa)	5.39	[86]
Shear modulus in γ', μ_p (GPa)	5.23	[87]
Mobility in γ, M_γ $(Pa^{-1}s)$	6795	Equation (3.4.2)
Mobility in γ', M_p $(Pa^{-1}s)$	6904	Equation (3.4.2)
Velocity of sound, v_{sound} (ms^{-1})	3.624×10^3	Equation (4.4.1)
Poisson's ratio, ν	0.333	[88]
Line energy, Γ	3.28×10^{-9}	$0.5\mu_\gamma b^2$
Boltzmann constant, k $(m^2kgs^{-2}K^{-1})$	1.3806×10^{-23}	-
Atomic volume, a_v (m^3)	8.18×10^{-30}	-
Atomic self-diffusivity, D_{s0} (m^2s^{-1})	2.0×10^{-4}	-
Jog spacing, λ_{jog} (m)	$300b$	[89]
Jog height, h_{jog} (m)	2.07×10^{-10}	$\frac{\sqrt{2}}{\sqrt{3}}b$
Climb activation energy, Q (kJ)	310	-

The stiffness tensor, $\underset{\equiv\equiv}{\boldsymbol{C}}$, is the gradient of the change in stress divided by the change in strain, this differs depending on the mediums through which the dislocations propagate, for example γ matrix or γ' particles have different $\underset{\equiv\equiv}{\boldsymbol{C}}$ component values. In the calculations the stiffness tensor components, also known as the elastic constants, are described by a six by six matrix

$$\underset{\equiv\equiv}{\boldsymbol{C}} = \begin{pmatrix} C_{11} & C_{12} & C_{12} & 0 & 0 & 0 \\ C_{12} & C_{11} & C_{12} & 0 & 0 & 0 \\ C_{12} & C_{12} & C_{11} & 0 & 0 & 0 \\ 0 & 0 & 0 & C_{44} & 0 & 0 \\ 0 & 0 & 0 & 0 & C_{44} & 0 \\ 0 & 0 & 0 & 0 & 0 & C_{44} \end{pmatrix} \tag{4.5.1}$$

The stiffness matrix values are temperature dependent and required functions to change the values according to the different temperature microstructures. The values in the γ matrix are taken from elastic component and temperature data by Mossa [86]. Fitting the data to obtain following temperature dependant relations for the elastic constant components

$$C_{11} = \left((-2 \times 10^{-5})T^2 - (0.0189)T + 241.16\right) \times 10^9 \tag{4.5.2}$$

$$C_{12} = C_{11} - 2\left((-0.0092)T + 49.33\right) \times 10^9 \tag{4.5.3}$$

$$C_{44} = \left((-1 \times 10^{-5})T^2 - (0.0153)T + 129.17\right) \times 10^9 \tag{4.5.4}$$

The relationship between temperature on the elastic components of the γ' particles was characterised from Ni_3Al data by Prikhodko [87]. The C_{11}, C_{12} and C_{44} values for the γ' particles are given by

$$C_{11} = \left((-1 \times 10^{-5})T^2 - (0.0174)T + 235.21\right) \times 10^9 \tag{4.5.5}$$

$$C_{12} = \left((-1 \times 10^{-5})T^2 - (0.0053)T + 153.12\right) \times 10^9 \tag{4.5.6}$$

$$C_{44} = \left((-4 \times 10^{-6})T^2 - (0.0254)T + 131.64\right) \times 10^9 \tag{4.5.7}$$

Chapter 5

Validity of the field dislocation mechanics through discrete dislocation dynamics

5.1 Introduction

Before implementing the FDM theory the transition from the discrete to the continuum had to be considered, and how discrete interactions would be accounted for. The dislocation density evolved by the theory represents a number of dislocations in an area, the length scale of this area needs to be calculated. The number and configuration of dislocations within the dislocation density will change how it interacts with other densities. Discrete dislocation dynamics (DDD) was used to determine key features of the FDM model. An in-house DDD code was used simulate different dislocation scenarios providing information used to inform the FDM model.

In order to implement the evolution of the dislocation field a suitable length scale was determined for the continuum description of dislocations. The continuum approach is designed

to capture the behaviour of large numbers of dislocations over length scales defining grains which would be computationally expensive with discrete dislocation simulations. Small scale discrete dislocation simulations were used to find where discrete interactions match continuum descriptions to find the length scale where the FDM approach, described in Chapter 3, is valid. The in-house DDD code was used to draw a comparison of the dislocation density distribution between discrete pile-up of dislocations to those of analytical solutions for continuum dislocations [2].

Following this the DDD model was used to investigate other discrete behaviour and how it would translate to the continuum scale. Firstly discrete dislocation simulations were used to determine an annihilation rate for interacting positive and negative dislocation densities. Secondly the variation in the stress field due to dislocation configuration within the density was investigated and if the super-dislocation stress field approximation is suitable as the scale. This involved comparing stress fields of different discrete dislocation configurations within the area of the dislocation density and how they differ relative to distance from the configuration.

Using the minimum length scale determined for the continuum of dislocations description, initial simulations for the FDM model were performed to examine the physical behaviour for a single slip plane. The model was tested for stability of the solutions from the finite difference approximations and limitations of scale. Analytical continuum pile-up solutions were used to validate FDM model in replicating the continuum pile-up of dislocations. Followed by some initial FDM simulations for multiple parallel slip systems.

5.2 Discrete dislocation dynamics model

An in-house model for discrete dislocations dynamics (DDD) was created to simulate the motion of parallel edge dislocations. The DDD model implemented the physical equations for dislocation glide, driven by stress field contributions from an external stress and the internal stress fields created by the lattice distortion created by the dislocations. Dislocations were confined to a single slip system able to move parallel to on another. For slip to be achieved in the model the dislocation must overcome certain aspects of the material that impinge dislocation motion. To move throughout the lattice dislocations must overcome an energy barrier known as the Peierls force. This energy is formed from the configurational changes that are formed when an edge dislocation; with the half plane of atoms moving from a stable symmetrical configuration to an unstable unsymmetrical configuration and back to a symmetric configuration. Nabarro [17] gives the derivation of the maximum Peierls force to be:

$$F_{peierls} = \frac{2b\mu}{1-\nu} \sin 2\pi \exp\left(-\frac{4\pi \frac{2\pi 1-\nu}{b}}{b}\right) \tag{5.2.1}$$

If the force is large enough to overcome the Peierls barrier the moving dislocation also has a drag that will impinge its movement. The force acting on each dislocation was calculated by summing the contributions due to the internal stress fields of all the other dislocations within the domain and the micro-stress field from the externally applied load. For the two dimensional system considered, using $\underline{\boldsymbol{b}} = [b\,0\,0]$ and $\underline{\boldsymbol{t}} = [0\,0\,1]$ for edge dislocations resulted in the internal dislocation stress field components driving motion being described by

$$g_{12}(\underline{\boldsymbol{x}} - \underline{\boldsymbol{\xi}}) = \frac{(x-x')((x-x')^2 - (y-y')^2)}{((x-x')^2 + (y-y')^2)^2} \tag{5.2.2}$$

acting in the slip direction. Dislocations were confined to move on the slip plane they generate on, for the results generated the force components acting normal to the slip plane do not influence motion. This g_{12} component is the same stress field component used in the FDM

calculations.

The model tracks the positions of each dislocation in the simulation. The Peach-Koehler force felt on the dislocation, given by Equation (3.2.21), was calculated from the stress for each dislocation position. Then using the equation for drag controlled glide, $\underline{\boldsymbol{v}}(\underline{\boldsymbol{x}}, t) = M\underline{\boldsymbol{f}}(\underline{\boldsymbol{x}}, t)\cdot\underline{\boldsymbol{s}}$, the glide velocity of each dislocation in the slip direction was calculated.

The velocity of each dislocation was multiplied by the time step to work out the displacement of each dislocation and update their position for the next time step. In dislocation dynamics the time step is very important in capturing the dislocation behaviour, Deshpande et al. [90] examined the effect of different time steps on getting the right dislocation reactions. If the time step is too large intricacies in dislocation behaviour are removed and too small the simulation becomes inefficient and time consuming. In assessing different time steps with discrete integration to capture the chaotic nature of dislocations a time step of 5×10^{-11}s was found to be sufficient.

The domain in which the dislocations moved was assumed to be a continuous γ matrix, with material parameters based on those of Nickel-superalloys. There are no particle interaction terms used in the DDD model. Boundary conditions could be changed for the simulation purpose so dislocations stop at the boundary (used in the dislocation pile-up analysis) or periodic boundary conditions (used in annihilation and analysis and stress fluctuation analysis). Utilising the stress driven dislocation generation equation (2.2.1) allowed for an accurate recreation the dislocation pile-up distributions. The nucleation length, L_{nuc}, was approximated at $100\underline{\boldsymbol{b}}$ taken from literature [91] and nucleation stress calculated by rearranging Equation (2.2.1). Dislocations adopted equilibrium positions which would exert a back stress on the source to prevent further dislocation generation. This allowed the stress dependency to dictate the number of dislocations generated in each equilibrium pile-up

scenario.

5.3 The scale of the continuum, an investigation through discrete dislocation pileup

As already stated, the applicability of any field dislocation mechanics theory requires determination of the length scale above which such an approach can be used. Continuum simulations in domains smaller than this length scale individual dislocations may be resolved. In the latter case continuum descriptions of the transport of dislocation do not apply. The transition from the discrete to the continuum description has been determined through numerical analysis of DDD simulations. Equations (2.2.3), (2.2.4) and (2.2.5) are used to determine the transition from the discrete to the continuum length scale. Although the model was built for parallel dislocations two-dimensional cross section of a grain, the pile-up simulated in the present research only required dislocations on a single slip plane. The two dimensional functionality was used to investigate other discrete behaviour for the continuum.

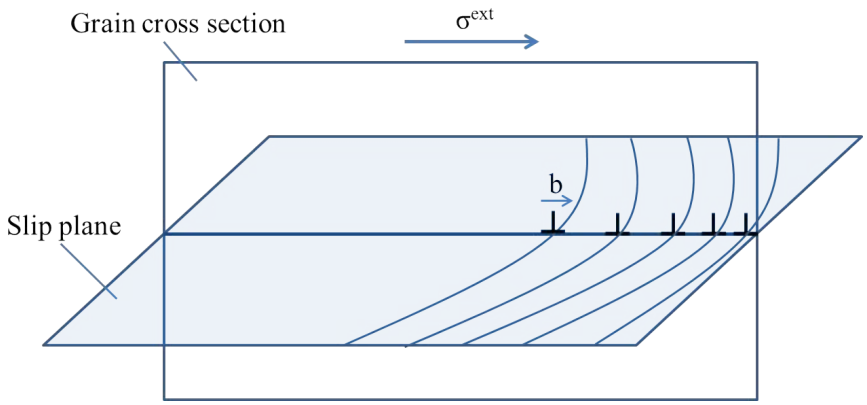

Figure 5.3.1: Cross section represents the area modelled using the DDD code. Edge dislocations moving along the slip plane parallel to the Burgers vector.

The DDD model for edge dislocations described in section 5.2 was run to observe numerical

dislocation pile-ups. It models dislocation motion on a single slip plane as if a cross section of the dislocation line as shown in Figure 5.3.1. The DDD simulations had a Frank-Read (FR) source in the centre of the slip plane generating dislocations, these were stopped at the domain boundaries causing pile-up. This continued until the back stress acting on the source prevented further generation and the dislocations fell into their equilibrium positions, an example of dislocations in equilibrium positions is seen in Figure 5.3.2.

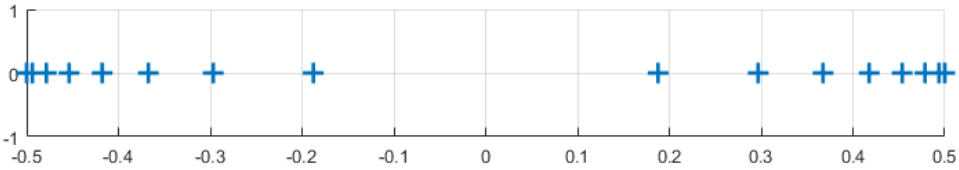

Figure 5.3.2: Example of dislocation positions in equilibrium pile-up for a short domain of 600 nm

Figure 5.3.3 gives a history of the total number of dislocations generated within the domain for a simulation. Once the total number of dislocations stopped increasing it was assumed that the system was in equilibrium and the back-stress exerted from the dislocations on the source lowered the stress sufficiently to prevent further dislocation generation. Then the line density of dislocations was calculated across the slip plane depending on dislocation sign, see Figure 5.3.4. The scaled line density values below zero indicate the distribution of the negative dislocations.

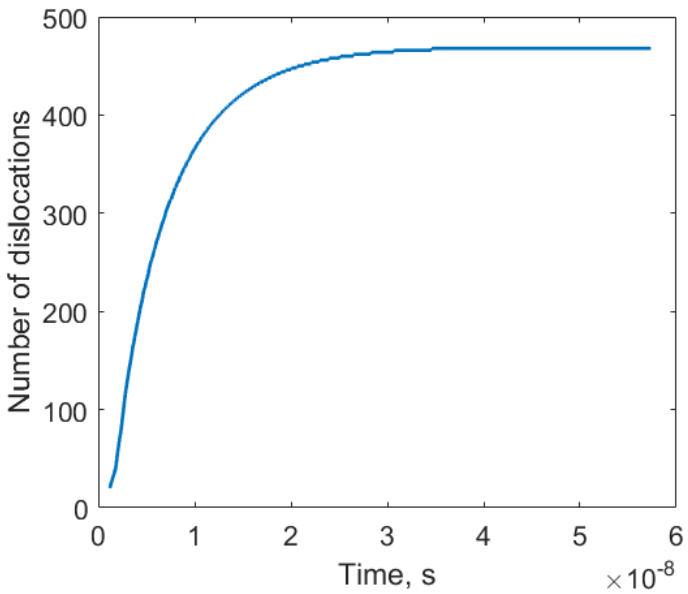

Figure 5.3.3: Example of dislocation generation with time in DDD simulation over a 6 μm domain

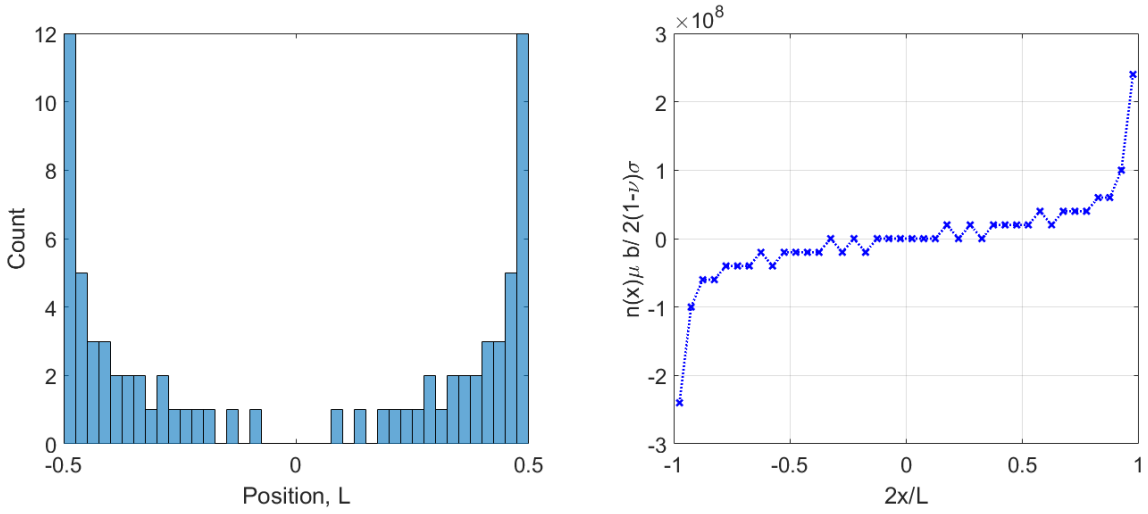

(a) Histogram of dislocation count in segments along slip plane

(b) Scaled line density plot of dislocations by sign

Figure 5.3.4: Histogram of dislocation count and corresponding line density plot for a 2 μm domain

The pile-up positions observed from the DDD accurately matched the dislocation pile-up equilibrium positions from the literature [18] across multiple length scales and numbers of

dislocations. The dislocation line density was calculated by dividing the domain into equally sized divisions and counting the number of dislocations in each. The density of line segments were plotted against the normalised plot of (2.2.5), see Figure 5.3.5. The applied stress had a big influence on the number of dislocations generated. Large stresses were needed to provide enough dislocations to use a continuum representation. For example the simulation under 266 MPa stress produced 50 dislocations and at 533 MPa produced 102 dislocations. The extra dislocations produced provided a much better count to the analytical continuum pile-up curve as shown in Figure 5.3.5.

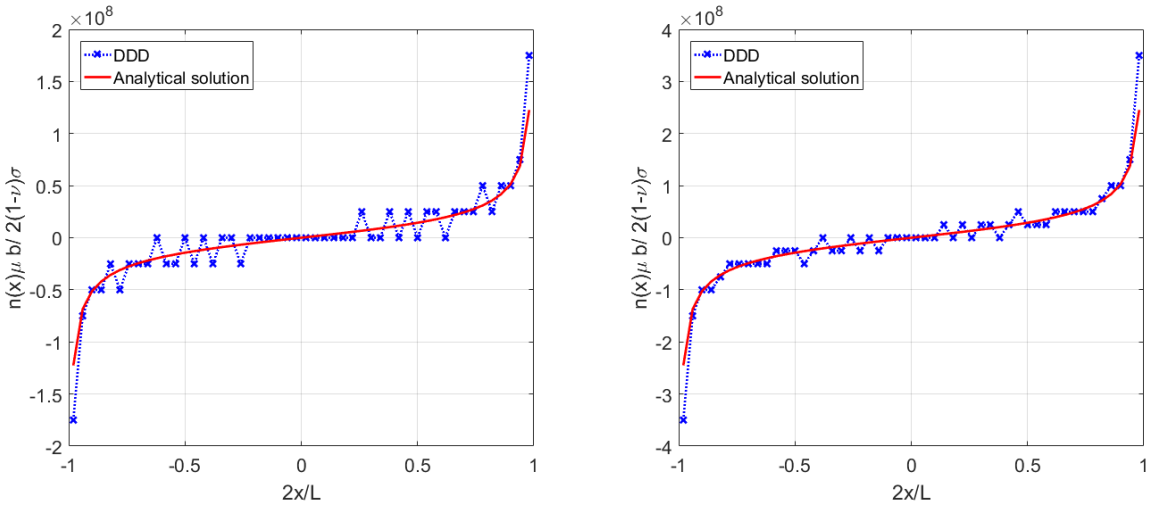

(a) Pile-up in DDD at 266 MPa (b) Pile-up in DDD at 533 MPa

Figure 5.3.5: Comparison of DDD pile-up for the same 2μm domain at different applied stress

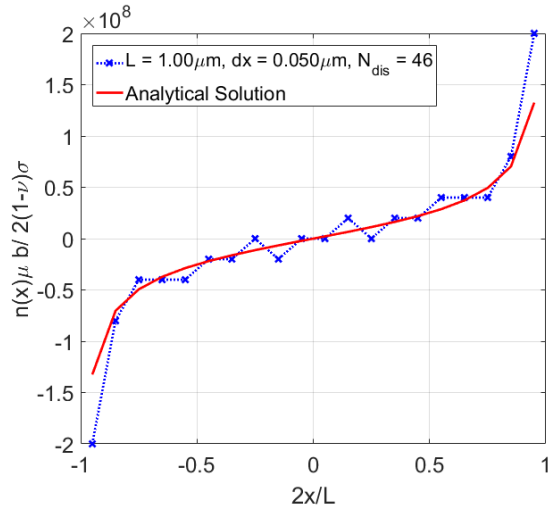

(a) $L = 1\,\mu$m slip plane

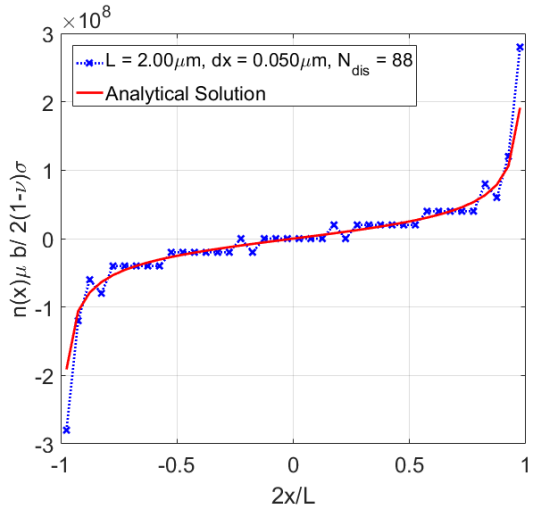

(b) $L = 2\,\mu$m slip plane

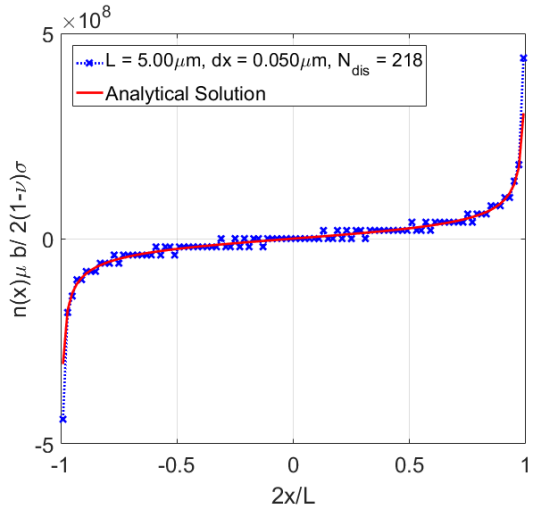

(c) $L = 5\,\mu$m slip plane

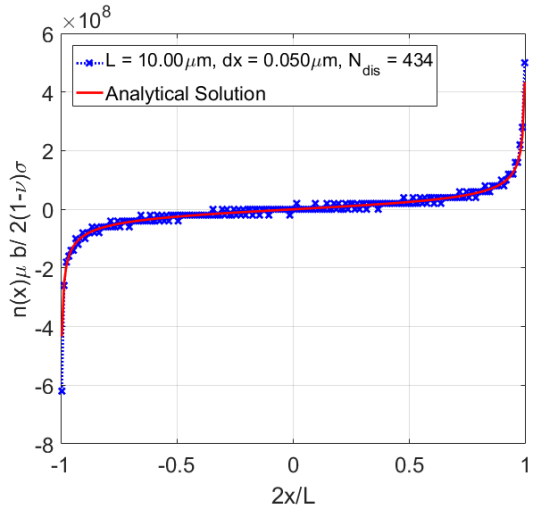

(d) $L = 10\,\mu$m slip plane

Figure 5.3.6: Double ended pile-up of edge dislocations in the DDD model for multiple length scales all using $dx = 50$ nm to count the line density.

Using the same division width of $dx = 50$ nm the continuum pile-up matched well with the DDD line density over multiple length scales. Normalised axes are used in Figure 5.3.6 to directly compare the profiles of the different plots and their deviation from the analytical pile-up plot of Equation (2.2.5). The average absolute residuals between the simulated and analytical data get smaller with increased domain size. The domain length determined how many dislocations could be produced until the back stress on the source was great enough

to prevent further dislocation production at the FR source. Shorter domains producing less dislocations as the dislocations are closer to the source and given the $1/x$ nature of the stress fields put a lot more stress on the FR source than the larger domains, thus require less dislocations to create a back stress which prevents generation.

5.3.1 Continuum break-down

The continuum description must have a minimum length scale which it is an effective description of grouped dislocation behaviour, from this distance and above it can be used to take over from discrete calculations. Simulations were run for decreasing length scales, maintaining the 50 nm grid division size, until the discrete dislocation distribution did not match the analytical pile-up plot, see Figure 5.3.7. For domain lengths of 800 nm and less the pile-up breaks down due to the small number of dislocations generated within that space are not enough to represent as a continuum density. The 50 nm divisions could not form a symmetrical distribution. Figure 5.3.7a shows a loose fit to the continuum over 900 nm, this DDD simulation generated a distribution of only 24 dislocations produced under an applied stress of 266 MPa, with the maximum count of 6 dislocations using $dx = 50$ nm. More dislocations can be generated within these small domain lengths giving a more continuum-like dislocation distribution, but only at very high stresses in excess of 800 MPa.

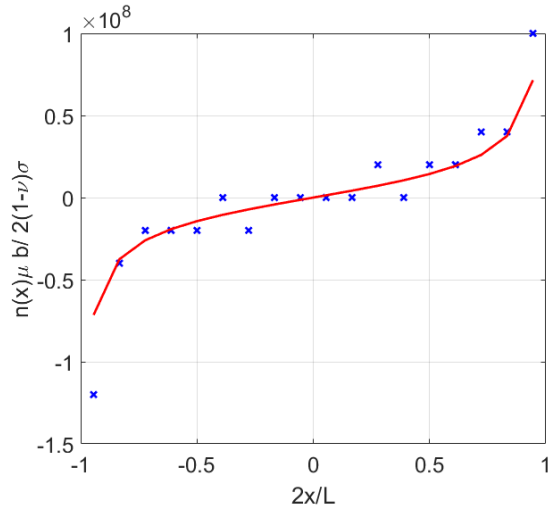

(a) $L = 900$ nm, $dx = 50$ nm

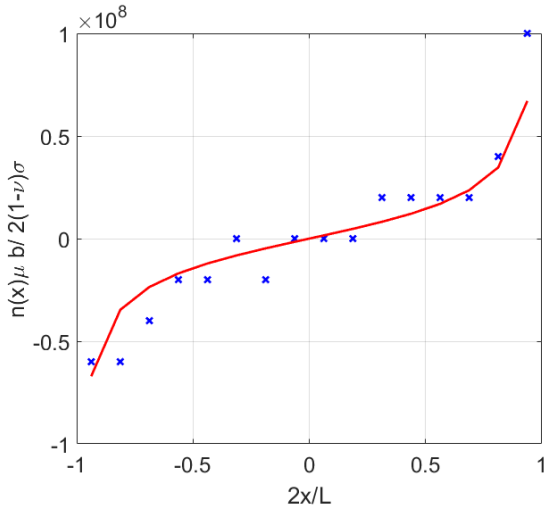

(b) $L = 800$ nm, $dx = 50$ nm

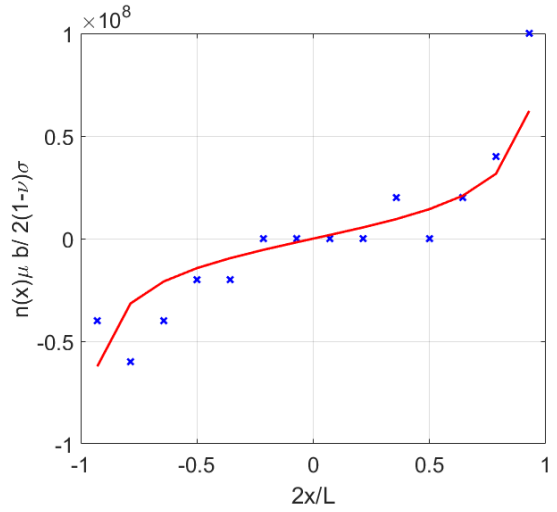

(c) $L = 700$ nm, $dx = 50$ nm

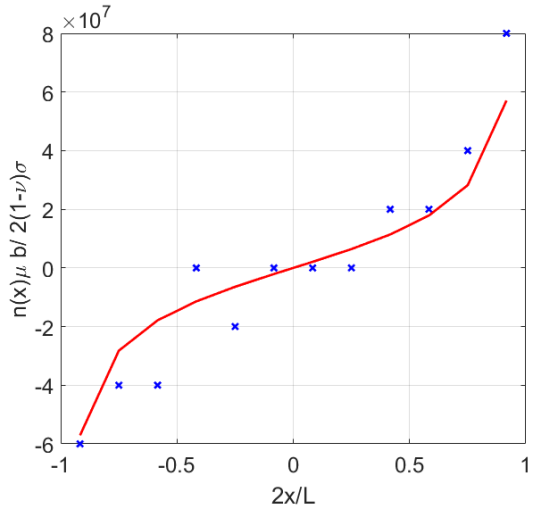

(d) $L = 600$ nm, $dx = 50$ nm

Figure 5.3.7: Break down of double ended pile-up in the DDD model at small length scales

5.3.2 Numerical considerations for FDM pile-ups

The fit of the dislocation line density to the analytical solution can vary greatly depending the grid division size, dx, used in the finite difference scheme to solve the dislocation transport equation. Less dislocations are generated within smaller computational domains, L, the low number of dislocations makes it less suitable to describe as a continuum. The benefit of the continuum theory is to capture large numbers of dislocations that would be very

computationally expensive to simulate with a discrete model. The representative area of the dislocation density has to be large enough to capture multiple dislocations whilst maintaining a good resolution to capture smaller scale grouped dislocation behaviour. Changing the grid division size had an influence on the line density value and fit to analytical solutions, shown in Figure 5.3.8.

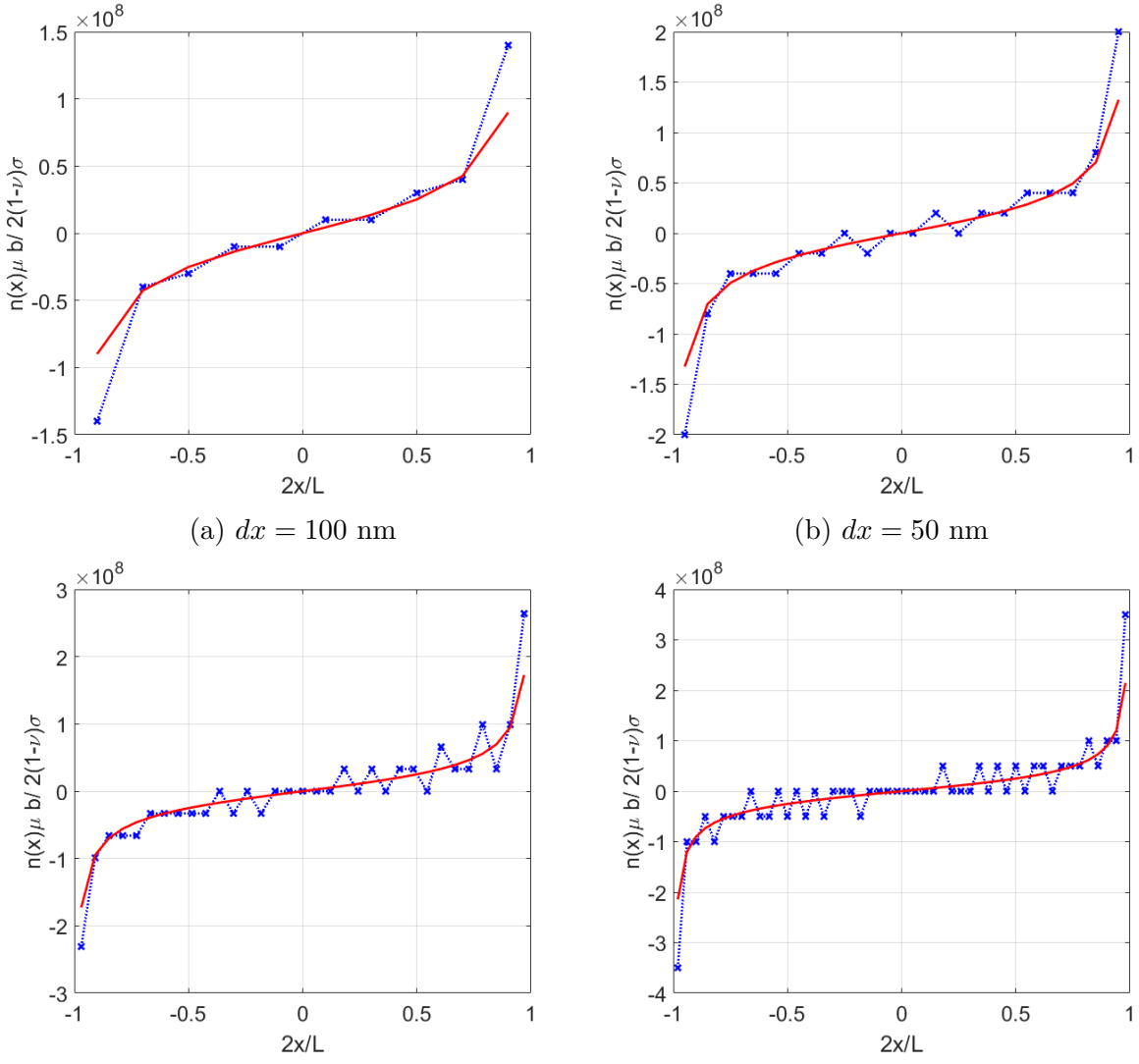

(a) $dx = 100$ nm

(b) $dx = 50$ nm

(c) $dx = 30$ nm

(d) $dx = 20$ nm

Figure 5.3.8: Comparison of continuum pile-up count from the DDD model for $L = 1\,\mu$m with different division sizes, dx, for the line density

From Figure 5.3.8 divisions less than 50 nm do not fit well to the analytical pile-up solutions,

the divisions often not counting any dislocations. Division sizes $dx = 50$ nm and $dx = 100$ nm had the smallest residuals from the analytical solution. For simulating large computational domains the same minimum grid spacing for the finite differencing scheme can be used. However, it was found that larger grid divisions can be used and still match well to the analytical continuum description. Figure 5.3.9b displays line density of dislocation pile-up for $dx = 100$ nm and $dx = 200$ nm both tracking very closely to the analytical solution in a larger domain of $L = 10\,\mu$m. When simulating large domains maintaining a small division size increases the number of points and thus the computational cost, therefore it is beneficial to change the dx relative to the domain length to reduce calculations.

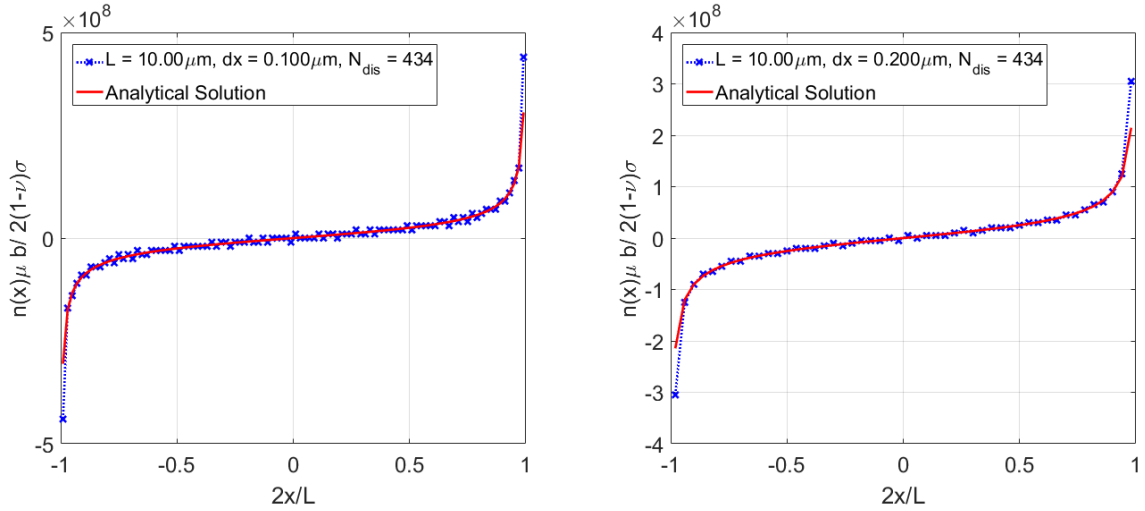

(a) $dx = 100$ nm (b) $dx = 200$ nm

Figure 5.3.9: Comparison of continuum pile-up count from the DDD model for $L = 10\mu$m with different division sizes.

5.4 Characterising dislocation interactions

Using the DDD to inform the FDM model. Looking for the scale of the dislocation density the rate of annihilation events for interacting densities. Then examining the combined dislocation stress fields and how they would influence surrounds dislocations relative to the dislocation density stress field approximation.

5.4.1 Dislocation annihilation rate

In order to form dislocation structures both positive and negative dislocations are required, features like dipole formation are integral to forming slip bands. When positive and negative dislocations approach within a specific distance of one another they annihilate restoring the crystal lattice. The dislocation stress field is comprised of the compressive and tensile fields created by the extra half plane in the crystal lattice, this contributes to the potential energy in the material. When two dislocations of opposite orientation approach within a critical distance (of approximately $6\underline{\boldsymbol{b}}$) they annihilate and the stored energy is removed as their stress fields cancel out. Annihilation of dislocations removes some of the dislocations reducing shear rates and the amount of plastic strain. To capture this behaviour an annihilation rate was introduced into the FDM model for the scenario where positive and negative dislocation densities meet, influencing the dislocation flux.

The rate at which annihilation occurs in our continuum model can be calculated through a stochastic approach. Averaging annihilation events at the smaller discrete scale to create a description on the larger continuum scale. In the continuum model annihilation events have to be described as a likeliness or rate of annihilation when densities of opposite sign dislocations meet as only a proportion of the dislocations may actually pass in a range resulting in annihilation which will vary with the configuration and number of interacting dislocations. Suppose a number of positive dislocations, N^+, and negative dislocations, N^-, within a domain and over a time period, dt, a number of positive and negative dislocations annihilate, $a = a^+ = a^-$.

$$N^+(t + dt) = N^+(t) - a \tag{5.4.1}$$

$$\dot{a} = \lim_{dt \to 0} dt^{-1} \left[N^+(t + dt) - N^+(t) \right] \tag{5.4.2}$$

$$a = N^+ P[+|-] \tag{5.4.3}$$

Equation (5.4.3) contains the term $P[+|-]$ which is the probability of annihilation between positive and negative dislocations. This probability will scale as a function of N^{-1} assuming a discrete measure for it,

$$P[+|-] \propto N^{-} \tag{5.4.4}$$

$$\dot{a} \propto N^{+}N^{-} \tag{5.4.5}$$

$$\dot{A}(x) \propto \rho^{+}(x)\rho^{-}(x) \tag{5.4.6}$$

The rate of dislocation annihilation was described as a function of the the product of the positive and negative dislocation density, see Equation (5.4.6). This annihilation rate function was characterised by running repeated DDD simulations with initially randomly positioned dislocations. Tracking the rate of annihilation and total annihilation events that occurred. This was tested for different numbers of positive and negative dislocations.

For an initial number of dislocations in a domain without sources experienced the same amount of annihilation plus or minus a couple of dislocation pairs occurred. With sources there was a steady rate of annihilation. Results shown incorporate sources into the DDD simulation domain. Initial randomly distributed sets of dislocations were created for different initial numbers of dislocations within a square domain of length 100 nm. For each initial dislocation number 500 simulations were run to average the number of annihilation events that occurred within a time frame, see Figure 5.4.1, for a range of dislocation densities.

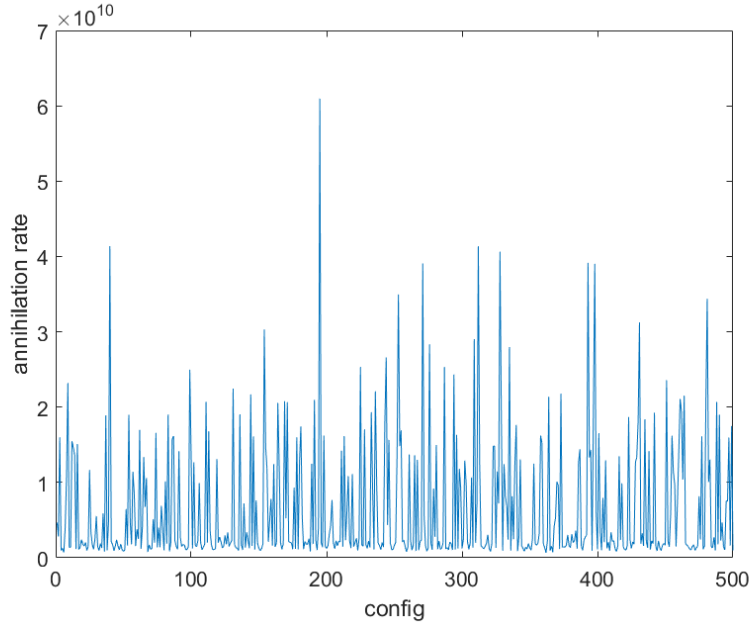

Figure 5.4.1: Average annihilation rate for each simulation

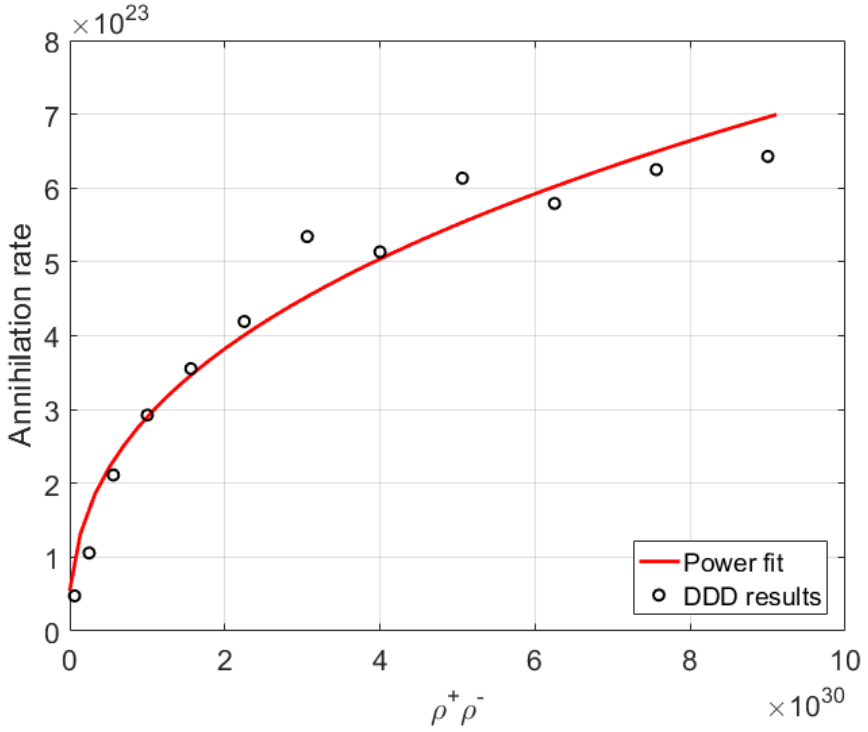

Figure 5.4.2: Relationship between density and annihilation rate with a power fit

A power relation between the product of the dislocation densities and the annihilation rate fits the data in Figure 5.4.2, the equation of the fit is given by

$$\dot{A}^{-}(\boldsymbol{x},t) = P^{p}_{ann}(\rho^{+}(\boldsymbol{x},t)\rho^{-}(\boldsymbol{x},t))^{0.3984} \tag{5.4.7}$$

where $P^{p}_{ann} = 3.24\times10^{11}$ is a fitting coefficient. The annihilation rate function was multiplied by the time step to calculate the magnitude of density annihilated, half of which was removed from both positive and negative dislocation densities.

5.4.2 Stress field fluctuations of the dislocation density configuration

This section focuses on validating the assumption that the stress field of a continuous field of dislocations can be approximated as that of a super-dislocation having a Burgers vector given by the dislocation density tensor. It was anticipated that this will be a good approximation at large distances but near the group of dislocations self interactions will induce fluctuation. The aim of this section is to assess the magnitude of such fluctuations on the stress field.

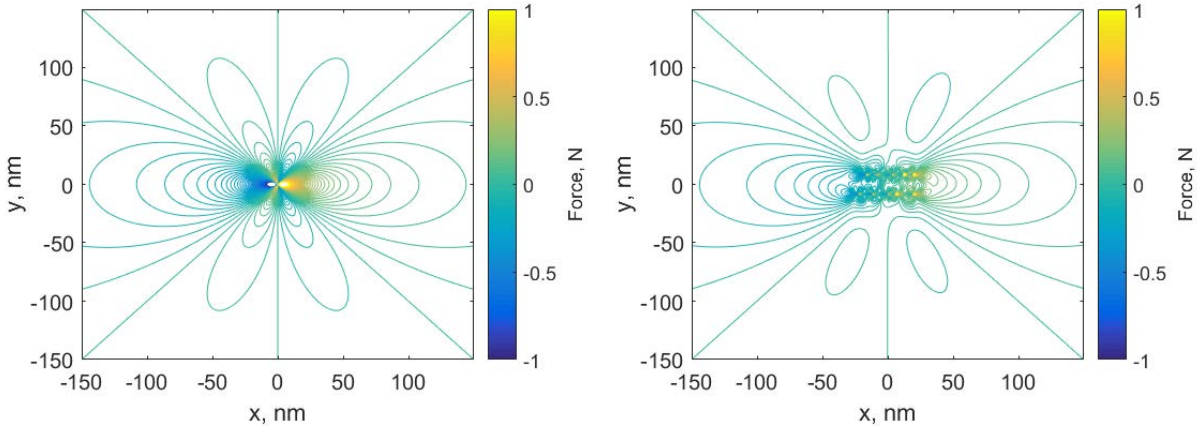

(a) 'super dislocation', $b_{tot} = 10\boldsymbol{b}$

(b) dislocation configuration, 10 dislocations, 2 slip planes with 5 each

Figure 5.4.3: Force field contours calculated from the g_{12} stress component between a configuration of dislocations and the equivalent 'super-dislocation'

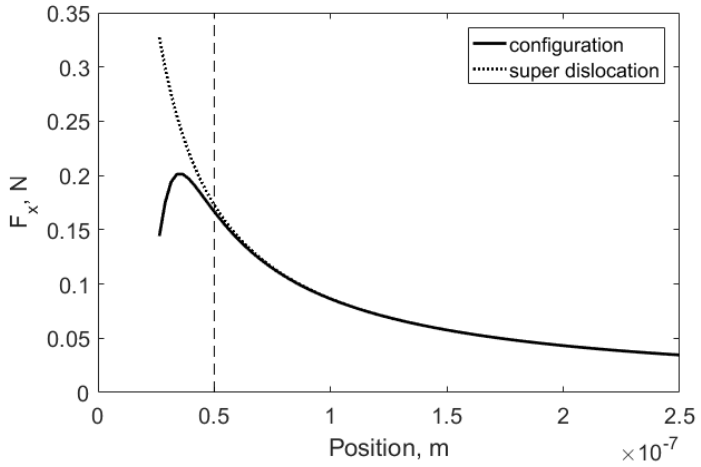

Figure 5.4.4: Comparison of the force field component, F_x, of the configuration and 'super-dislocation' acting on the slip pane central to the configuration

Figure 5.4.3 shows a contour plot of the g_{12} field for a single dislocation of Burgers vector $10\underline{\boldsymbol{b}}$ and a cluster of 10 dislocations each with Burgers vector $\underline{\boldsymbol{b}}$. As expected the g_{xy} field in the vicinity of the cluster of dislocations can be seen to be perturbed compared to the single dislocation case. Figure 5.4.4 shows the variation of the x-component of the force acting along the central slip plane of the density, $y = 0$, between the discrete configuration and 'super-dislocation', they converge to each other within 100 nm. Large differences in stress are only seen within the density area which the dislocations are positioned, inside the representative density area. Given the length scale of present simulations the stress at a point far away from the dislocation cluster is well approximated by the 'super-dislocation'. The local fluctuations at a dislocations density point were investigated using a stochastic approach during further developed FDM model in Chapter 6.

5.5 Initial FDM simulations

The governing equations for transport of the dislocation field described in Chapter 3 were validated by setting up FDM simulations to produce dislocation density pile-ups along a sin-

gle slip plane for a purely γ-matrix as used in the DDD model. The pile-ups were validated using the same method as the DDD simulations reported in Section 5.3 comparing to the analytical solutions given by Equation (2.2.4) and Equation (2.2.5). An existing continuum dislocation dynamics model has performed a similar validation for their model, where an initial dislocation density distribution is advected to form the pile-ups [79]. The numerical implementation presented in Chapter 4 was used to solve the advection equation (3.2.18). These simulations only involved the Fortran calculations for the FDM model using a constant applied stress and were not integrated with ABAQUS to update the stress state. To adapt dislocation generation for the continuum the Frank-Read mechanism, described by Equation (2.2.1), was scaled to the continuum. The nucleation length was smaller than the resolution of the representative continuum area. Assuming the density contained one dislocation nucleation source that generated at sufficient stress defined by the nucleation length. Using the nucleation time for source the amount of density generated was scaled with the timestep.

First single pile-up was simulated for a same sign dislocation field, followed by double pile-up for both positive and negative dislocation fields. The length scales and division sizes determined for the continuum dislocation field in section 5.3 were used in the FDM simulations, using domain length scales of $L = 2\,\mu$m and above, and grid spacings of $dx = 50$ nm. Smaller division sizes were tested for comparison of stability. The numerical implementation of the FDM was then expanded to two-dimensions.

The pile-up of dislocations leads to a steep gradient of the density function which can become unstable. The implicit Gauss-Seidel method described in Chapter 4 was used to solve the partial differential equation (3.2.18). Figure 5.5.1 shows comparison of the simulated FDM pile-up to the normalised plot of (2.2.4). The profiles show that same implicit finite difference scheme with a different numerical derivative approximations can become unstable

at the boundary. At higher stresses and increased dislocation density mobility, the two-point gradient approximation calculation (4.1.2) collapsed at the boundary. The three-point approximation (4.1.4) remained stable and accurately matched the analytical solution shape, this approximation was used for all future numerical calculations.

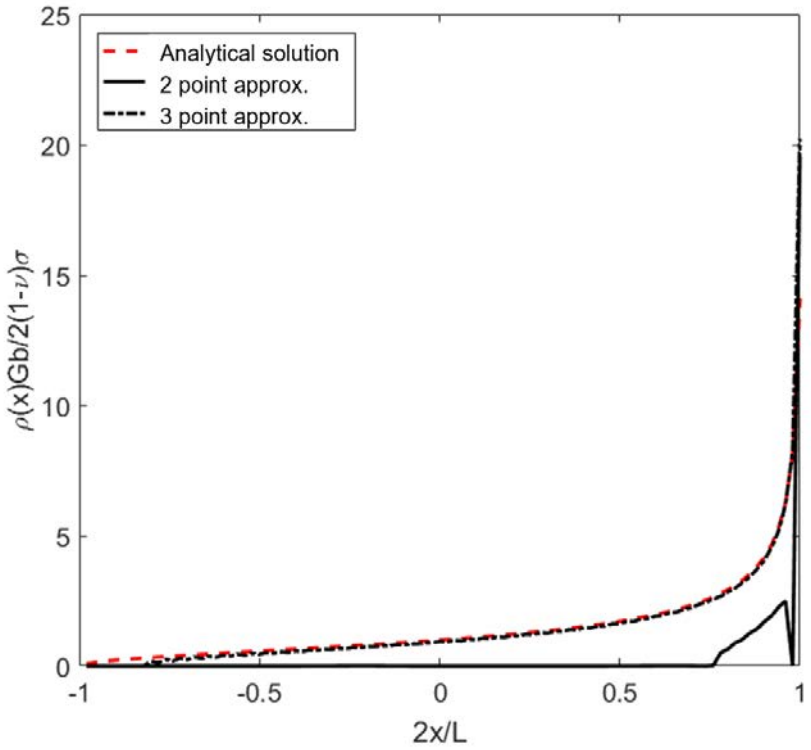

Figure 5.5.1: Comparison of pile-up with different numerical gradient approximations at the boundary for FDM pile-up in a 2 μm domain

5.5.1 FDM single pile-up

Figure 5.5.2 shows an example of the history of the total dislocation population of the domain. The simulations were run until a maximum density was reached indicating the source had stopped generating due to the back stress on the source and the continuum pile-up was arranged in the equilibrium distribution. All pile-up distributions were plotted once they reached this condition.

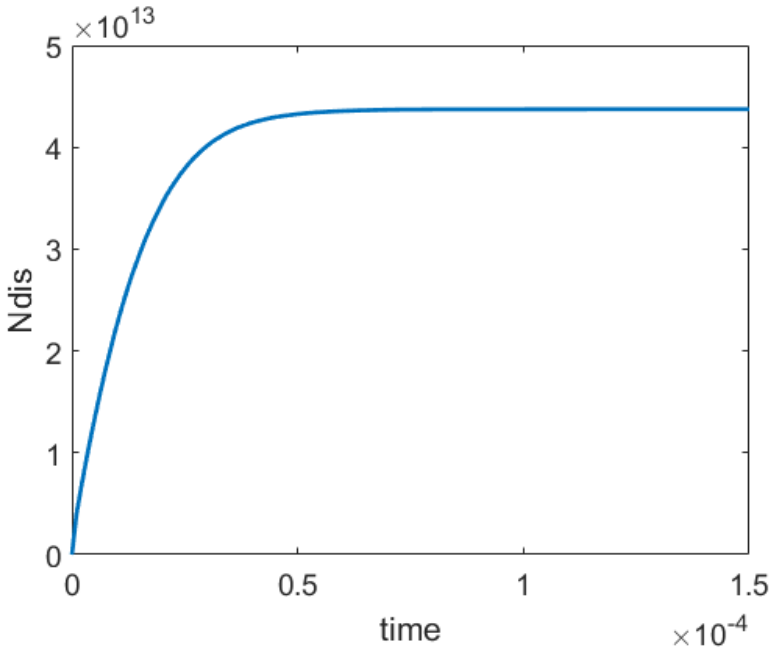

Figure 5.5.2: Generation history in a FDM simulation within a 2 μm domain

As with the grid division size, dx, analysis for the DDD simulations, the grid width in the FDM have an influence on pile-up investigated in Figure 5.5.3. Changing the division size changes the number of points to be simulated and the level of detail of the simulation. The FDM predictions of equilibrium pile-up differed at the grain boundary. The simulations with $dx = 20$ nm captured more of the dislocation density in the steep pile-up gradient at the boundary. Although 20 nm and 50 nm results have a similar shape a closer look outlines a difference in shape and smoothness, see Figure 5.5.4. The $dx = 20$ nm produced a smoother profile than $dx = 50$ nm, but $dx = 20$ nm is below the minimum grid size determined for the continuum. The division size relative to the FDM simulation domain size has to be taken into account maintaining enough points for computational stability whilst staying within the bounds of the continuum length scale.

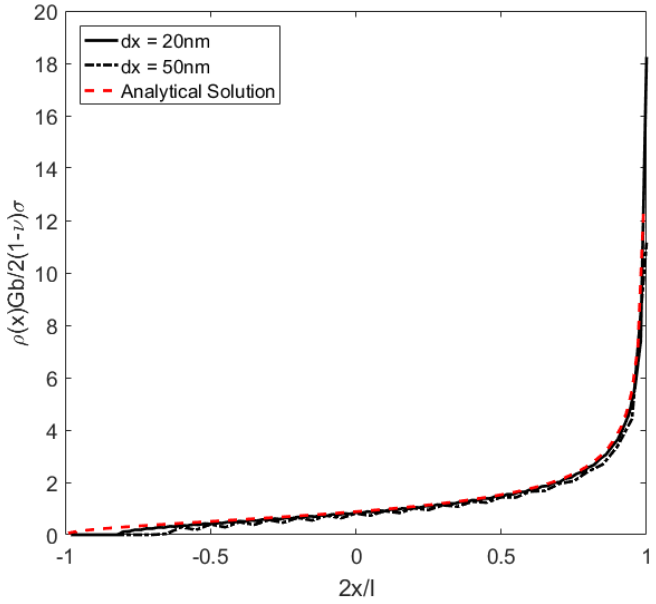

Figure 5.5.3: Comparison of division width, dx, in a $L = 2\,\mu$m domain FDM simulation

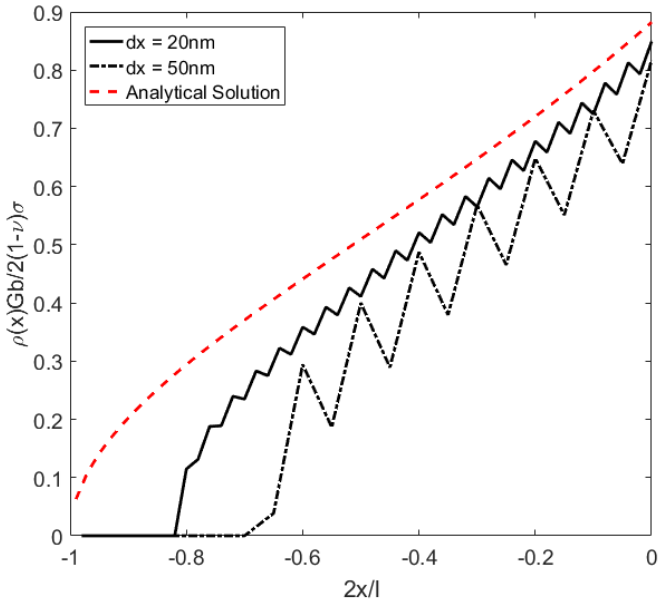

Figure 5.5.4: First half of the pile-up from Figure 5.5.3

One limit of the FDM is instability simulating small domains, for domains less than 5 μm with $dx = 50$ nm minimising the number of points, this creates less stable solutions of the

FDM. Each of the plots in Figure 5.5.5 utilises a grid space one hundredth of the domain length to propagate the dislocation density smoothly into a pile-up configuration. The analytical solution given by Equation (2.2.4) was scaled to have the same total dislocation density as the FDM simulation results to compare the distribution shape. The repulsive force forms the curved pile-up distribution observed at the boundary, as seen in the DDD simulations Section 5.3, indicating the internal stress contributions calculated for the density by Equation (3.3.9) accurately distributed the density. By matching the analytical solution this demonstrated that the FDM model replicated behaviour of same sign dislocations under stress using suitable material parameters similar to that of a Nickel-based superalloy. This was verified for positive dislocation density in Figure 5.5.5 and negative dislocation density in Figure 5.5.6, also demonstrating the inverse nature of the stress fields from the opposite sign Burgers vector of the positive and negative dislocations.

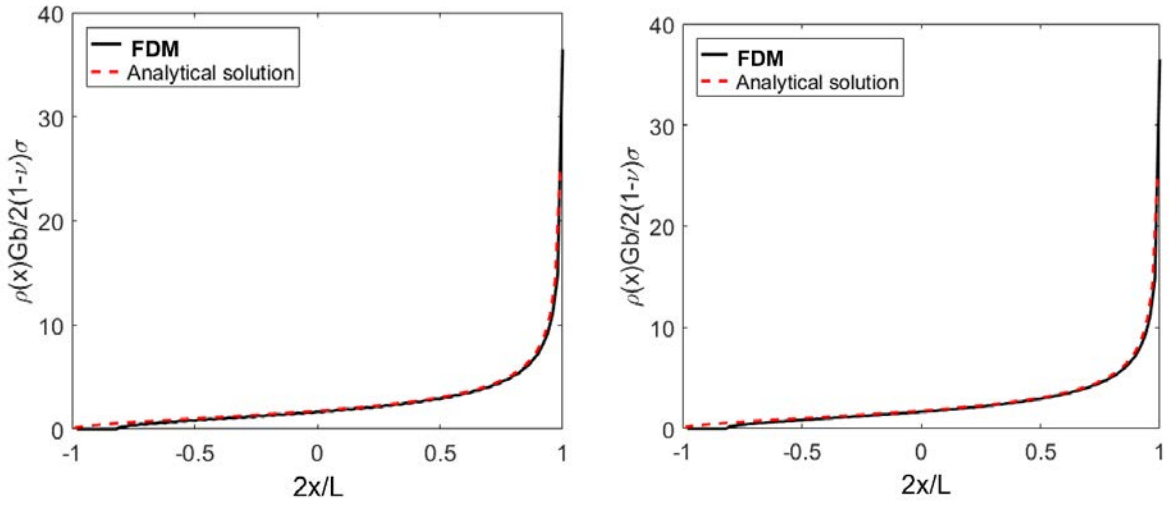

(a) $L = 2\,\mu$m, $dx = 20$ nm (b) $L = 5\,\mu$m, $dx = 50$ nm

Figure 5.5.5: FDM pile-ups of positive dislocation density for different domain lengths

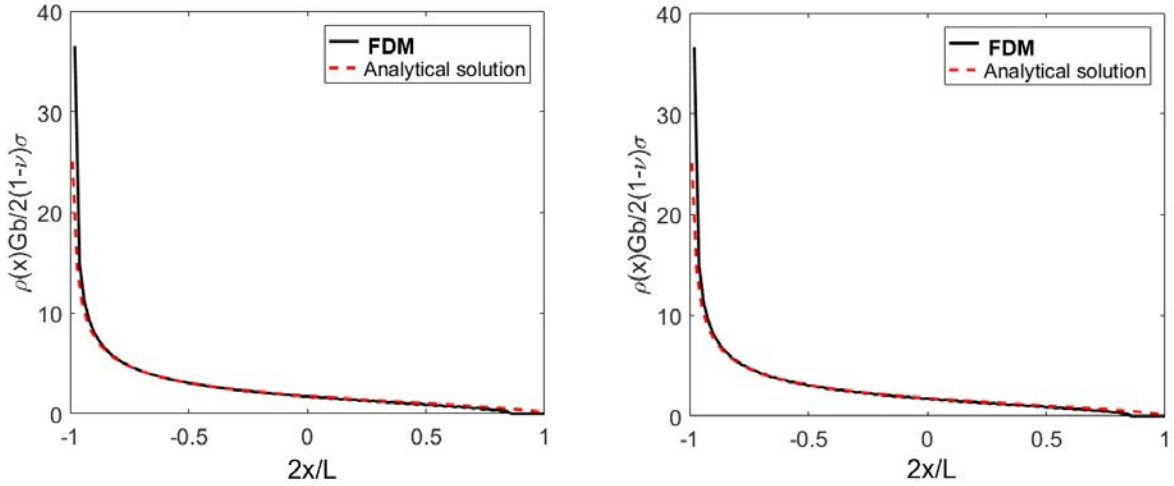

(a) $L = 2\,\mu$m, $dx = 20$ nm

(b) $L = 5\,\mu$m, $dx = 50$ nm

Figure 5.5.6: FDM pile-ups of negative dislocation density for different domain lengths

5.5.2 FDM double pile-up

As dislocations form as loops they create both positive and negative dislocations on the same slip plane, their interaction is a key component in dislocation mobility. Simulations were set up with a Frank-Read source in the centre of the domain producing both positive and negative dislocations where the velocity field was determined by the combination of positive and negative dislocation stress fields. This influenced how the density distributions moved within the domain. The dislocation stress fields are an important factor in dislocation pinning and formation of junctions. The FDM results were compared to the analytical solution of a double pile-up given in equation (2.2.5). Note this simulation did not incorporate any annihilation terms given the positioning of the Frank-Read source and applied stress the positive and negative densities did not meet on the slip domain. Pile-up was examined for multiple length scales using the scaled density axis, $\rho(x)Gb/2(1-\nu)\sigma$, each code used grid spacing $dx = L/100$ along the x-axis, scaling with the domain length.

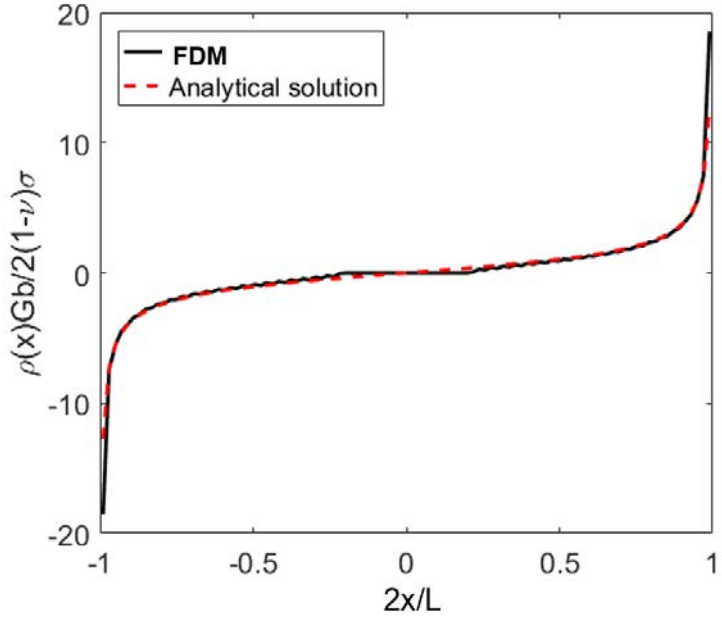

Figure 5.5.7: Positive and negative dislocation density pile-up, L = 2 μm, dx = 20 nm

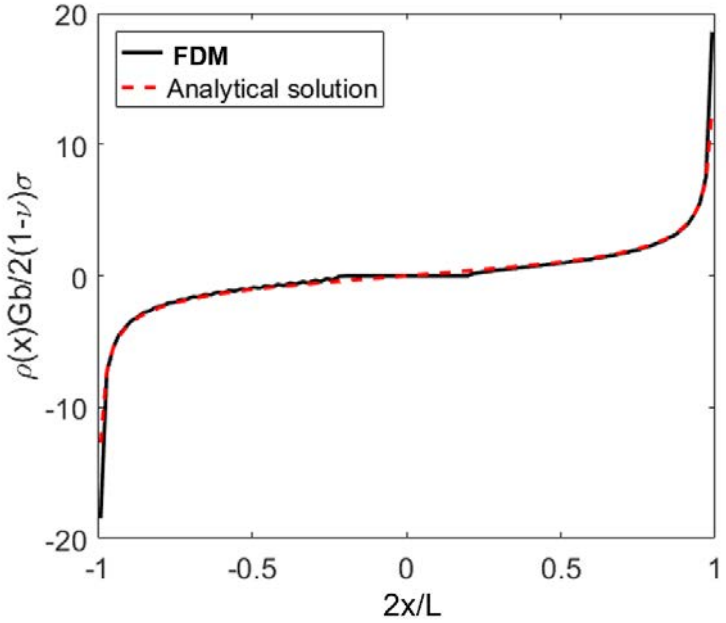

Figure 5.5.8: Positive and negative dislocation density pile-up, L = 5 μm, dx = 50 nm

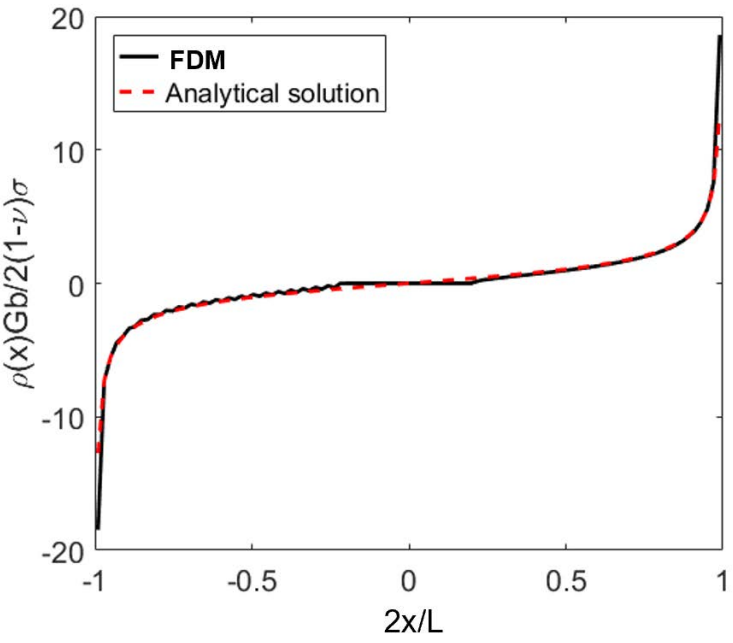

Figure 5.5.9: Positive and negative dislocation density pile-up, L = 10 μm, dx = 100 nm

Figures 5.5.7, 5.5.8 and 5.5.9 show the shape of the dislocation density pile-up from the FDM matched closely to analytical function over multiple length scales. The difference between the continuum model and analytical description is noticeable at the centre where the FDM has no dislocations near to the source location. The influence of stress on pile-up was also replicated to check the shape changes accordingly with the applied stress and the stability of the code at higher applied stress. Instability of the solutions and errors are more likely in the code if the applied stress is too large as it propagates the dislocation density too quickly leading to convergence errors. Results in Figure 5.5.10 show the expected result that more stress leads to more dislocation generation and increases the density of dislocations in the pile-up at the boundaries.

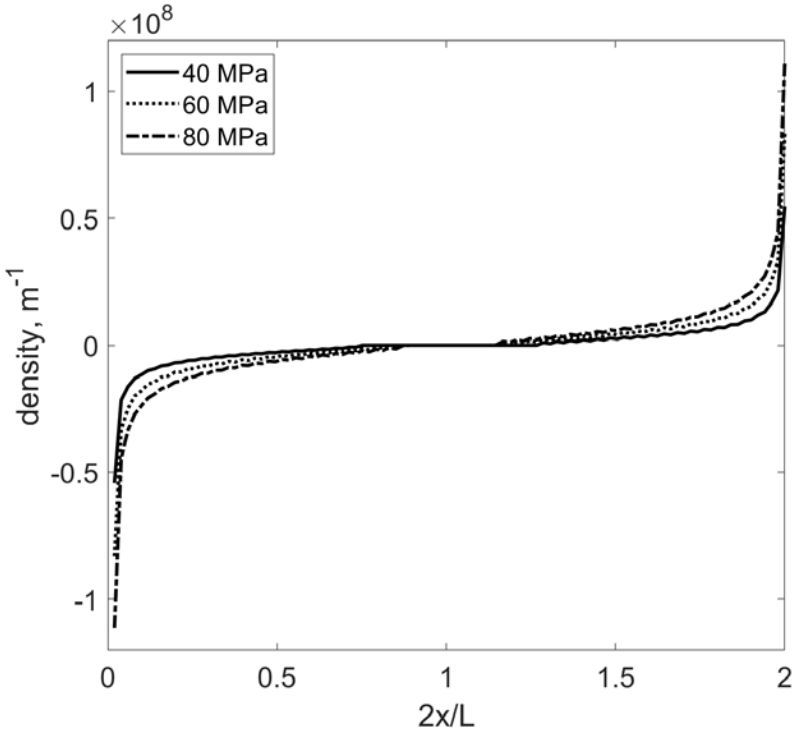

Figure 5.5.10: Double pile-up for different stresses for a domain $L = 5\,\mu$m

Similar anlysis for other continuum models has been carried out by Shulz [79] for an initial conserved Gaussian shaped density distribution that propagates to a pile-up and is compared to the continuum pile-up equation. In the present research the FDM recreates equilibrium pile-up using stress activated dislocation generation.

5.5.3 Two-dimensional FDM

The next step was to develop the FDM code for a two-dimensional domain representing the cross section of a grain, as seen in Figure 5.3.1, but with the density moving on multiple parallel slip planes with interacting stress fields. This provided the capability to model dislocation density evolution across domains to form dislocation slip bands similar to those observed experimentally.

The FDM code for two-dimensions propagates positive dislocation densities through solving the continuity Equation (3.2.18) for both x and y direction force components. For these simulations the densities were confined to glide motion for a single slip system (parallel with the x-axis), as with the pile-up simulations it is assumed the dislocations are moving through a homogeneous γ-matrix, free to slip unimpeded by particles. The distributions on each plane influenced by the external shear stress component resolved on the slip plane and the internal stress fields of the distributions. The results from section 5.3 provided the domain length and grid spacing, set to $L = 5\,\mu$m and $dx = 50$ nm respectively, for the two-dimensional model simulations.

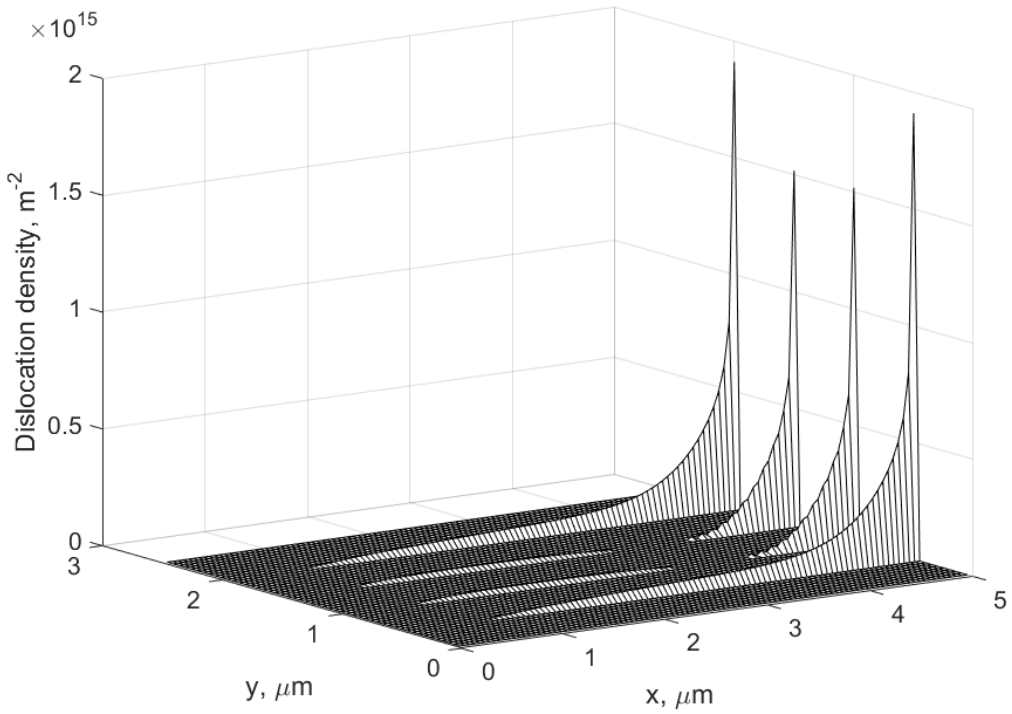

Figure 5.5.11: Single pile-up of positive dislocation density on multiple parallel slip planes

Figure 5.5.11 shows single pile-up of positive density distributions on multiple parallel slip

planes. Positive dislocation density was generated by 4 equally spaced sources on the left hand boundary at $x = 0\,\mu$m. The shape of the pile-up is very similar to that expected but differ on the different slip planes due to the stress field contributions from the neighbouring pile-up distributions. The two middle distributions have a different shape due to the internal stress field created by the other distributions. The distributions are symmetrical in the central y-axis to the distributions, given the nature of the dislocation stress field calculations.

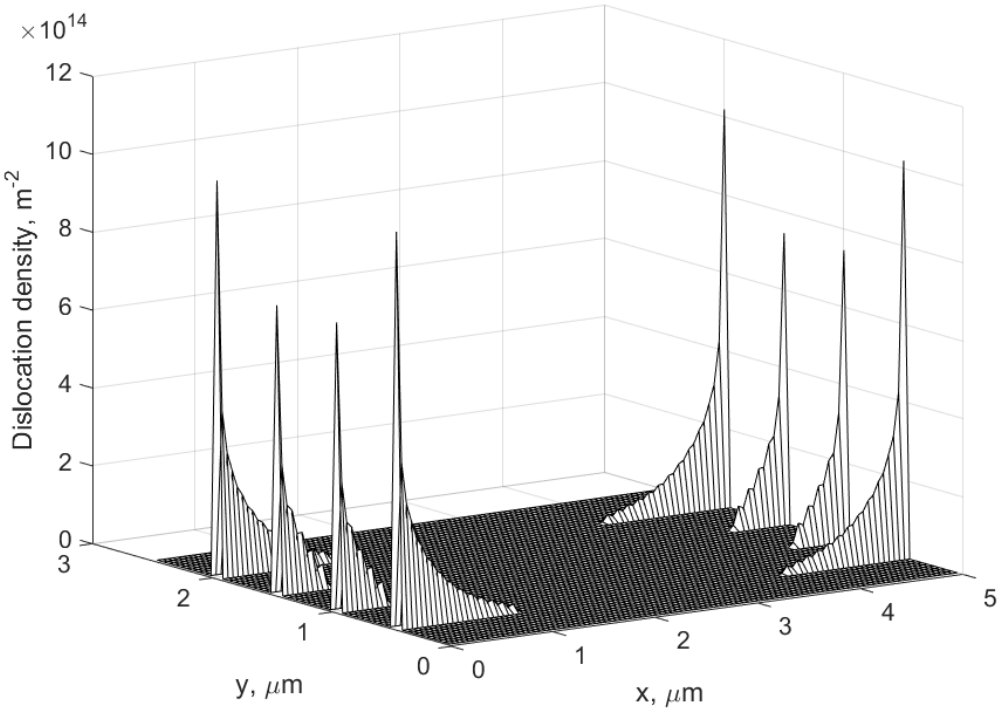

Figure 5.5.12: Double pile-up of positive and negative dislocation density on multiple parallel slip planes

Negative dislocation densities were then introduced into the two-dimensional model evolving a second Equation (3.2.19). Figure 5.5.12 displays double ended pile-up of dislocation densities over four equally spaced slip planes. Sources were placed in the middle of the slip plane producing dislocation density, positive dislocation density pile-up occurring at the domain boundaries at $x = 5\,\mu$m and negative dislocations piled-up at $x = 0\,\mu$m. As with the

one dimensional scenario no annihilation occurred in this set up. The pile-up length on the different planes differ due to the internal dislocation stress field contributions. The distributions in the domain are symmetric due to the symmetric nature of the stress fields and the constant applied stress throughout the domain. The distributions created by the FDM simulations are replicating observed behaviours including formation of slip bands across a grain, of 5 μm in width, and concentration of dislocations at the grain boundaries.

5.6 Discussion

The comparison of the DDD pile-up predictions to analytical solutions of the dislocation pile-up founded a viable length scale limit for the continuum description of dislocations. Defining the continuum length scale was an essential first step for the numerical implementation of the FDM theory. The results in Figure 5.3.7 show the continuum pile-up breaks down sub $L = 900$ nm due to the small amount of dislocations which can be generated in the domain. The grid division size represented by the dislocation density relative to the domain size is also important for closely matching the analytical pile-up solutions, divisions smaller than 50 nm do not capture enough dislocations to accurately recreate the continuum curve, see Figure 5.3.8. As the domain length decreases the grid divisions are relatively larger but contain less dislocations resulting in a less detailed pile-up distribution. Larger domains work better for the continuum scale and the division size can be increased and maintain the same continuum profile, although this would reduce the detail of the model.

Initial continuum simulations indicated accurate pile-up behaviour at non-penetrable boundaries, matching closely to the analytical solutions given by Equation (2.2.4) and Equation (2.2.5) [2]. It was important to take into account the grid spacing relative to the grain size for the detail of the simulation and computational time. Figure 5.5.3 demonstrates the influence of division size relative to the grain size, less stable replication of continuum pile-up

at lower length scales. Larger grid spacing will resolve a less detailed stress field with the stress field Equation (3.3.7). This needs to be considered when modelling microstructural features of the alloy, for example precipitate particles size relative to the the grid spacing, and simulations in small grains will have much less detail than large grains.

The FDM model accounts for positive and negative edge dislocation densities for a single slip system influencing their velocities through their internal stress field interaction and the externally applied stress components. The assumption of the non-local theory is that density representing the dislocations ensemble within the grid spacing has the same stress field of a single edge dislocation scaled by the number of dislocations contained in the density, and succeeded in replicating the analytical pile-up distributions.

The integro-differential Equation (4.1.6) was computationally expensive to solve in two dimensions with the implicit Gauss-Seidel method relying on convergence to a solution over multiple iterations, and the internal stress calculations by summing the stress contribution from each density acting at all other points in the domain. Combined with the small time step used to satisfy the CFL condition (4.1.9) and maintain stability of the implicit finite difference method, simulations take a long time to simulate a small time period of dislocation behaviour, this became more of a limitation with the fatigue simulations performed in Chapter 7.

Some other discrete dislocation behaviour was also considered for how it would apply in the FDM model. Annihilation rates for the FDM were calculated through averaging annihilation events in DDD simulations for multiple random configurations representing dislocation densities of dislocations. Characterised by a power relationship, Equation (5.4.7), and implemented into the FDM framework. Inclusion of this annihilation term is essential for capturing the accurate physics of dislocation interaction. The assumption of the 'super-

dislocation' stress field for the dislocation density was tested using DDD. For the scale of the simulations the differences in the dislocation stress fields due to configuration quickly converge within the distance between density points. The non-local theory could have an effect within the density and these local stress fluctuations due to the dislocation configuration in the density was investigated in chapter 6.

Chapter 6

Influence of stochastic stresses on slip band development

6.1 Introduction

Currently, it is not practical to simulate the flow stress behaviour of two-phase alloys using discrete dislocation dynamics (DDD) over large computational domains that cover multiple grains. An alternative approach is needed, and a continuum description of dislocation transport provides a scheme for modelling the evolution of slip bands within an agglomerate of grains. Continuum theories are based on tracking the evolution of the dislocation density, where elastic interactions are treated as a superposition of the stress field of individual dislocations. In a continuum theory this involves a spatial integral over the dislocation density. However, for a given density at a point in the computational domain, there is any number of possible arrangements individual dislocations can take, see Figure 6.1.1. These different spatial configurations will result in different stresses experienced by the dislocations, which may influence the behaviour of dislocations locally. Thus, the effective stress acting on the dislocation density at some point X is the superposition of there terms: i) the applied stress at X; ii) the dislocation stress from other neighbouring dislocations located at some $X \neq X$;

iii) a fluctuation stress $\delta\tau_{fluc}$ associated with spatial arrangements of dislocations at the point X. Application of the Peach-Koehler equation, each of these will contribute to the dislocation force, i.e., f and in particular an addition term appears in Equation (3.2.21) $\underline{\boldsymbol{f}}^{\infty}$, $\underline{\boldsymbol{f}}^{d}$ and $\underline{\boldsymbol{f}}^{fluc}$. It follows that the expressions for the dislocation velocities require the addition of the additional term $\underline{\boldsymbol{f}}^{fluc}$. Such effects are not dealt with continuum descriptions of the dislocation field and this chapter aims to assess the impact of such interactions on the motion of continuous dislocation field.

The approach adopted in this study differs from previous research by Groma and Bako [54, 55, 68] and Hahner [65–67] for determination of the fluctuation stress distribution, see review in Section 2.4.3. In this work, a series of discrete dislocation dynamics simulations were run using the in-house DDD code, described in Section 5.2, to determine the distribution of stresses acting on dislocation from all other dislocations within a small domain. The size of this domain is chosen to be small compared to that of a crystallographic grain, i.e, significantly smaller than $1\mu m$. This distribution represents the stress fluctuations $\delta\tau_{fluc}$ and will be used to calculate the $\underline{\boldsymbol{f}}^{fluc}$ contribution to the total force.

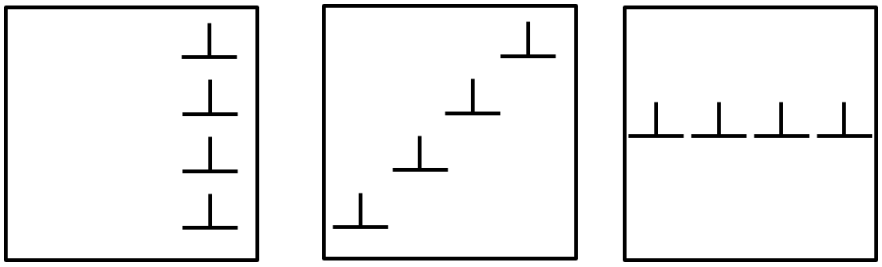

Figure 6.1.1: Sketch of different configurations for the same density

6.2 Stochastic stress distribution

In order to understand the influence of the elastic fields of a group of dislocations has on their motion a series of discrete dislocation dynamics simulations were performed. The aim of

these simulations was to numerically determine fluctuations in the dislocation stress, $\delta\tau_{fluc}$, associated with their spatial arrangements. These fluctuations are defined as the difference of the total dislocation stress in a domain and its mean value. Since the average of an internal equilibrated stress field is zero, the stress fluctuations are the total dislocation stress. The stress values were measured at intervals over the simulation time, and used to determine probability distributions of the dislocation configurations.

DDD simulations were set up in a $(50\text{ nm})^2$ domain, which was equal to the size of a grid point from the FDM model, determined in Chapter 5. Different size populations of dislocations of the same Burgers vector were simulated for random initial dislocation configurations. Stress fluctuations, $\delta\tau_{fluc}$, were averaged over time to allow the initial random configuration of dislocations to rearrange in a lower energy configuration. Initially the domain average was investigated as a function of the sampling average, N. Increasing numbers of sample points were used to find sampling average to which the mean and standard deviation of $\delta\tau_{fluc}$ converged.

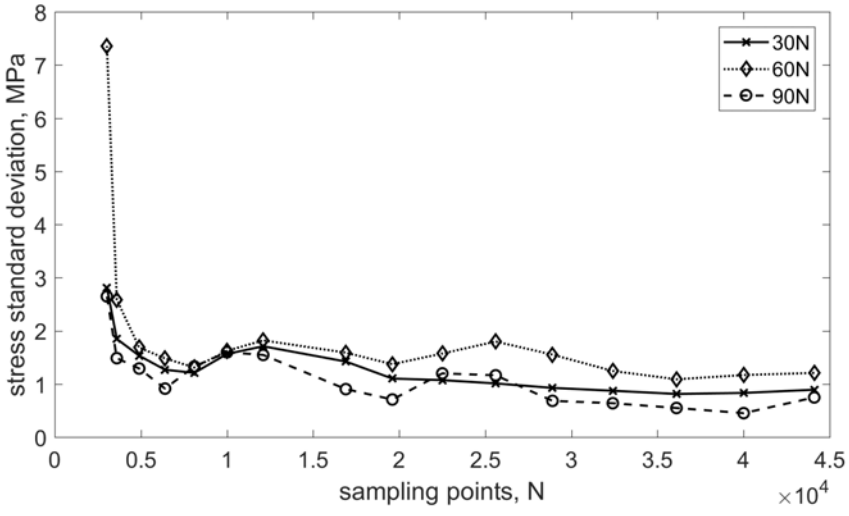

Figure 6.2.1: Convergence of standard deviation of $\delta\tau_{fluc}$ within the domain, for different numbers of dislocations

The standard deviation, or first moment, of $\delta\tau_{fluc}$ varies greatly for less than 0.4×10^4 sampling points but the standard deviation started converging about 1×10^4. An averaging sample of 4×10^4 equally spaced points was selected to sample the average domain stress. Taking a value of 4×10^4 sample points, the average domain stress of 500 random initial configurations was calculated.

The force due to the internal dislocation stress fields is calculated using the Peach-Koehler equation, Equation (3.2.20). Thus the fluctuation of stress can be expressed as a force through the same relation

$$\underline{\boldsymbol{f}}^{fluc} = \underline{\boldsymbol{t}} \times \delta\tau_{fluc} \cdot \underline{\boldsymbol{b}} \tag{6.2.1}$$

The fluctuation force scales stress fluctuation with the Burgers vector. Cumulative probability distribution functions (CDFs) were created by tracking the average of the internal force sampled throughout the domain for each initial configuration, an example can be seen in Figure 6.2.2. These were averaged into one CDF giving the probability distribution of internal force at constant applied stress, as seen in Figure 6.2.3.

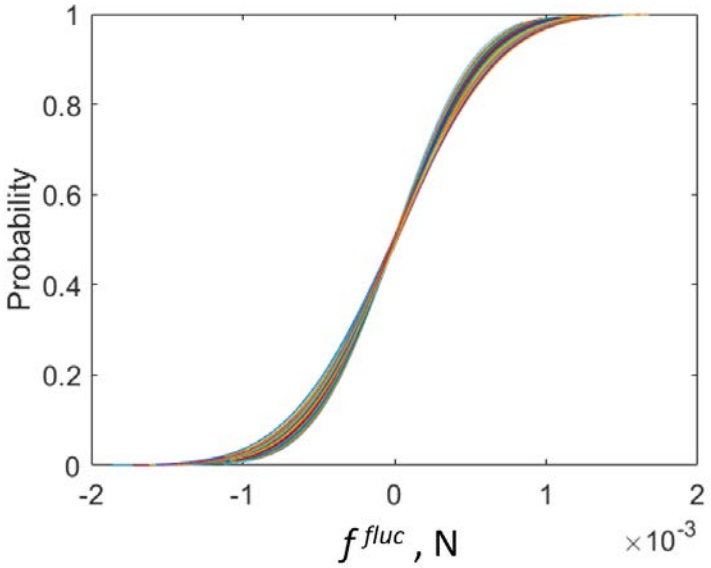

Figure 6.2.2: Cumulative distribution function of the average domain stress of simulations of 40 dislocations for 500 different initial configurations

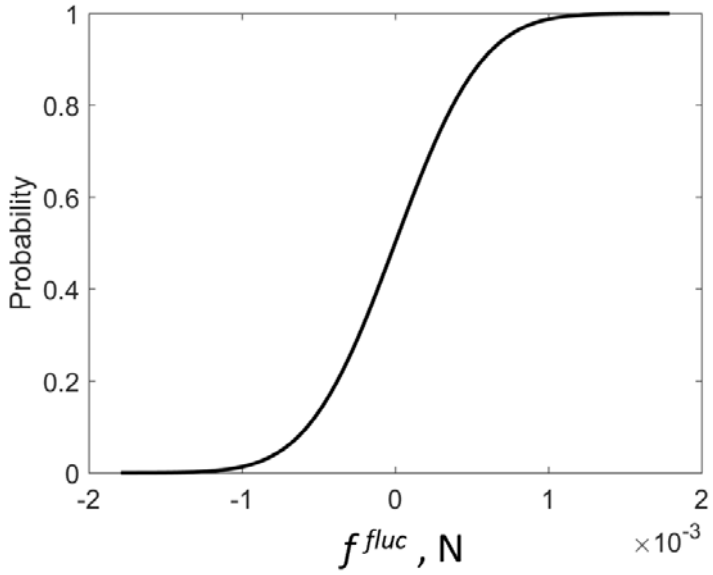

Figure 6.2.3: Averaged cumulative distribution function of the average domain force from the internal dislocation stress field, f^{fluc}, stress field of 40 dislocations for 500 different initial configurations

These DDD simulations were performed for different numbers of dislocations within the same area to compare the change in the CDF shape with density, this was is characterised by the

standard deviation and mean local stress. Figure 6.2.4 plots the correlation between the dislocation density, ρ, and standard deviation of the local force experienced. It displays a linear relationship between two variables, the least squares fit of this plot was used to describe the standard deviation as a function of density. As the number of dislocations increases the range of the stress fluctuation in the domain increases linearly.

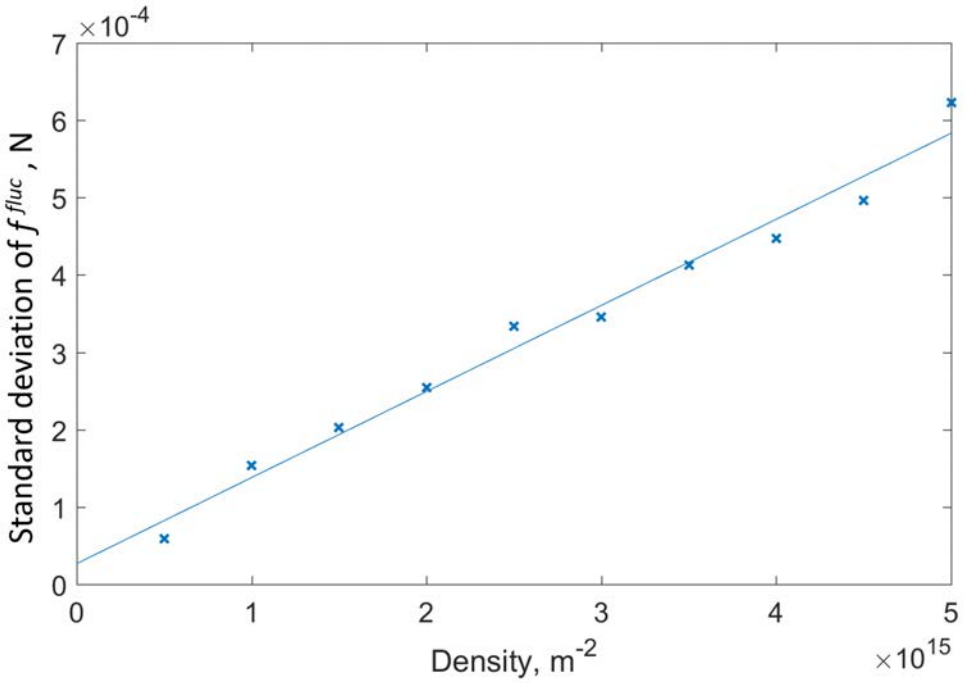

Figure 6.2.4: Standard deviation of f^{fluc} as a function of density for the domain average

Groma et al. [68] has previously used the stress fluctuations felt by individual dislocations tracked in DDD simulations to inform the fluctuation stress term informed by Equation (2.4.8) and Equation (2.4.9). Given that dislocations arrange themselves into configurations to minimise the energy it reflects the fluctuation of stress felt on dislocations within the density. The force fluctuations experienced by the dislocations in each configuration, an example seen in Figure 6.2.5, was used to create the CDF dictating the probability of the internal force fluctuation. The CDF of the force from the internal stress fields acting between dislocations in 500 simulations of 40 positive dislocations with different initial configurations

is shown in Figure 6.2.6 showing the difference in stress ranges between each configuration and the shared mean stress of zero. These were averaged into a CDF from all 500 initial dislocation configurations in Figure 6.2.7.

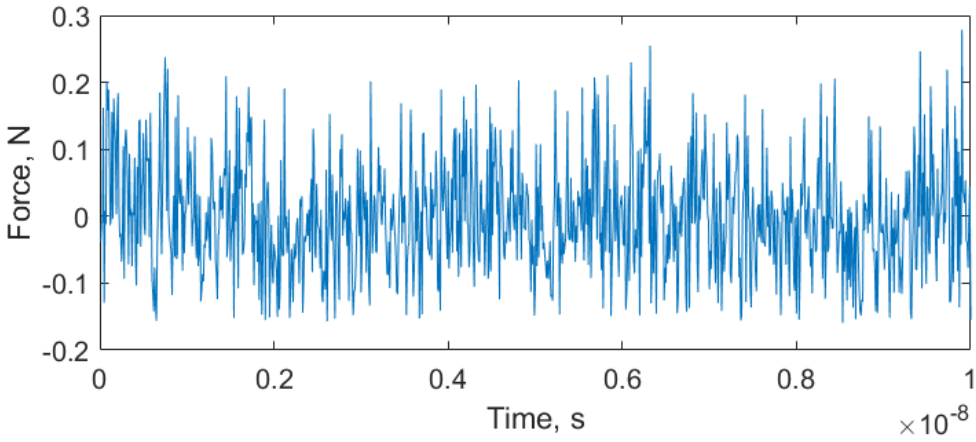

Figure 6.2.5: Example of the average force from internal stress field felt on a dislocation during a DDD simulation

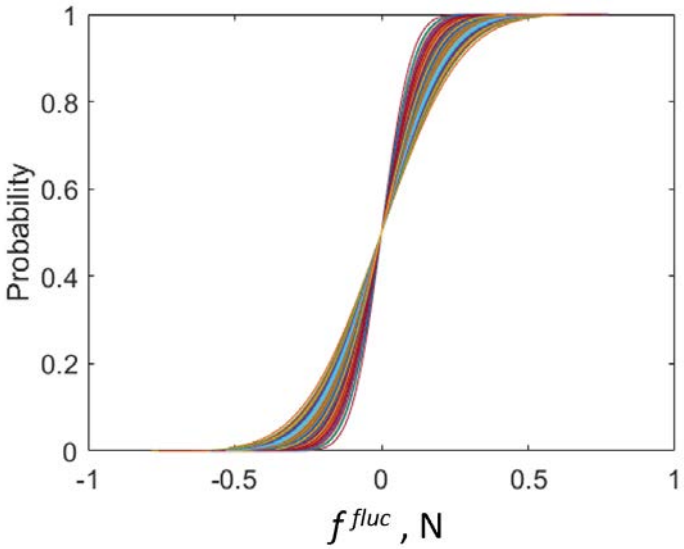

Figure 6.2.6: Cumulative distribution functions of the average internal force felt by 40 dislocations for 500 different initial configurations

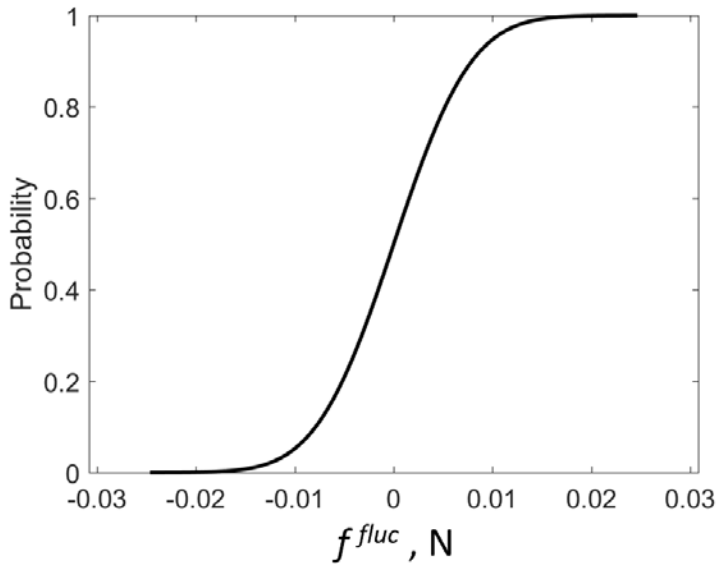

Figure 6.2.7: Averaged cumulative distribution function of the average internal force, f^{fluc}, experienced by the 40 dislocations for all 500 different initial configurations

The dislocation stress CDFs were created for increasing dislocation density, each averaged over 500 simulations for different initial random dislocation configurations. This created a scalable relationship between the standard deviation of the CDF and the density, shown in Figure 6.2.8.

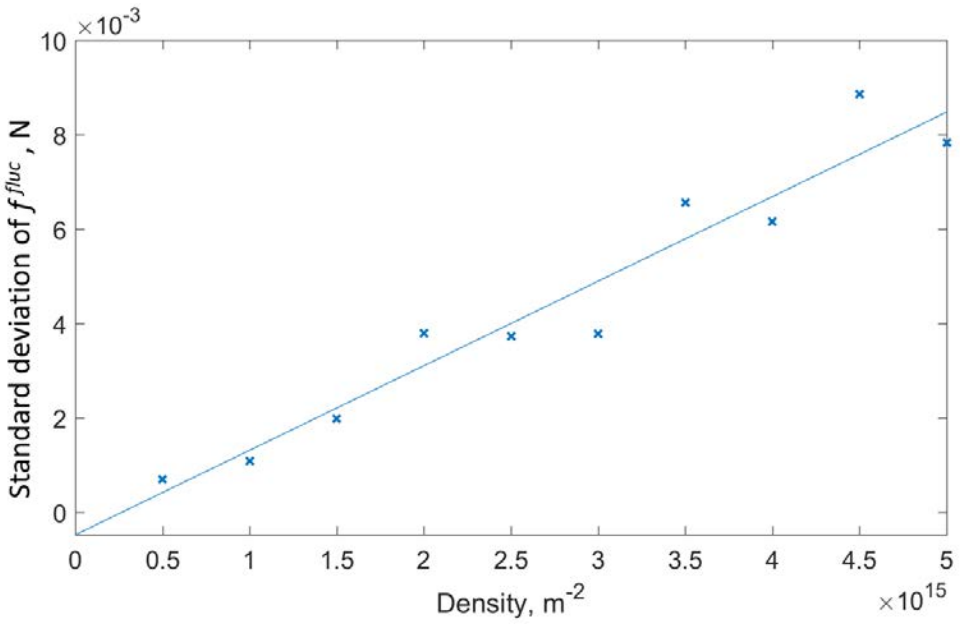

Figure 6.2.8: Standard deviation of f^{fluc} as a function of density for the average stress felt on the dislocations

The dislocation average for the standard deviation of f^{fluc} is an order of magnitude larger than that of the domain average. The gradient of this line relating the density and the standard deviation of the force fluctuations experienced in DDD simulations is given by

$$SD^{fluc}(x) = 2.0 \times 10^{-18} \rho(x) \tag{6.2.2}$$

The domain average fluctuation would be important for dislocations entering the domain or sources activating within the domain but in terms of short range dislocation correlations it was decided the take the range of stresses felt by each dislocation within the ensemble. This would better capture the local stress fluctuations of the ensemble influencing its own movement.

To implement the stochastic effects into the FDM theory the local stress fluctuation term was determined from a density dependent CDF, following existing methods in the format

of Equation (2.4.11) [54]. The internal force fluctuation value, $\underline{\boldsymbol{f}}^{fluc}$, was selected randomly from the CDF described by

$$P(\underline{\boldsymbol{f}}^{fluc}(\underline{\boldsymbol{x}})) = \frac{1}{2}\left(1 + erf\left(\frac{\underline{\boldsymbol{x}}}{SD^{fluc}(\underline{\boldsymbol{x}})\sqrt{2}}\right)\right) \tag{6.2.3}$$

for a Gaussian cumulative probability distribution that scales with the standard deviation, SD^{fluc}, as a function of $\rho(\underline{\boldsymbol{x}})$ through equation (6.2.2). The probability distribution function (6.2.3) was introduced into the FDM formulation. The value of $\underline{\boldsymbol{f}}^{fluc}$ at each location $\underline{\boldsymbol{x}}$ was generated by first calculating the standard deviation of the stress fluctuations from the linear relation in Figure 6.2.8. Subsequently this value was used to shape the the probability distribution (6.2.3). A randomly generated probability value between 0 and 1 was interpolated from the CDF for (6.2.3) to give a value internal fluctuation. This introduced an additional term $\underline{\boldsymbol{f}}^{fluc}(\underline{\boldsymbol{x}}, t)$ to dislocation transport equation (3.2.18) to create the new stochastic advection equation to drive the temporal density evolution

$$\frac{\partial \rho(\underline{\boldsymbol{x}}, t)}{\partial t} + \underline{\boldsymbol{\nabla}} \cdot \left[\rho(\underline{\boldsymbol{x}}, t)\underline{\boldsymbol{v}}\left(\underline{\boldsymbol{f}}(\underline{\boldsymbol{x}}, t)\right)\right] = \dot{A}^{+}(\underline{\boldsymbol{x}}, t) - \dot{A}^{-}(\underline{\boldsymbol{x}}, t) \tag{6.2.4}$$

where $\underline{\boldsymbol{f}} = \underline{\boldsymbol{f}}^{mot}(\underline{\boldsymbol{x}}, t) + \underline{\boldsymbol{f}}^{fluc}(\underline{\boldsymbol{x}}, t)$. Expressions for drag, jog and climb controlled velocities as functions of the force per unit length on the dislocations are given in Section 3.4.

6.3 Effect of stochastic fluctuations on the uniaxial flow stress

The influence of the stochastic fluctuations on the flow stress will now be assessed. As discussed in the previous section, this is accounted for by introducing an additional force term f^{fluc} when calculating the dislocation velocity used in equation (6.2.4). In these simulations a unimodal precipitate distribution representative of secondary γ' dispersions found in fine

grain RR1000 was used: volume fraction of 0.3 and mean particle radius of 100 nm. To account for variations of the γ' dispersion parameters a second distribution was analysed with a volume fraction of 0.33 with same size particles. These particle distributions are shown in Figure 6.3.1. Simulations were carried out at 800°C since at this temperature much of the tertiary γ' have dissolved thereby justifying the unimodal precipitate distribution.

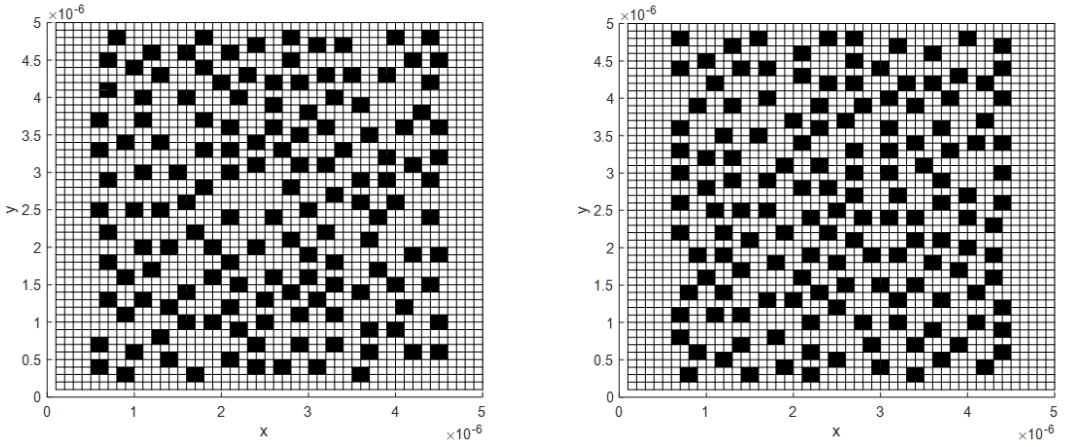

(a) $R_s = 100$nm, $\Phi_s = 30\%$ (b) $R_s = 100$nm, $\Phi_s = 33\%$

Figure 6.3.1: Particle distributions for FDM simulations with stochastic stress component

Initially, simulations were run for systems of positive sign dislocations generated at the left hand boundary of a computational domain. The flow stress response of the domain was examined up to 3% strain as building towards a fatigue model this is well above the strain range planned for simulations. For each γ' distribution three simulations were performed with the stochastic FDM to allow for a scatter driven by f^{fluc} value. The plotting labels for the three instances of the stochastic stress simulations are labelled; *'fluctuation 1'*, *'fluctuation 2'* and *'fluctuation 3'*. The FDM simulations with no stress fluctuation component is labelled as *'no fluctuation'*. Figure 6.3.2 and Figure 6.3.3 show the influence of the stochastic force on the flow stress curves from the adapted FDM simulations. They show that f^{fluc} has very little effect on the plastic deformation of the predicted flow stress behaviour.

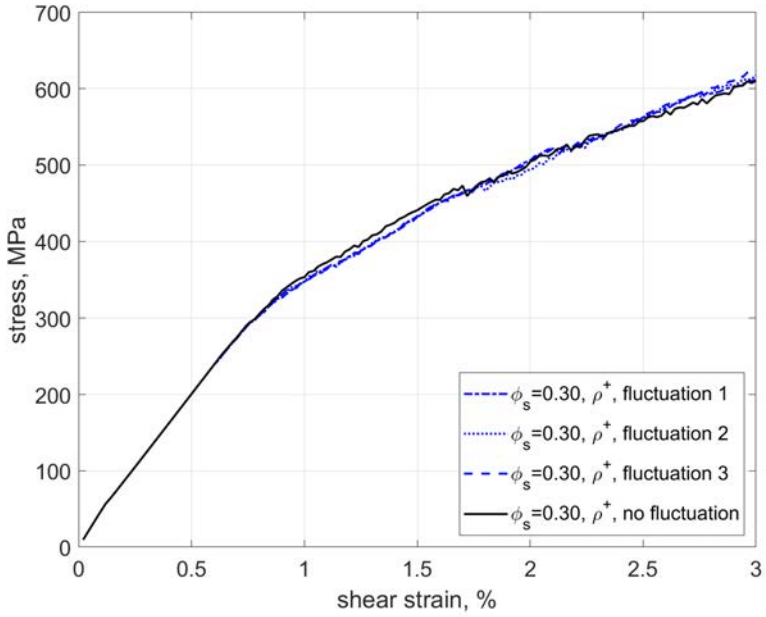

Figure 6.3.2: Flow stress comparison for FDM simulations with the stochastic fluctuating force on the $\Phi_S = 0.30$ distribution. Positive dislocations only.

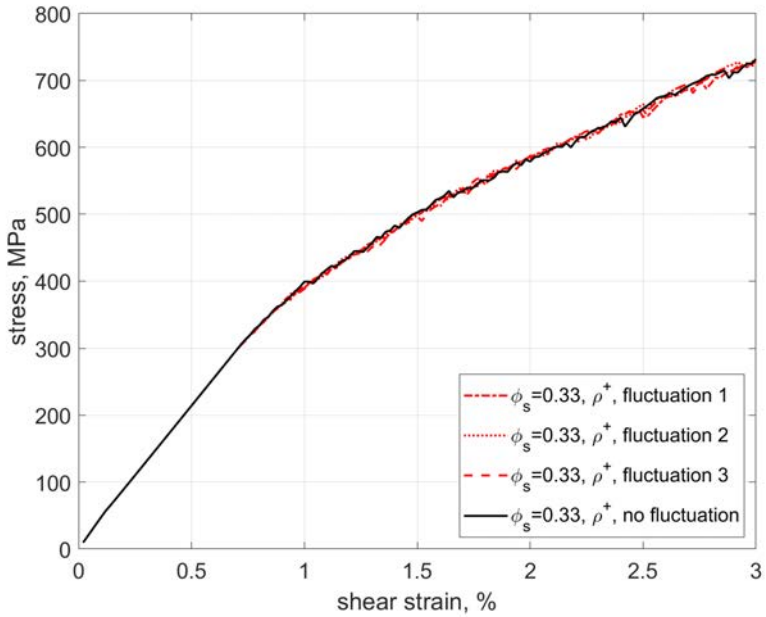

Figure 6.3.3: Flow stress comparison for FDM simulations with the stochastic fluctuating force on the $\Phi_S = 0.33$ distribution. Positive dislocations only.

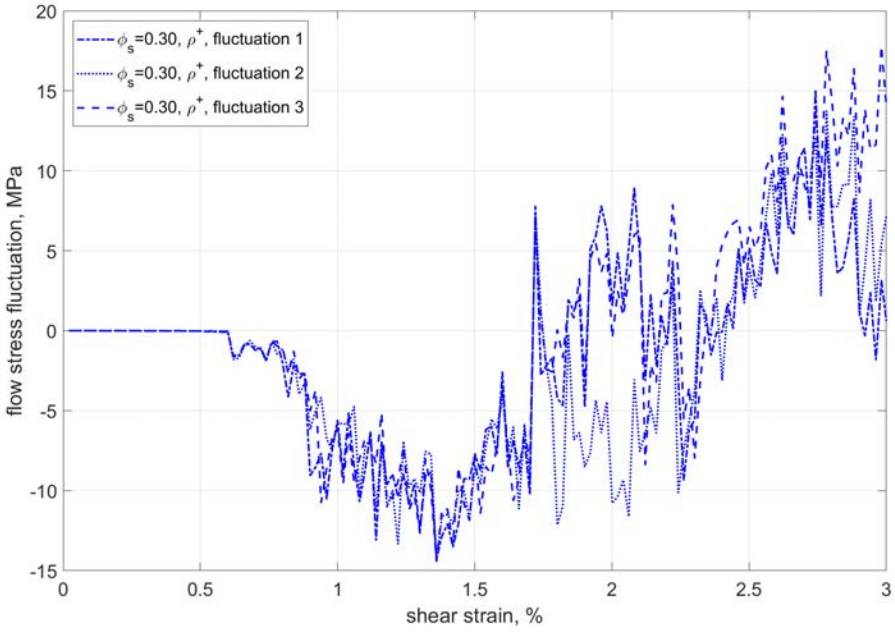

Figure 6.3.4: Flow stress fluctuations representing the difference between FDM solutions with and without f^{fluc} for $\Phi_S = 0.30$. Positive dislocations only.

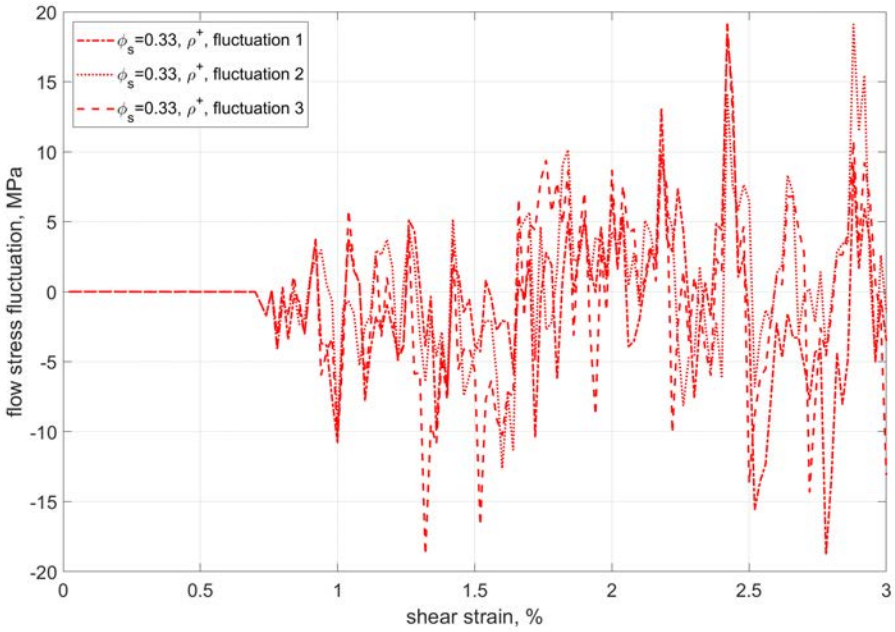

Figure 6.3.5: Flow stress fluctuations representing the difference between FDM solutions with and without f^{fluc} for $\Phi_S = 0.33$. Positive dislocations only.

A useful measure to assess the influence of the stochastic force term on the flow stress, is the difference in flow stress between the FDM solutions with and without the $\underline{\boldsymbol{f}}^{fluc}$ term. These flow stress fluctuations are plotted in Figure 6.3.4 and Figure 6.3.5. The flow stress fluctuations are predicted to increase with increasing strain, which is associated with the build-up of the dislocation density. However, these fluctuations appear to stabilise after 2% strain. The $\Phi_S = 0.30$ distribution sees a larger average difference of 5.23 MPa, while for the $\Phi_S = 0.33$ distribution this value was 3.46 MPa.

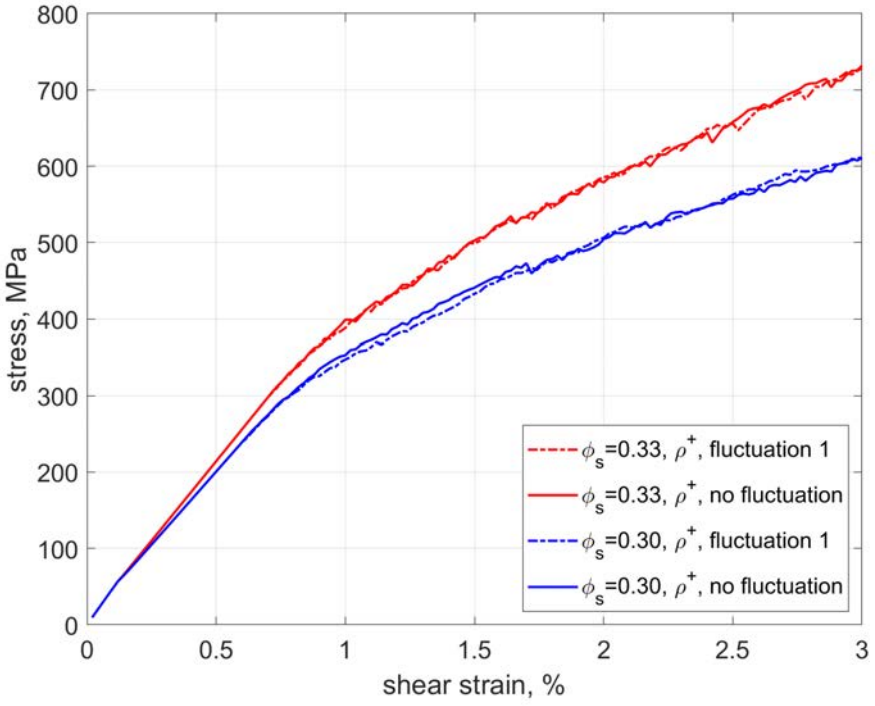

Figure 6.3.6: FDM simulations comparing the first stochastic simulation and non-fluctuating run flow stress curves in the γ' distributions of $R_s = 100$ nm, $\Phi_S = 0.30$ and $\Phi_S = 0.33$. Positive dislocations only.

There is a clear influence of γ' on the flow stress response, with the $\Phi_S = 0.33$ dispersion distribution showing more hardening than the $\Phi_S = 0.30$ dispersion solutions, as shown in Figure 6.3.6. This behaviour corresponds to the larger interparticle spacings in the $\Phi_S = 0.30$ γ' dispersion when compared the $\Phi_S = 0.33$ volume fraction dispersion, see Figure 6.3.1,

resulting in more slip events. This is better illustrated in Figure 6.3.7, which shows maps of the plastic deformation gradient component F^p_{12}. It can be seen that more concentrated slip is predicted for $\Phi_S = 0.30$.

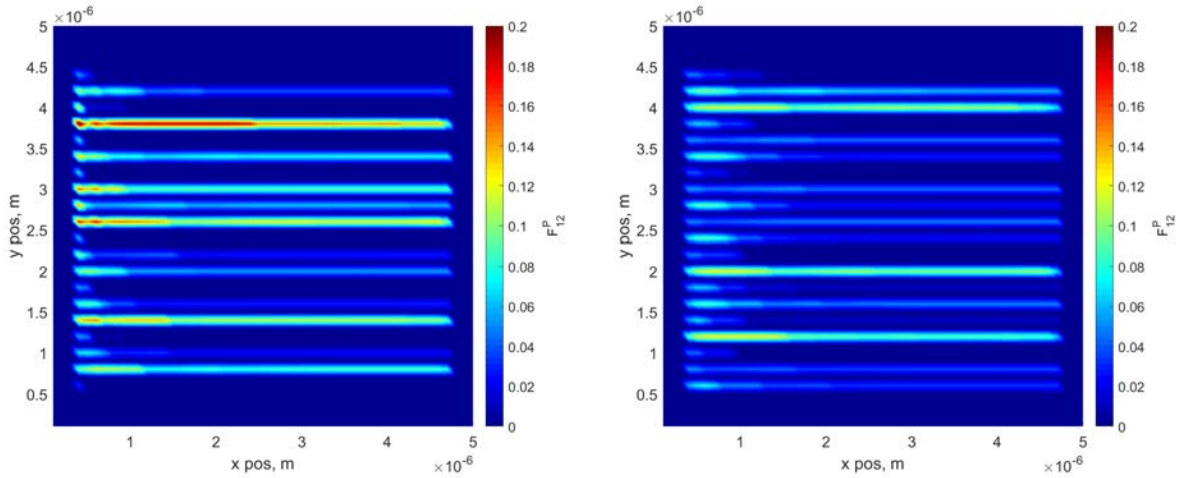

(a) Plastic deformation for $\Phi_s = 30\%$ (b) Plastic deformation for $\Phi_s = 33\%$

Figure 6.3.7: Plastic deformation gradient, F^p_{12}, maps for two distributions, without stress fluctuation term, ρ^+ only, taken at $\epsilon = 3\%$.

For the same particle distributions, the stochastic FDM simulations were run with the negative dislocations. The negative dislocation sources were evenly distributed on the right hand side of the domain. To ensure the same total number of dislocation sources, and similar amount of dislocation generation, there are half the number of positive dislocation sources now the negative dislocation sources have been added to the other side of the domain. These positive and negative dislocation sources were aligned to promote dislocation annihilation events. Given the symmetric nature of the dislocation stress fields the same stress fluctuation characterisation was used for negative dislocation densities as was used for the positive densities described by Equation (6.2.3). The annihilation rate for dislocations where opposite sign densities interact was defined by equation (5.4.7). Again three simulations were run with the stress fluctuation term and one without compared as a baseline.

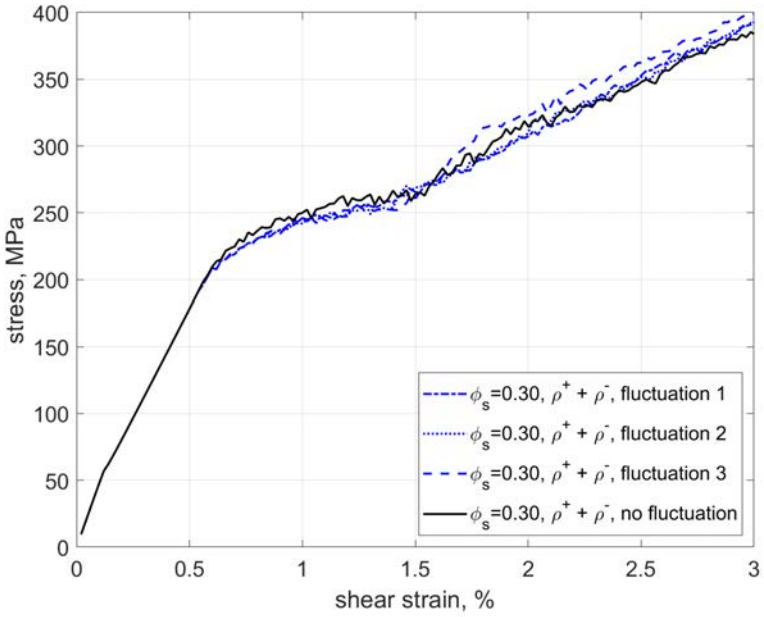

Figure 6.3.8: Flow stress comparison for FDM simulations with the stochastic fluctuating stress term on the $\Phi_S = 0.30$ distribution. Positive and negative dislocations.

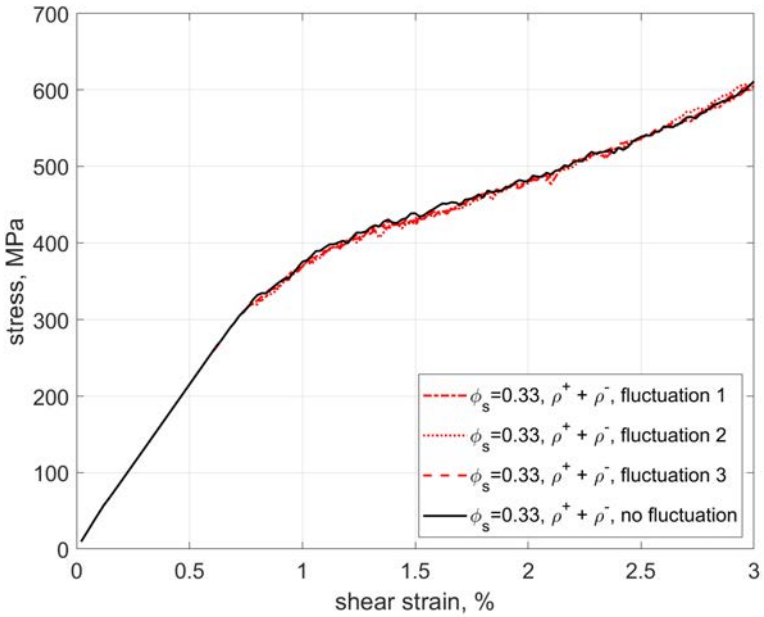

Figure 6.3.9: Flow stress comparison for FDM simulations with the stochastic fluctuating stress term on the $\Phi_S = 0.33$ distribution. Positive and negative dislocations.

The flow stress results for the mixed dislocation simulations are shown in Figure 6.3.8 and Figure 6.3.9. The stochastic FDM results show a very similar differences in plastic response to the simulations without the stochastic term as seen with the simulations of only positive dislocations. It is noted that the hardening behaviour in these simulations is different to those obtained with the transport of positive dislocations. Also a larger difference in flow stresses is predicted between the $\Phi_S = 0.30$ and $\Phi_S = 0.33$ cases for simulations with opposite signed dislocations when compared to those with positive dislocations only. The reason for this difference is that the number of dislocation slip events is increased when considering positive and negative dislocation populations.

The average fluctuation of the flow stress for the $\Phi_S = 0.33$ distribution in Figure 6.3.10 is 6.14 MPa. For the $\Phi_S = 0.33$ distribution in Figure 6.3.11 this value is 3.15 MPa. These are very similar amount to the equivalent simulations using only positive dislocations. Where the average fluctuation of the flow stress curves are 5.23 MPa and 3.46 MPa for $\Phi_S = 30\%$ and $\Phi_S = 33\%$ respectively. The added negative dislocations did not increase the fluctuation of stress response.

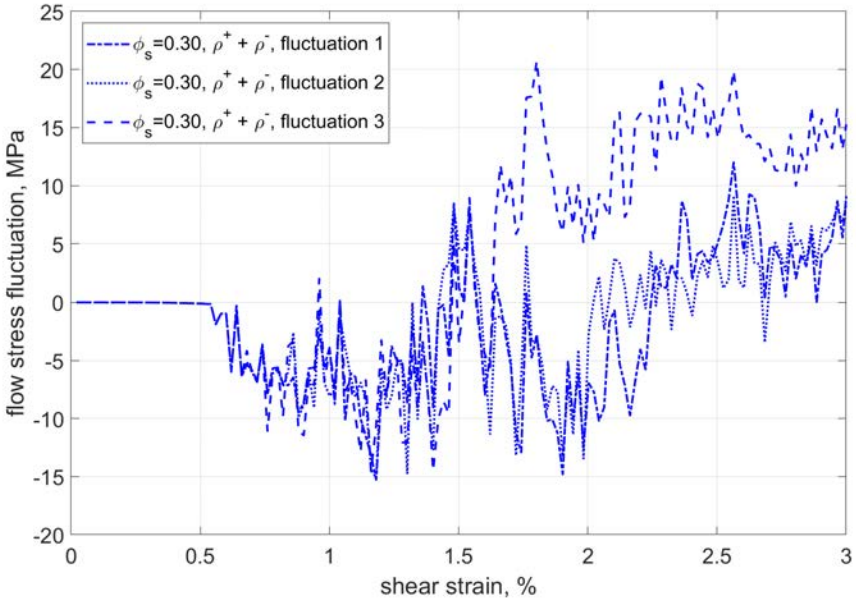

Figure 6.3.10: Flow stress fluctuations representing the difference between FDM solutions with and without f^{fluc} for $\Phi_S = 0.30$. Mixed dislocations.

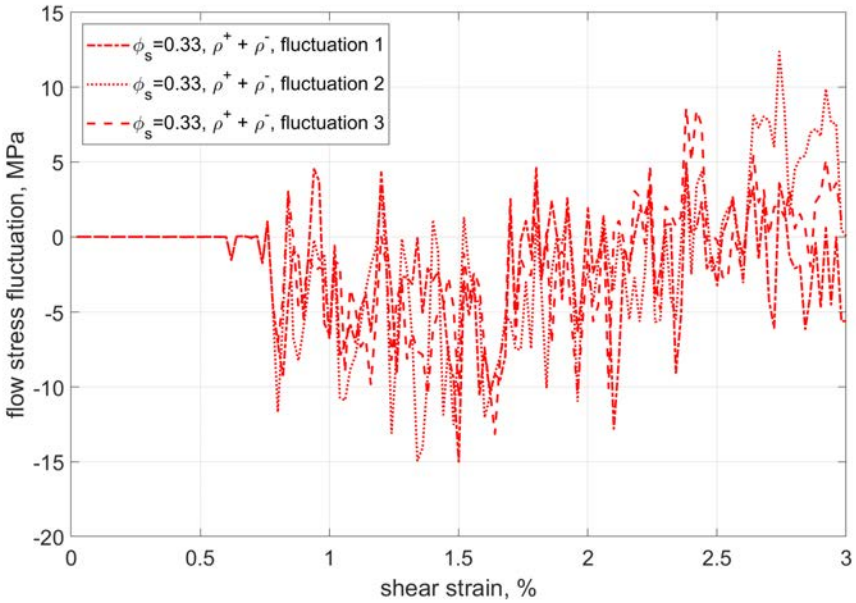

Figure 6.3.11: Flow stress fluctuations representing the difference between FDM solutions with and without f^{fluc} for $\Phi_S = 0.33$. Mixed dislocations.

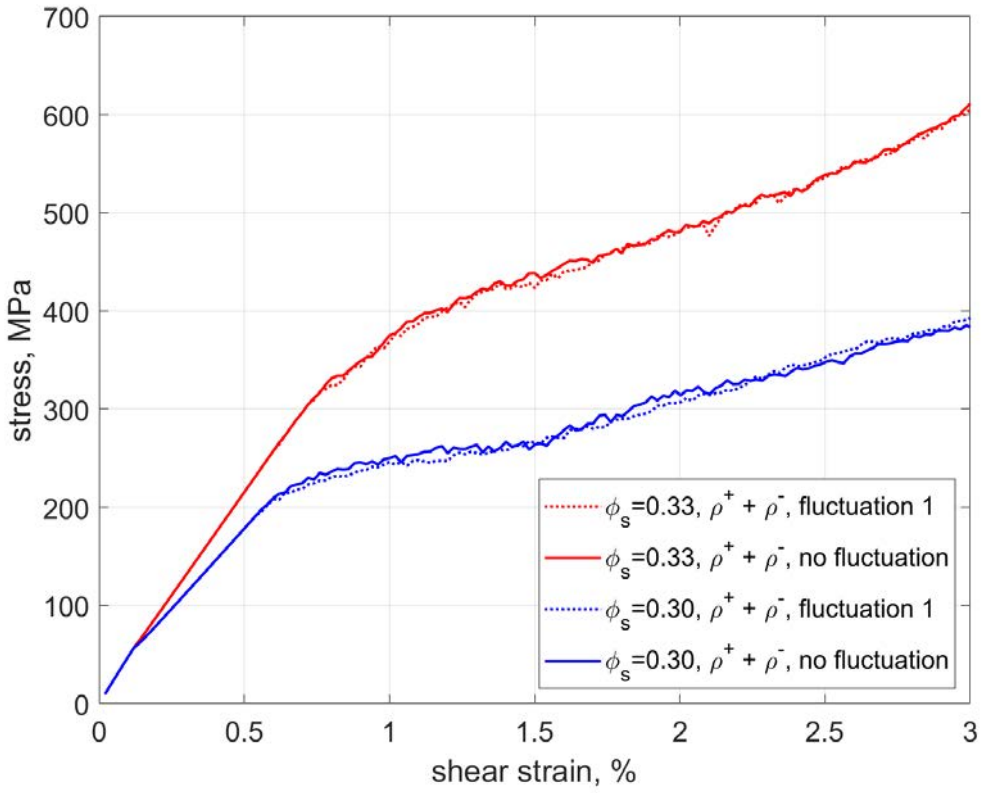

Figure 6.3.12: Comparison of flow stress curves for $\Phi_S = 0.30$ and $\Phi_S = 0.33$ for positive and negative dislocation densities

Comparison of the stochastic simulations on flow stress in relation to the different microstructures, as seen in Figure 6.3.12, again shows the difference in hardness for the two volume fractions with the harder $\Phi_S = 0.33$ distribution. With the mixed dislocation density there is a significant drop in the yield stress for $\Phi_S = 0.30$ relative to $\Phi_S = 0.33$. Figure 6.3.13 shows the difference in the plastic deformation gradients at low strain. The $\Phi_S = 0.30$ displays significantly more concentrated deformation gradients developing from both sides of the computational domain at low strain due to the increased spacing between the particles.

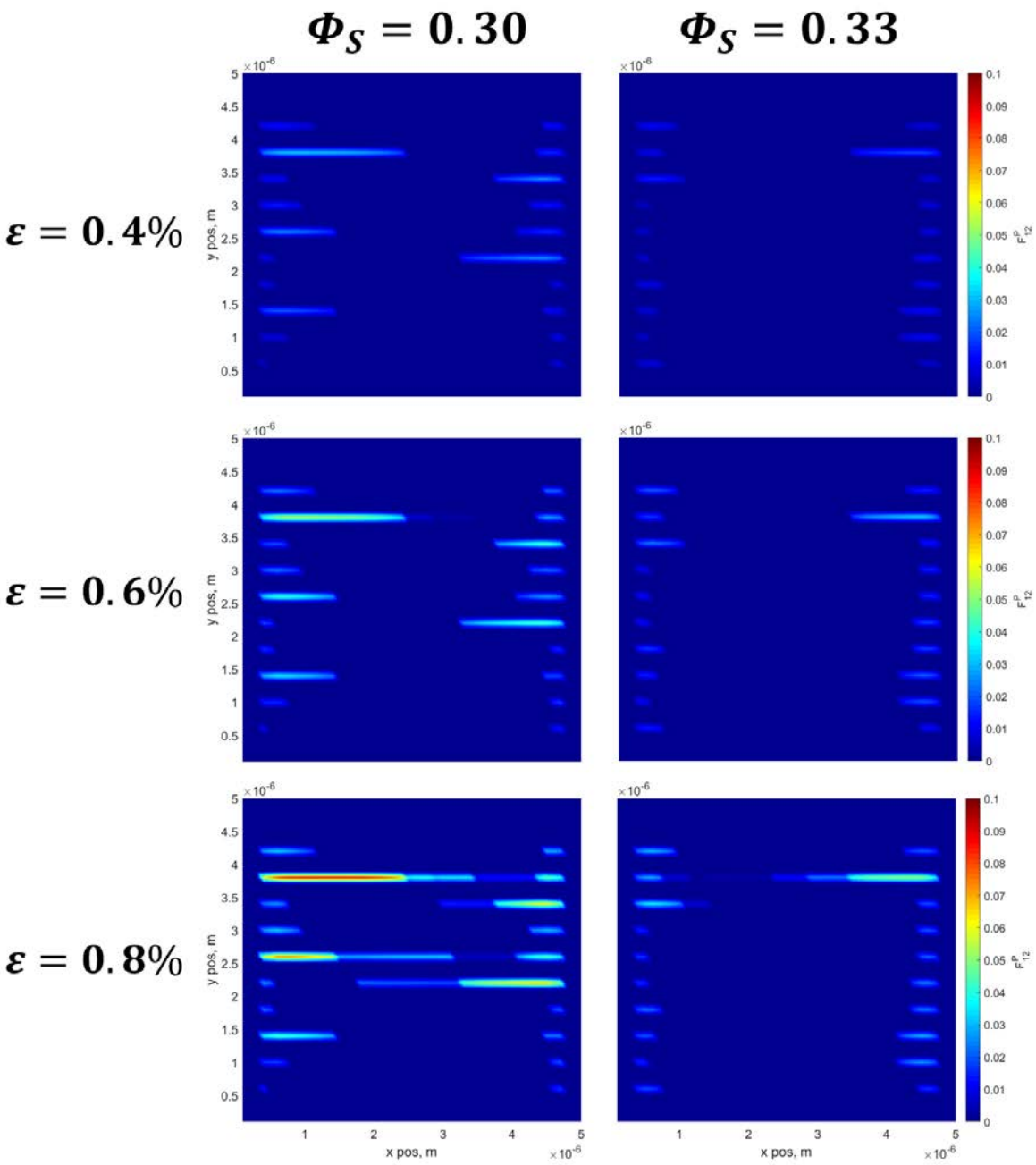

Figure 6.3.13: Plastic deformation gradient, $\boldsymbol{F}^p_{12}$, maps at low strain without stress fluctuation term, ρ^+ and ρ^- for $\Phi_S = 0.30$ and $\Phi_S = 0.33$

Figure 6.3.14 shows the difference in the total annihilation history, where the $\Phi_s = 30\%$ distribution saw more dislocations annihilated. It also reveals that no dislocation annihilation occurs until $\epsilon = 0.7$ when the dislocations achieve sufficient stress to cut the γ' particles.

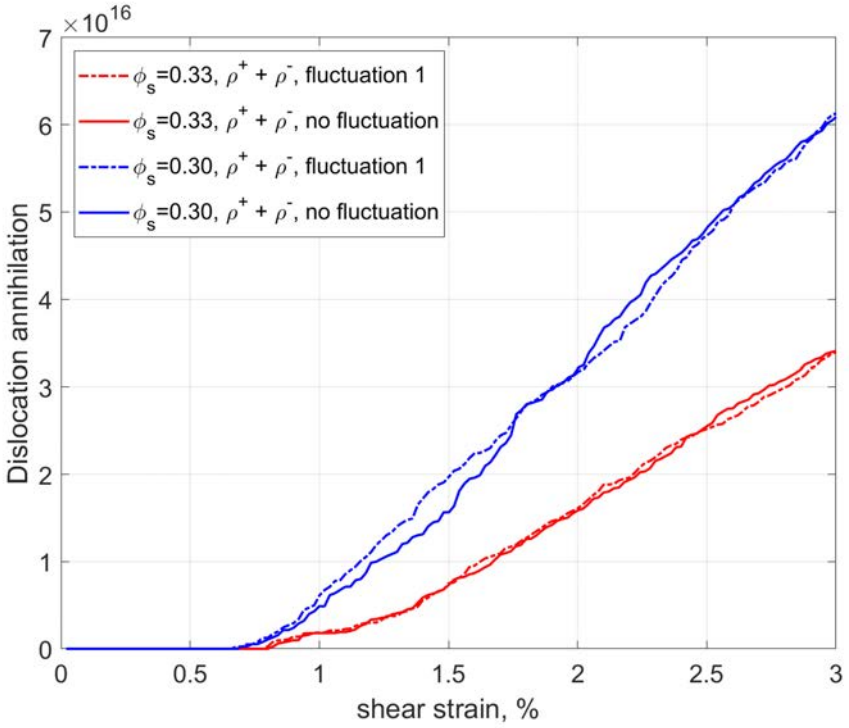

Figure 6.3.14: Comparison of total annihilation of $\Phi_S = 0.30$ and $\Phi_S = 0.33$ for fluctuating stress run 1 and the non-fluctuating run of the positive and negative dislocation densities

Maps showing where the dislocation densities annihilated are presented in Figure 6.3.15. A higher density of annihilation is observed along the slip bands at $\Phi_s = 0.30$. This is linked to the increased dislocation population shearing the domain and meeting to annihilate as the annihilation rate, Equation (5.4.7), scales with the densities.

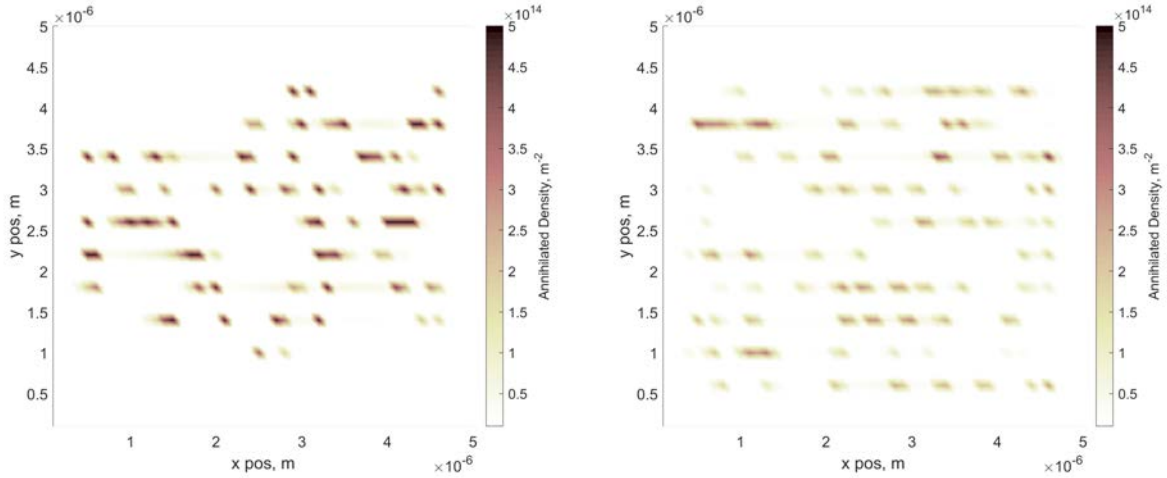

(a) Total dislocation annihilation for $\Phi_s = 0.30$ (b) Total dislocation annihilation for $\Phi_s = 0.33$

Figure 6.3.15: Total dislocation annihilation maps for two distributions, without stress fluctuation term at $\epsilon = 3\%$

The introduction of the negative dislocation density field and annihilation rate clearly influenced the hardness of the material in the FDM simulations. Higher densities of dislocations in theses cases resulted in more concentrated shear and plastic deformation. In addition, annihilation of dislocations will result in reduced flow stress when compared to simulations associated with transport of one signed dislocations. This is because in the current set-up for opposite signed dislocations, they have been arranged to be on the same slip plane, thereby ensuring their annihilation. This reduces the elastic interactions of the dislocation field on the slip pane, resulting in more slip. A direct comparison of the flow stress of simulations featuring only positive dislocations and the mixed dislocations in Figure 6.3.16 and Figure 6.3.17 show clearly the further softening effects caused the negative dislocation density.

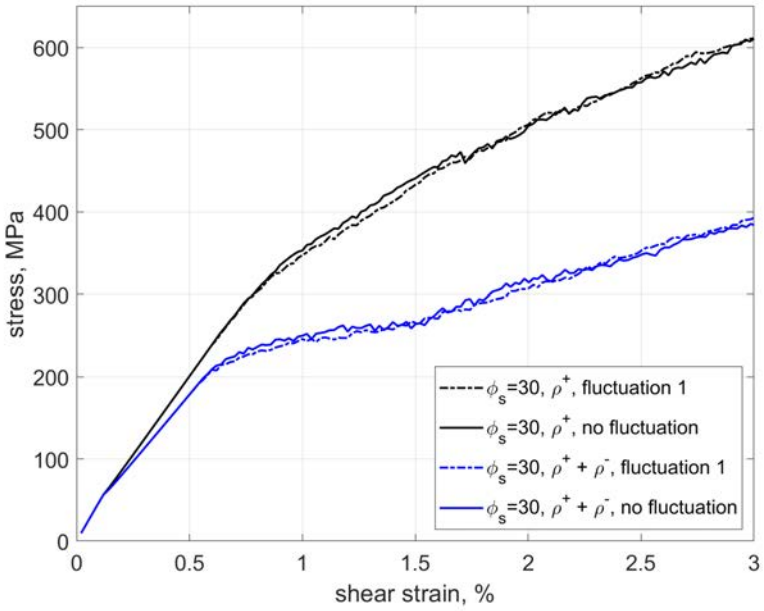

Figure 6.3.16: Flow stress comparison with and without negative dislocation density for $\Phi_S = 0.30$

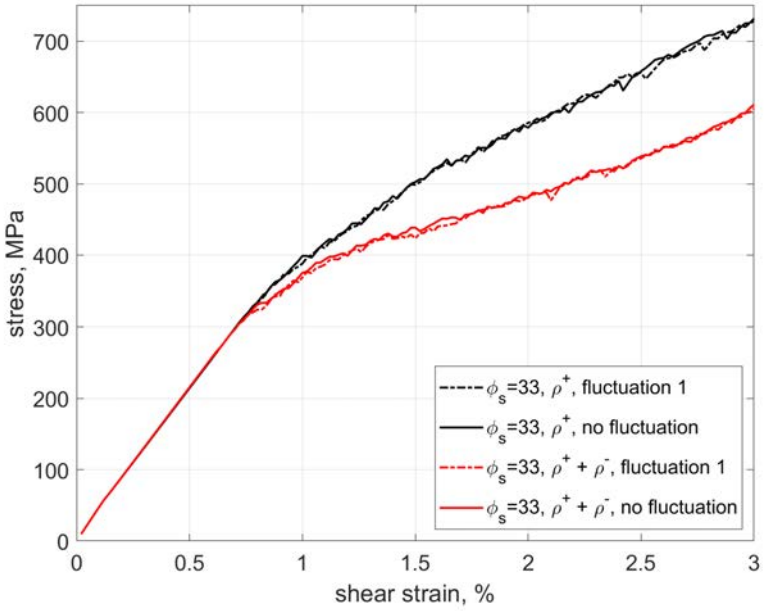

Figure 6.3.17: Flow stress comparison with and without negative dislocation density for $\Phi_S = 0.33$

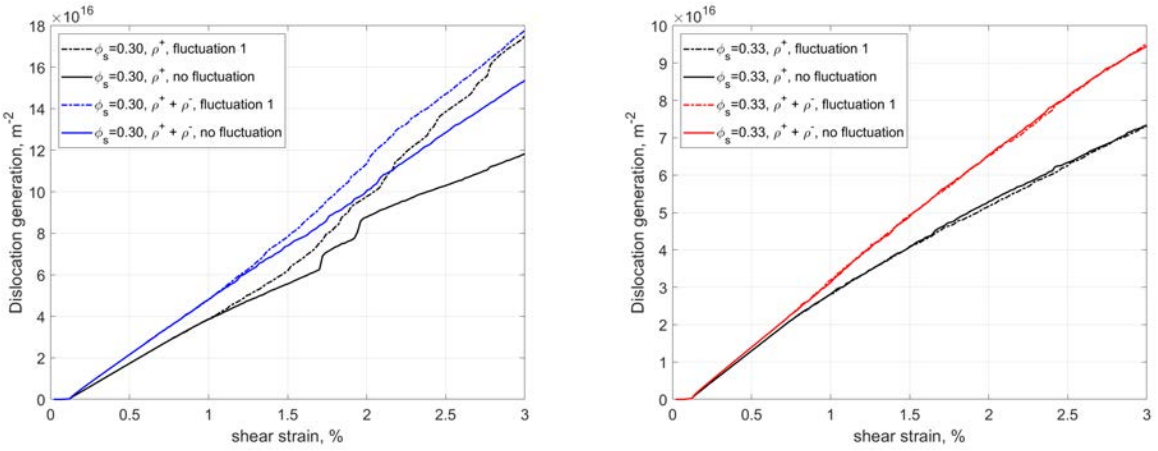

(a) Dislocation generation for $\Phi_S = 30\%$ (b) Dislocation generation for $\Phi_S = 33\%$

Figure 6.3.18: Dislocation density generation history for positive and mixed dislocation density simulations

The number of dislocation sources was the same throughout the simulations but the simulations with only positive sources saw less dislocation generation, see Figure 6.3.18. The location of the dislocation sources relative to the γ' dispersion has influenced the total number of dislocations generated. Figure 6.3.18 shows that dislocations start generating at much lower strain (and corresponding stress) than the macro-yield was observed. The flow stress curves for $\Phi_S = 0.30$ in Figure 6.3.16 display a micro-yield corresponding with the initial generation of dislocations. The dislocations must generate then immediately pile-up at the γ' particles until there was sufficient stress at the tip of the pile-up to shear the 100 nm particles. The yield observed in the flow stress is due to the shearing of the γ' particles not just the generation of dislocations.

6.4 Development of slip bands with stochastic stress contributions

This section focuses on the evolution of dislocation slip bands. The secondary focus is if the stochastic stress field approach has an influence on dislocation patterning which existing

stochastic dislocation dynamics approaches have investigated [54,65,69]. The source activation and evolution of dislocation density is dependant on the strain and stress distribution within the domain. Sources were activated with a randomly assigned nucleation stress from a specified range of nucleation stress values. The distribution of the F_{12}^p component of plastic deformation was plotted at 1% strain increments for the simulations in Figure 6.4.1 and Figure 6.4.2. Both show the formation of heterogeneous slip due to the positioning of γ' particles relative to dislocation sources. Dislocation movement was initially stopped by γ' particles until the stress on the density was sufficient to overcome the cutting stress to shear the particle.

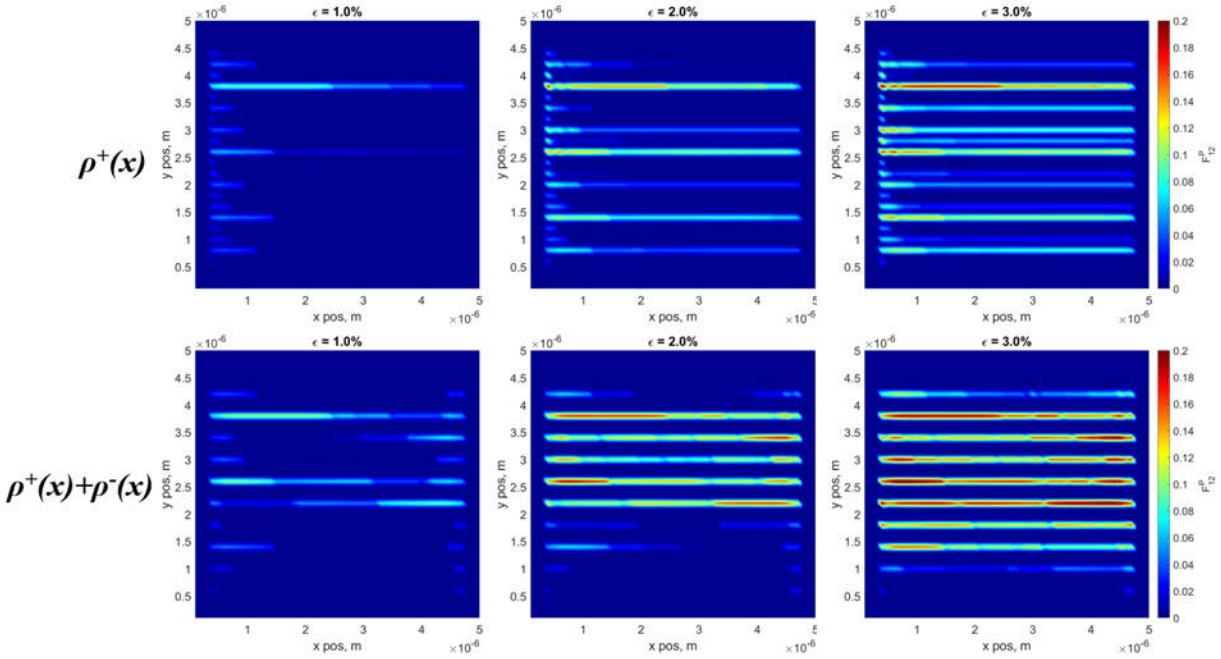

Figure 6.4.1: Plastic deformation gradient, F_{12}^p, maps at shear strain increments of 1% for 'Fluctuation 1' in $\Phi_S = 0.30$, $\rho^+(x)$ and $\rho^+(x) + \rho^-(x)$.

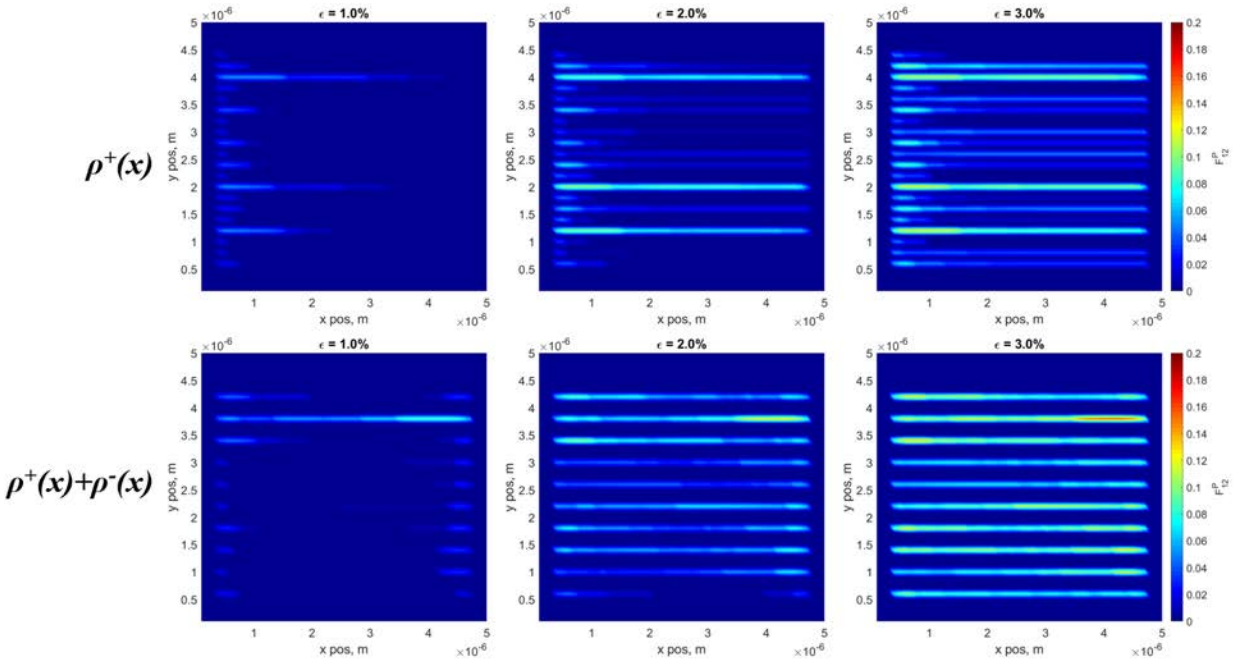

Figure 6.4.2: Plastic deformation gradient, F^p_{11}, maps at shear strain increments of 1% for 'Fluctuation 1' in $\Phi_S = 0.33$, $\rho^+(x)$ and $\rho^+(x) + \rho^-(x)$.

Due to the higher concentration of dislocations on slip planes from positive and negative sources these instances display shear at $\epsilon = 3\%$ across the full domain length whereas for the positive source simulations shear has not occurred across the full domain for all sources. Figure 6.4.1 shows development of more slip bands at 1% than Figure 6.4.2, the lower volume fraction of γ' particles more easily sheared increasing shear events and lowering the yield stress.

The dislocation fluctuation term introduced a random element to each simulation which changes the velocity fields and resulting evolution of the densities. The different stress fluctuation runs were expected to evolve into different distributions. The dislocation distributions for the simulations with the stress fluctuation term are compared to identify differences in dislocation arrangement and plastic deformation. The dislocation density maps presented correspond to the flow stress graphs in Section 6.3.

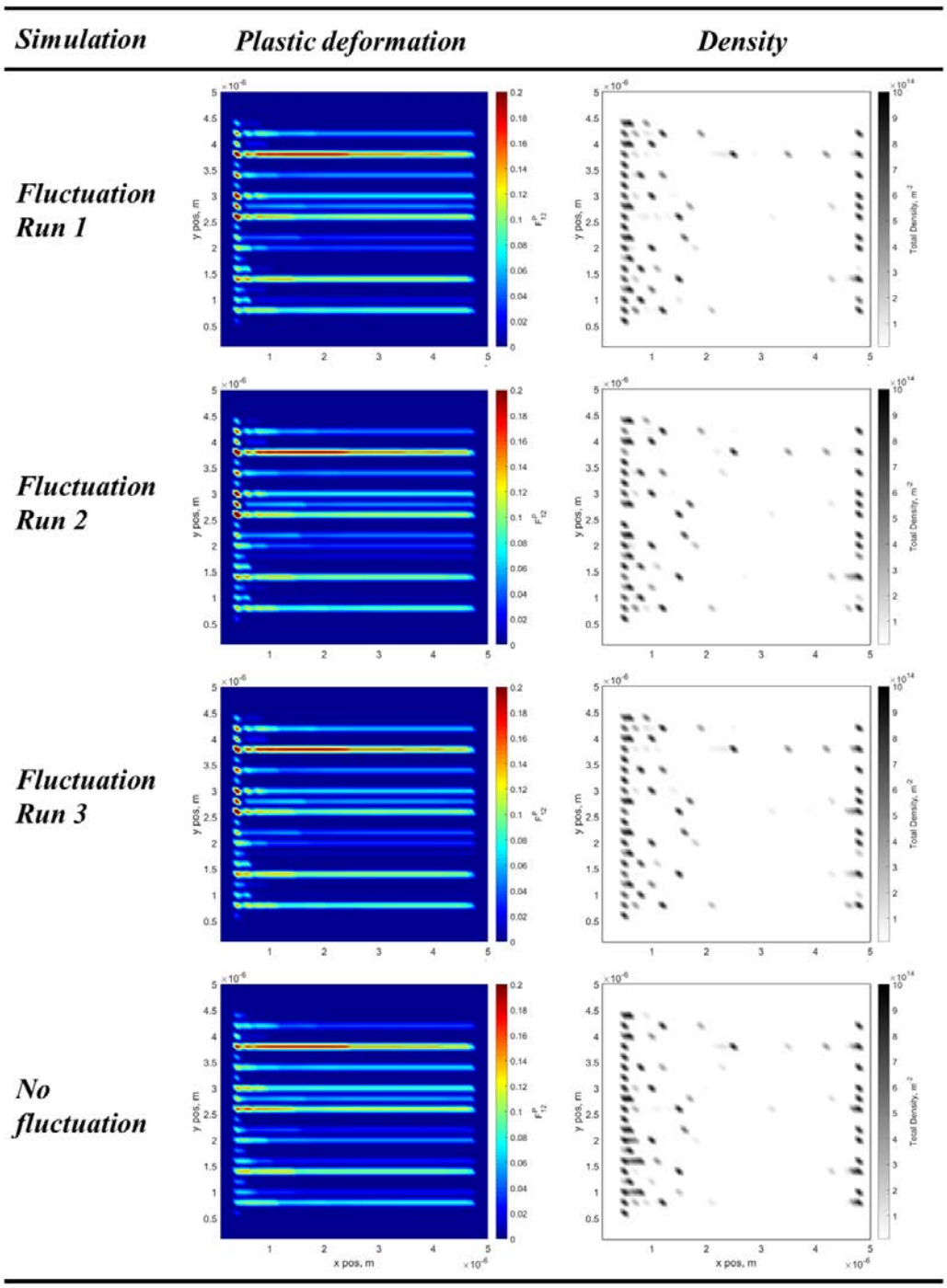

Figure 6.4.3: Plastic deformation gradient component, F_{12}^{p}, and dislocation density, ρ^{tot}, comparison of all simulations for $\Phi_s = 0.30$ dispersion. Each distribution map captured at $\epsilon = 3\%$. Only positive dislocations

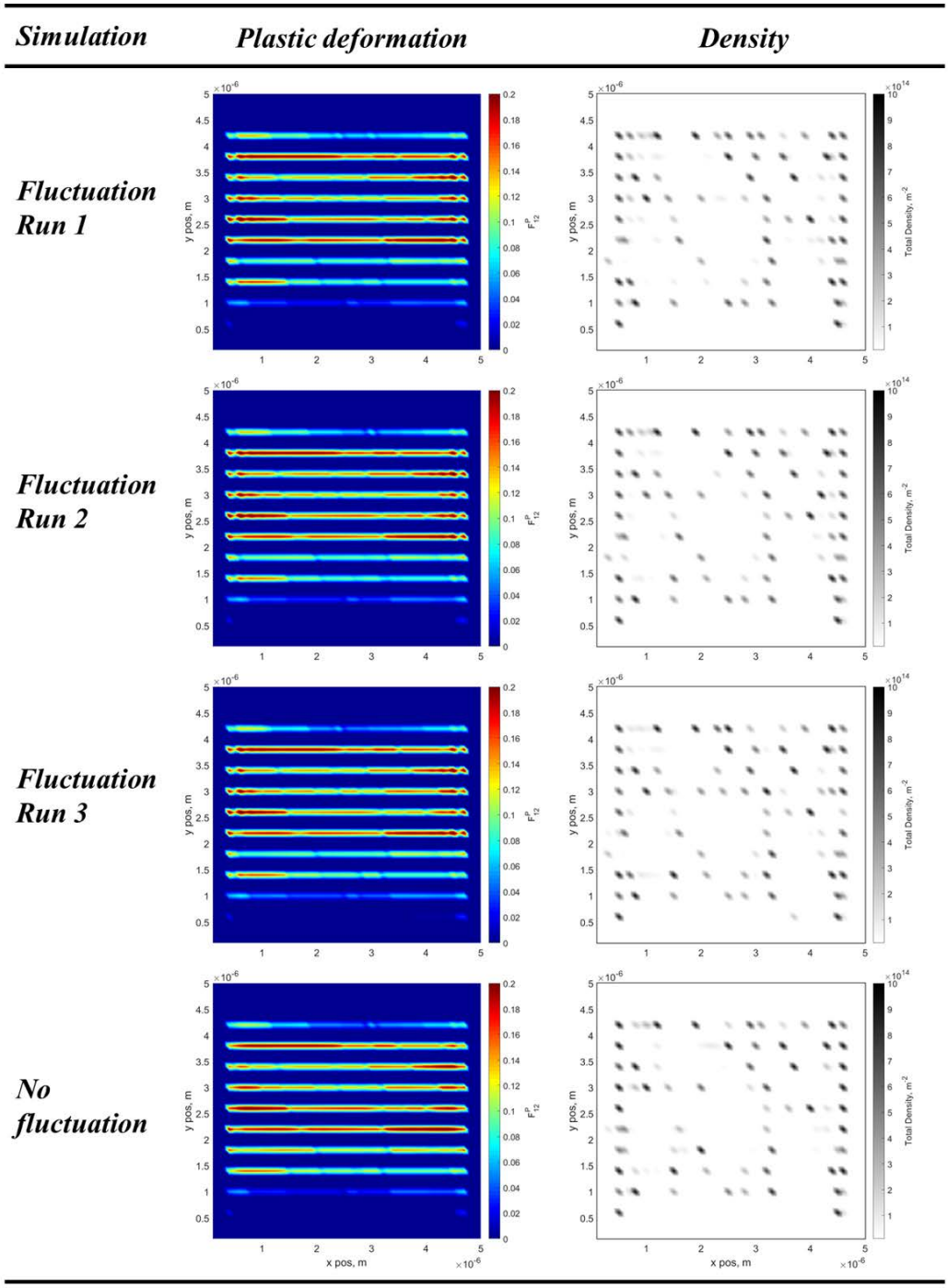

Figure 6.4.4: Plastic deformation gradient component, F_{12}^{p}, and dislocation density, ρ^{tot}, comparison of all simulations for $\Phi_s = 0.30$ microstructure. Each distribution map captured at $\epsilon = 3\%$. Positive and negative dislocations

Figure 6.4.3 and Figure 6.4.4 compare the deformation gradient (indicating shear) and the dislocation fields at $\epsilon = 3\%$ for the positive dislocation and mixed dislocation simulations respectively. Both display little difference between their distributions of F_{12}^{p} and ρ^{tot} with the stress fluctuation term. Slip bands form by shearing the precipitate particles, with the concentrations of dislocations at the boundaries. The local stress fluctuations did not change the slip band formation in Figure 6.4.3, much more difference in slip band formation comes from changes in the heterogeneous particle distribution. Minor differences in dislocation distributions and stress fields due to the $\underline{\boldsymbol{f}}^{fluc}$ term, dislocations concentrated at the boundaries and by some particles in the domain. These dislocation density field plots highlight the immobile dislocation populations piled-up at γ' particles and the boundary. The corresponding y position in the F_{12}^{p} map not showing any shearing across the domain, for example at $y = 1\,\mu m$ for all maps in Figure 6.4.4.

6.5 Discussion

The governing equation for transport of dislocations requires specification of the dislocation velocity, which in turn depends on the local force acting on the dislocation field. In classical FDM, this force is the superposition of contributions coming from the applied load as well as neighbouring dislocation field. However, such formulations do not account for fluctuations in the dislocation force arising from different arrangements of individual dislocations, which are not resolved in a continuum theory. To asses the impact of these fluctuations, DDD simulations were carried out that determined the the fluctuation force $\underline{\boldsymbol{f}}^{fluc}$. The force fluctuations $\underline{\boldsymbol{f}}^{fluc}$ for each density was characterised by tracking internal forces from 500 discrete dislocation dynamics simulations. The fluctuation of local stress acting on the dislocations formed normal Gaussian distributions which were scalable with the density, plotted in Figure 6.2.8. The force associated with the stress functions was calculated using the Peach-Koehler equation, which was then used to calculate the dislocation velocities required

to solve the transport equation.

The stochastic term had little effect on the flow stress relative to simulations without the stochastic term. The average absolute flow stress fluctuation for positive dislocations were 5.23 MPa for the $\Phi_s = 0.30$ distribution, and 3.46 MPa for the the $\Phi_s = 0.33$ distribution. These minor average deviations did not appear to increase with the applied strain and growing dislocation population. Negative dislocations were introduced into the stochastic FDM with the annihilation rate, define by Equation (5.4.7), for when opposite sign dislocation densities interacted. Negative dislocation sources increased the dislocation population and the concentration of shear. This reduced the average domain stress and linear hardening effects due to the closed boundaries observed when only modelling positive dislocations. The fluctuating stress term had little effect on the plastic response of the simulated domain up to 3% applied strain, even with the addition of the negative dislocations.

These simulations also revealed the relationship between dislocation-microstructure interactions and the influence it has on yield stress. Although dislocations began generating at about $\epsilon = 0.11\%$, seen in Figure 6.3.18, little yield was observed until the stress was sufficient to begin shearing the γ' particles across the full length of the domain at approximately $\epsilon = 1.0\%$. A 3% increase in secondary γ' particle volume fraction saw yield at approximately 100 MPa higher in the mixed dislocation simulations. Comparing the deformation gradient maps at $\epsilon = 1\%$ in Figure 6.4.1 and Figure 6.4.2, there was much less shear due to the increased cutting stress required when the dislocation density stopped at each particle. The simulation set-up confining dislocations to a single slip system limited the spread of dislocations to neighbouring slip systems, although the dislocation climb term was accounted by Equation (3.4.4) no broadening of the slip bands was observed making glide the dominant form of dislocation transport.

The finer details of dislocation patterning alternative stochastic models attempt to recreate are too small resolution to capture in our continuum model within the current scaling of the dislocation density grid. The main finding of this chapter is that for single slip, the flow stress fluctuations are small in comparison to the flow stress. Consequently it was decided to omit these stochastic stress field contributions for the evolution of the field dislocation mechanics model in subsequent fatigue simulations to focus on the influence of the microstructure.

Chapter 7

Modelling microstructure influence on fatigue behaviour using FDM

7.1 Introduction

The ordered $L1_2$ γ' phase in Nickel-based superalloys plays an important role in determining their high temperature properties. In particular, experimental observations indicate that increasing γ' volume fraction has a beneficial impact on fatigue life [34, 92]. Microstructure characterisation of these alloys have shown the development of dislocation slip bands during low cycle fatigue conditions, mediated by the transport of coupled dislocations [16, 93, 94]. It was demonstrated in the previous chapter, that variations in the γ' dispersion induce scatter in the flow stress response. This casual effect of microstructure on alloy properties, will play an equally important role under low cycle fatigue conditions such as those experienced by a turbine disc. In such components variations in the thermal fields during forging operations will induce location specific variations in the γ' dispersion. Figure 4.4 shows SEM images of γ' dispersions subject to different thermal histories with a turbine disc. Understanding the effect of these precipitate variations on the LCF behaviour of these alloys is important, since certain precipitate distributions may promote localisation of deformation that lead to

nucleation of cracks.

Typical grain sizes of disc alloys are in the range of 4 - 12 μm [95]. Based on these observations a computational domain size of $(5\,\mu\text{m})^2$ was used to represent a single grain. A number of instances of these domain were set-up based on different γ' dispersions. Cyclic loading simulations have been carried out at 700°C, 750°C and 800°C. The γ' dispersions used in these models are based on 50 hour exposures of the as-received material as reported by Schultz et al [85] and Anderson et al. [14]. The dispersion parameters used are listed in Table 4.1. The γ' dispersions used in the simulations are shown in Figure 4.4.2. As in the previous chapter, the cyclic flow stress is calculated through homogenisation of microstress field. From these, the plastic strain range, $\Delta\epsilon_p$, and stress range, $\Delta\sigma$, were extracted for each fatigue loading cycle, these dimensions are indicated in Figure 7.1.1.

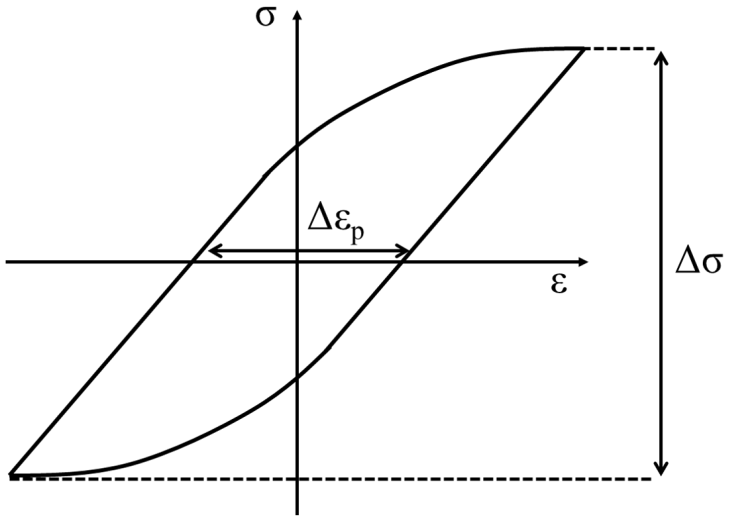

Figure 7.1.1: Stress range, $\Delta\sigma$, and plastic strain range, $\Delta\epsilon_p$, dimensions on a fatigue stress-strain plot

7.2 Fatigue simulation set-up

A square simulation domain of $5\,\mu$m length was created with a mesh of grid division size dx =100 nm. A shear displacement boundary condition was imposed on the top face of the computational domain while keeping the bottom face pinned, see Figure 7.2.1. Switching to a reverse loading condition was achieved by changing the direction of the imposed surface velocity on the top face of the domain. The resulting total strain time evolution created by the periodic velocity reversal on the top of the domain is shown in Figure 7.2.2. Dislocation sources capable of generating positive and negative dislocation lines were placed at regular intervals along the boundaries of the computational domain. These are schematically shown in Figure 7.2.1. It is recognised that this arrangement of positive and negative dislocation sources is artificial and in real crystals these will be randomly distributed along grain boundaries. However, these aligned opposite sign sources were chosen to investigate the impact of annihilation events on the cyclic stress-strain curves. These constant source placements were chosen over a random source distribution to focus on the influence of the changes in γ' distribution on the fatigue response.

The FDM requires a very small time step, 1×10^{-8}s, to capture dislocation-microstructure interactions for the domain size simulated, thus to simulate a suitable number of loading cycles a high loading frequency was used for strain controlled loading. Figure 7.2.2 shows the loading amplitudes applied. Normally the loading frequency for LCF tests is around 1-2 Hz for physical testing [16, 96]. Low cycle fatigue experiments test between $\Delta\epsilon = 1\%$ to $\Delta\epsilon = 2\%$ [94,96]. The predictions made in this chapter are over the strain ranges $\Delta\epsilon = 1.2\%$ to $\Delta\epsilon = 1.6\%$ chosen as they both surpass the yield stress creating the plastic deformation observed in LCF tests.

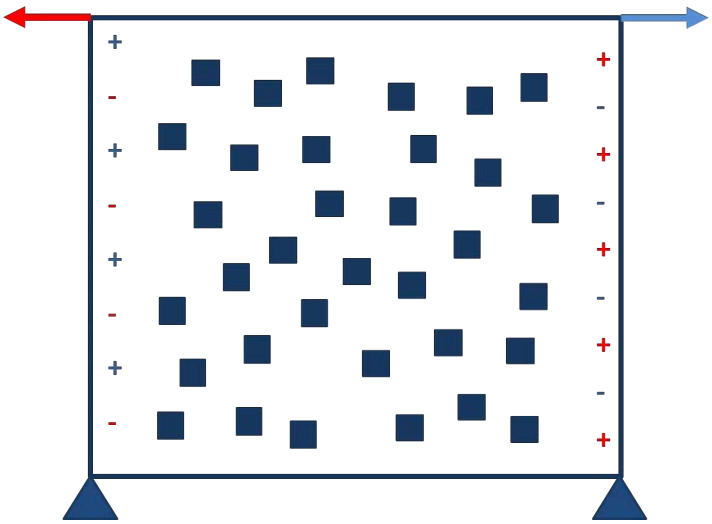

Figure 7.2.1: Sketch of domain source set-up, blue indicates sources that activate on a forward load (right) and red indicate sources that activate on a reverse load (left)

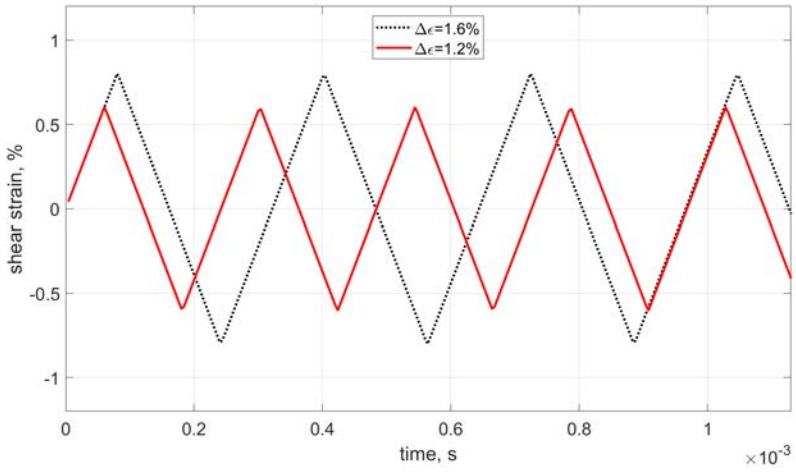

Figure 7.2.2: Strain controlled fatigue loading profiles

7.3 Strain-controlled cyclic flow stress behaviour

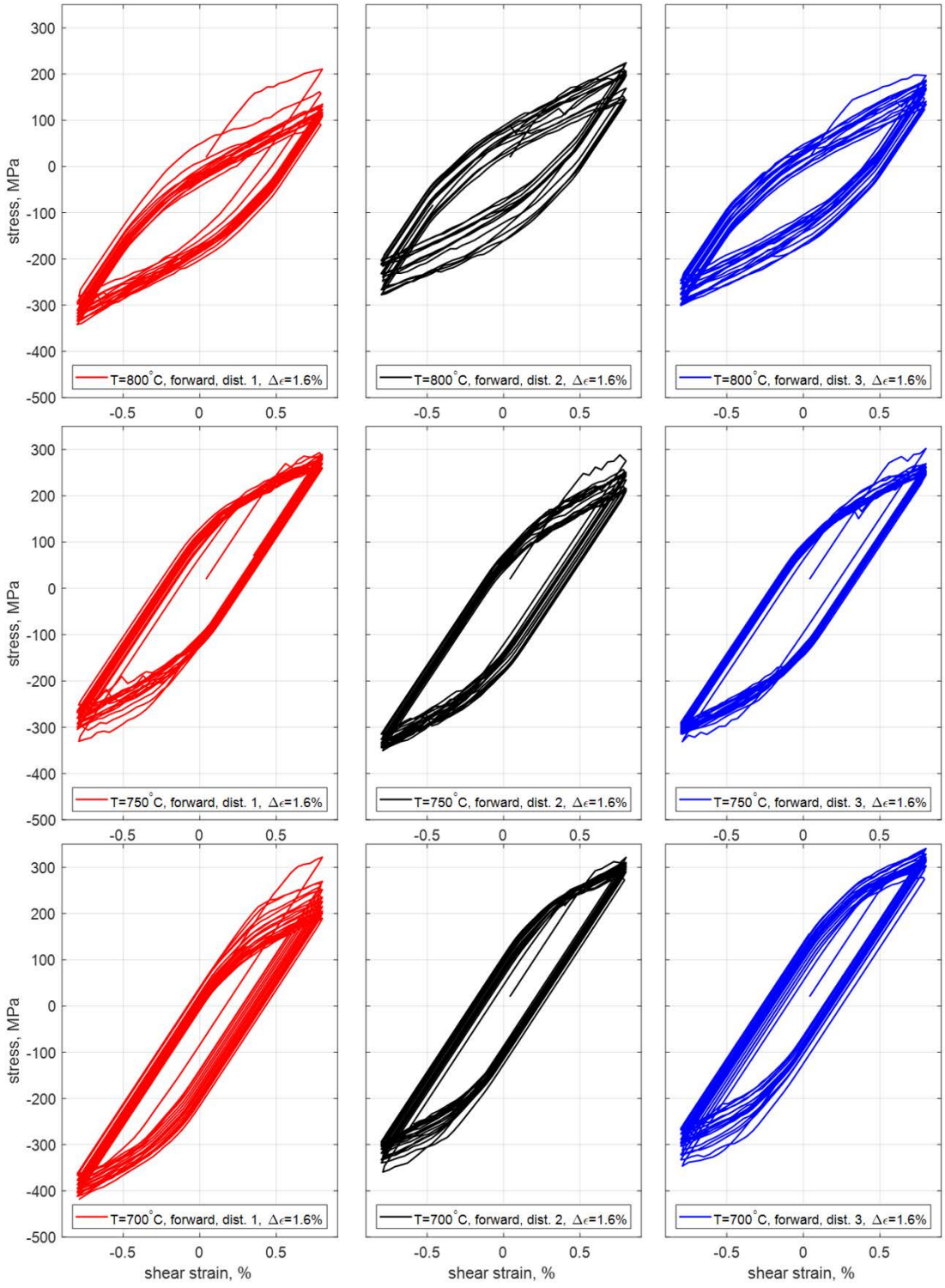

Figure 7.3.1: Stress-strain plots for the three distributions for all temperatures tested at $\Delta\epsilon = 1.6\%$

The cyclic stress-strain model predictions for $\Delta\epsilon = 1.6\%$ are shown in Figure 7.3.1. From these simulations it can be seen that the three γ' distributions result in variations in the predicted cyclic curves at all temperatures. However, the largest differences in the predicted stress-strain curves are at 800°C. At this temperature, a significant amount of strain softening is predicted within the first 2 cycles. The absence of tertiary particles at 800°C resulted in increased dislocation mobility leading to strain softening behaviour. As the dislocation slip band stabilise, so does the predicted cyclic response. The predicted scatter in the cyclic loads at 700°C and 750°C is not as wide as those observed at 800°C. The peak stresses for these cases are larger, which reflects the strengthening effect of tertiary γ' precipitates. Predicted fatigue curves for the applied strain range $\Delta\epsilon = 1.2\%$ are shown in Figure 7.3.2. Once again the largest scatter in the predicted cyclic loads is at 800°. Distribution 2 at 800°C exhibits some initial softening but then sees a slight ratcheting of the average stress back up rather than downwards. Distribution 3 sees the largest drop in the maximum stress after the first cycle. As expected, the width of the hysteresis loops decreases with decreasing temperature, with the peak stresses being largest at 700°C. This is attributed to a larger γ' volume fraction at 700-750°C compared to 800°C as well as the presence of tertiary γ' at the lower temperatures. As already discussed in the previous chapter, the γ' cutting stress scales with precipitate volume fraction, so that transmission of the slip band across a γ/γ' interface is more difficult at lower temperatures.

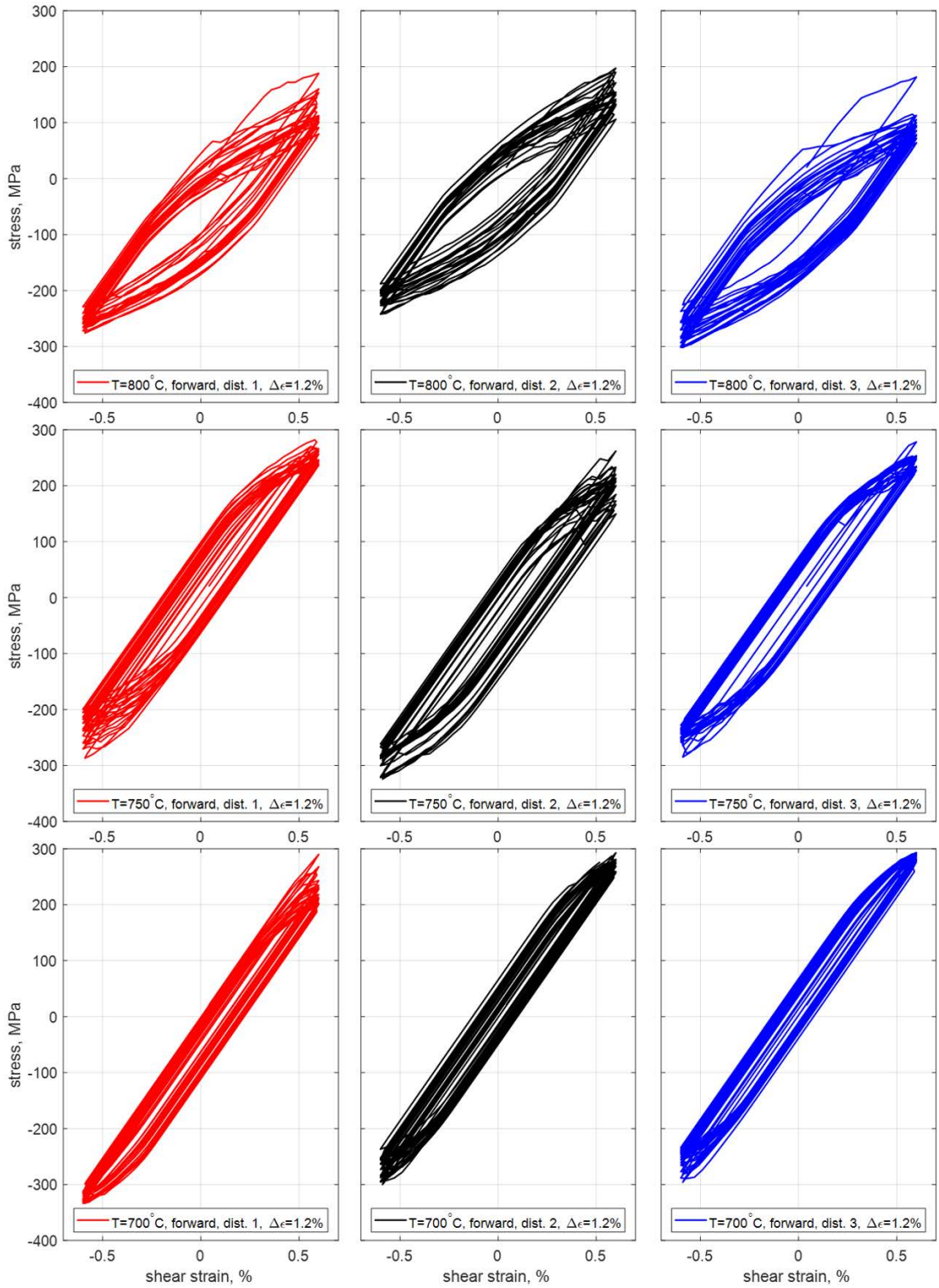

Figure 7.3.2: Stress-strain plots for the three distributions for all temperatures tested at $\Delta\epsilon = 1.2\%$

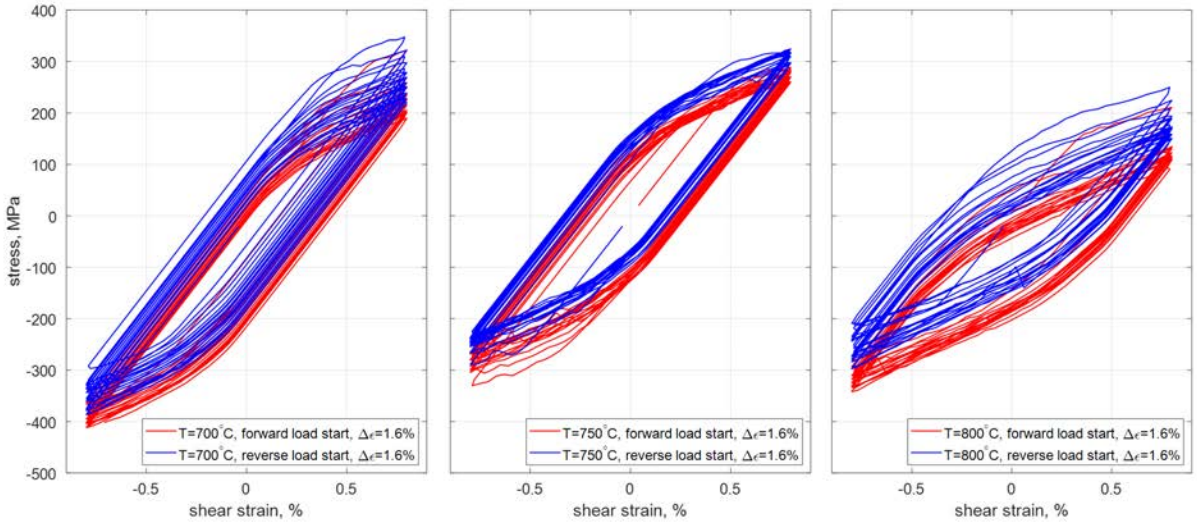

Figure 7.3.3: Stress-strain plots comparing forward and reverse starting load direction for distribution 1 for all temperatures tested at $\Delta\epsilon = 1.6\%$

Simulations were also performed with a negative imposed strain rate, so that the cyclic loading goes into compression on initial loading. Comparison of the forward and reverse simulations for distribution 1 at each temperature for $\Delta\epsilon = 1.6\%$ are shown in Figure 7.3.3. With an initial compressive loading direction expected a reverse shakedown to occur but a similar small amount of ratchetting of the negative stress occurs in Figure 7.3.3. The similarities in response can be attributed to spacing between particles is the same, similar size shear events are possible but the particle field is approached by dislocations generated from the same sources in a different order.

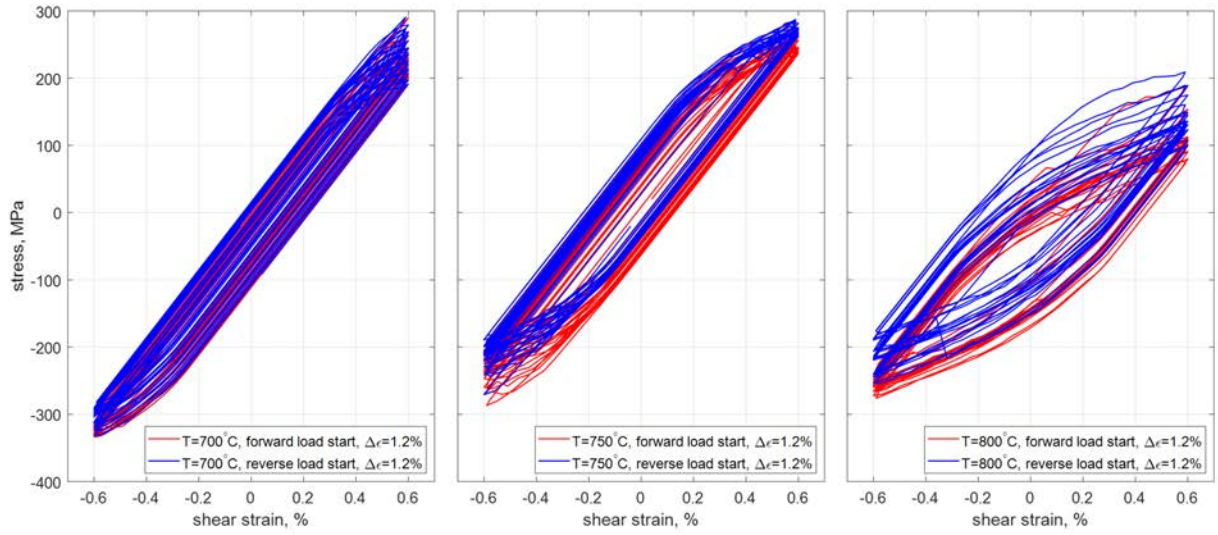

Figure 7.3.4: Stress-strain plots comparing forward and reverse starting load direction for distribution 1 for all temperatures tested at $\Delta\epsilon = 1.2\%$

Similarly, the forward and reverse loading simulations for $\Delta\epsilon = 1.2\%$ are presented in Figure 7.3.4. At 750°C the cyclic curves for forward and reverse loading overlap with a slight ratchetting of the stress due to softening as dislocations were generated with each cycle. Both forward and reverse loading simulation demonstrate increased activity from negative dislocations sources. The forward and reverse fatigue loops for distribution 1 at 700°C show a lot of overlap in Figure 7.3.4, there was not much yield for the stress reached with the strain range in these distributions, the distributions had a very elastic response.

7.4 Peak stresses and stress range

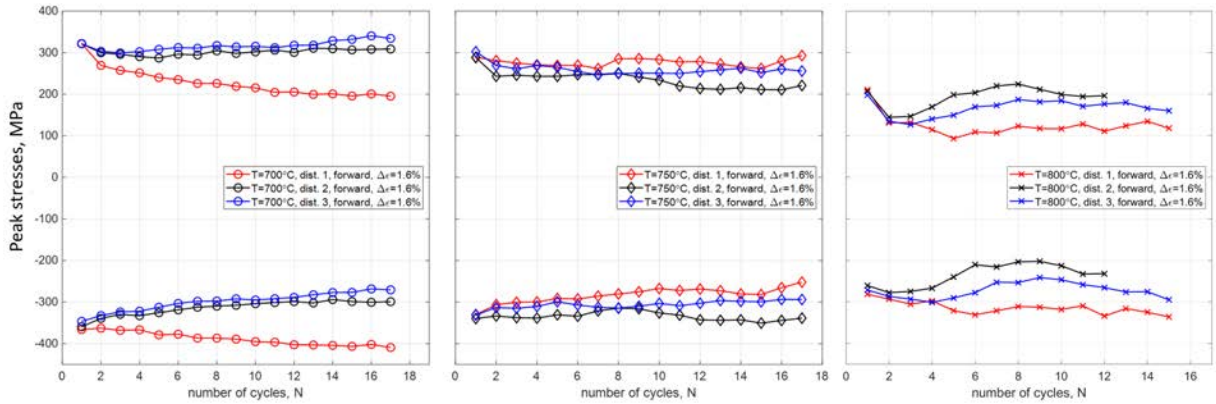

Figure 7.4.1: Peak stresses per cycle comparing for all temperatures and distributions at $\Delta\epsilon = 1.6\%$

The peak stresses as a function of the number of cycles for $\Delta\epsilon = 1.6\%$ are shown in Figure 7.4.1. The influence of the γ' dispersion on the evolution the cyclic curves can clearly be seen. Model predictions for all cases show kinematic hardening behaviour, where the stress range (as defined by the difference in the peak stresses) moves progressively into compression or tension. These kinematic effects are associated with the development of internal stresses that result in the translation of the loading yield surface. This behaviour gives rise to a Bauschinger effect. The peak stress evolution for $\Delta\epsilon = 1.2\%$ are shown in Figure 7.4.2. This cyclic drift of the hysteresis loops is consistent for the distributions for both applied strain ranges. At 700°C the differences in peak stresses are very similar to those observed for the larger strain range in Figure 7.4.1. This shows that slip development and imbalances in shear events is consistent for the γ' distributions under different applied strain ranges.

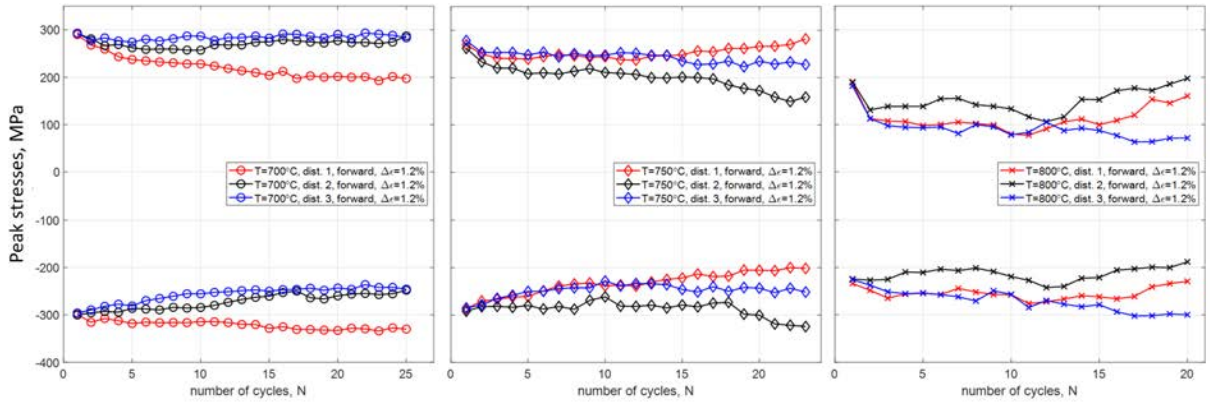

Figure 7.4.2: Peak stresses per cycle comparing for all temperatures and distributions at $\Delta\epsilon = 1.2\%$

It will prove useful to work with the average stress range response associated with all three distributions. This is illustrated in Figure 7.4.3, where model predictions of the stress range for all three distributions at 700°C with $\Delta\epsilon = 1.2\%$ are shown as well as the corresponding mean stress range (together with the maximum and minimum values).

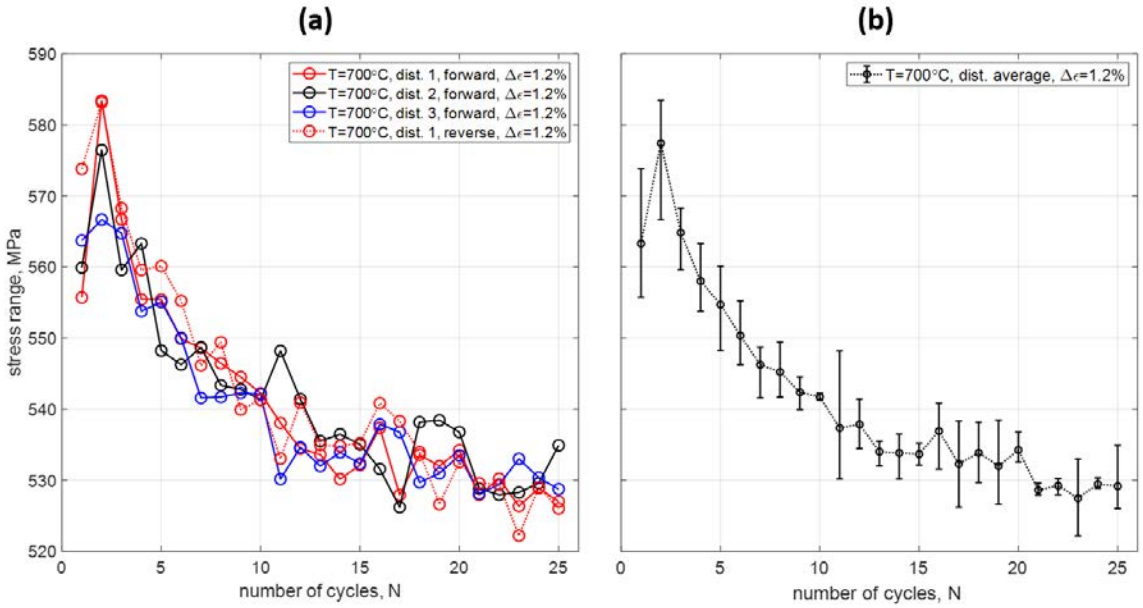

Figure 7.4.3: (a) Individual stress range plots for distributions at 700°C for $\Delta\epsilon = 1.2\%$. (b) Mean cyclic stress range for all distributions at 700°C for $\Delta\epsilon = 1.2\%$

Comparison of the averaged stress range evolution for both applied strain ranges and temperatures investigated are summarised in Figure 7.4.4. The model simulations indicate that slip band interactions with γ' precipitate result in strain softening, characterised by a drop in the stress range. The stress range values for the distributions at 700°C displayed the least scatter, having the largest secondary and tertiary particle volume fraction increases the stress required for dislocation shear the γ' particles slowing the dislocations. There is a smaller mean free path for the mobile dislocations in these distributions reducing the potential for large shear events and the amount of variation in stress range per loading cycle. At 700°C for $\Delta\epsilon = 1.2\%$ displayed an initial increase in the stress range for the second cycle, see Figure 7.4.4, rather than the drop displayed at all other temperatures, after this it trends down toward 530 MPa. The change in stress range per cycle decreases for the 700°C and 750°C distributions, an indication of increased plastic deformation and softening. The results at 750°C overall have a smaller stress range than 700°C showing the impact of the reduced volume fraction of secondary and tertiary γ' particles on fatigue behaviour. For the smaller strain range more cycles were completed within the same simulation time, which gave more of an indication as to the long term trend of the fatigue behaviour.

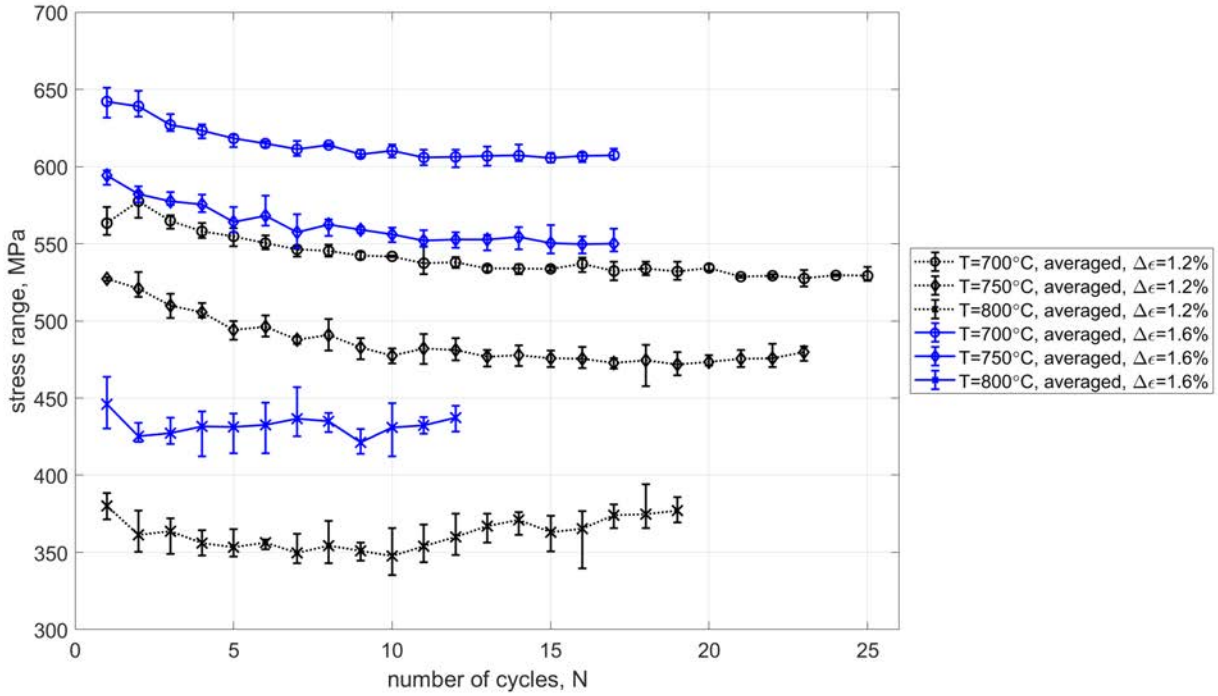

Figure 7.4.4: Comparison of averaged stress range per cycle for distributions at all temperatures for $\Delta\epsilon = 1.2\%$ and $\Delta\epsilon = 1.6\%$

Both of the averaged stress ranges at 800°C for $\Delta\epsilon_p = 1.6\%$ and $\Delta\epsilon_p = 1.2\%$ in Figure 7.4.4 display an initial softening of the stress range and later begins to increase back to the stress range of the first cycle. This is likely due to kinematic hardening from the increased dislocation density in later cycles, the presence of more dislocations and the influence of their increased dislocation stress field contributions reducing the amount of shear events. Due to the lack of tertiary γ' particles the dislocations can move much more freely in these unimodal distributions resulting in more plastic deformation and a much lower average stress range in comparison to the lower temperature distributions.

7.5 Influence of γ' on plastic strain evolution

Using the same averaging method on the stress range for distribution behaviour at each temperature, the averaged cyclic hardening/softening curves for the plastic strain range were plotted together for both applied strain ranges in Figure 7.5.1.

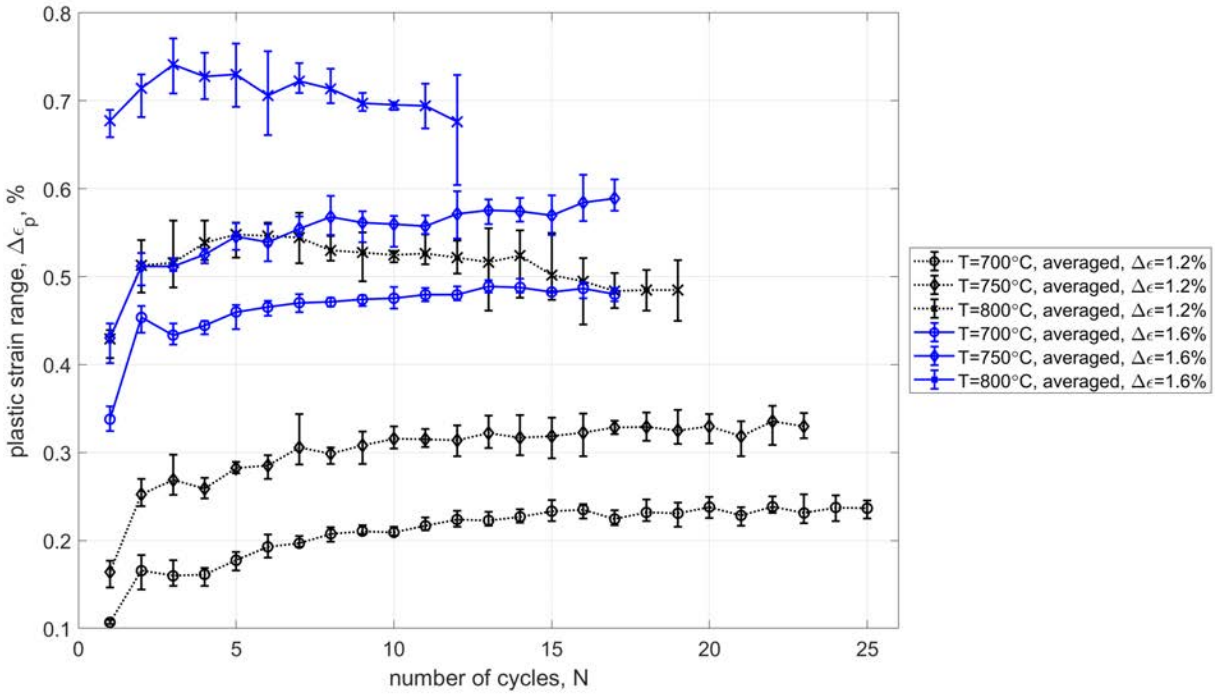

Figure 7.5.1: Comparison of averaged plastic strain range per cycle for all distributions at temperatures for $\Delta\epsilon = 1.2\%$ (black) and $\Delta\epsilon = 1.6\%$ (blue)

At both applied strain ranges 700°C had the smallest plastic strain range and variation per cycle. The average absolute difference in strain range values from the mean at each cycle was 0.02% for $\Delta\epsilon = 1.2\%$ and 0.018% for $\Delta\epsilon = 1.6\%$. Having the hardest overall response of the temperatures is a direct result of the high volume fraction microstructure. For both strain ranges the 750°C plot is closer to the 700°C results than the 800°C results. This will be a result of the higher volume fraction of secondary γ' and presence of tertiary γ' which shortens the mean free path of the dislocations and prevents larger shear events from happening that

create more change in the flow response resulting in an overall harder response of the domain.

Figure 7.5.1 presents an increase in plastic strain range at 750°C that begins to plateau with small increments increasing per cycle. At 750°C the increase from cycle 1 to cycle 2 for $\Delta\epsilon = 1.6\%$ is a 0.008% less than that experienced at $\Delta\epsilon = 1.2\%$. This implies slightly more shear events occurred from cycle 1 to cycle 2 in the smaller strain range, but it would be expected that the larger applied strain would induce more stress and more slip events. The 700°C and 750°C distributions both show an increase in plastic strain range indicating softening towards a constant value as shown for to the larger strain range in Figure 7.5.1. The 700°C and 750°C distributions display an increase in the plastic strain range indicating softening of the domain tending towards a plateau.

At 800°C the initial increase in the plastic strain range is significantly smaller by 0.048% smaller for $\Delta\epsilon = 1.6\%$ not expected as the domain experiences larger stresses under the large fatigue strain range. In Figure 7.5.1 the 800°C distributions show an initial softening through an increase of the plastic strain range that then trends back down towards the plastic strain range of the first cycle. At $\Delta\epsilon = 1.6\%$ the average plastic strain range of the cycle 12 is the same as the starting cycle, cycle 12 also has the largest variation in values across the distributions. Smaller numbers of cycles were simulated at 800°C, these results show a consistent trend of initial softening followed hardening indicated by decrease in plastic strain range and corresponding increase in stress range in Figure 7.4.4. These simulations completed less cycles than initially expected for the maximum allowed time frame. The dislocation field had increased mobility in the highest temperature distribution the FDM calculations required more iterations to converge the solutions for the dislocation evolution equation.

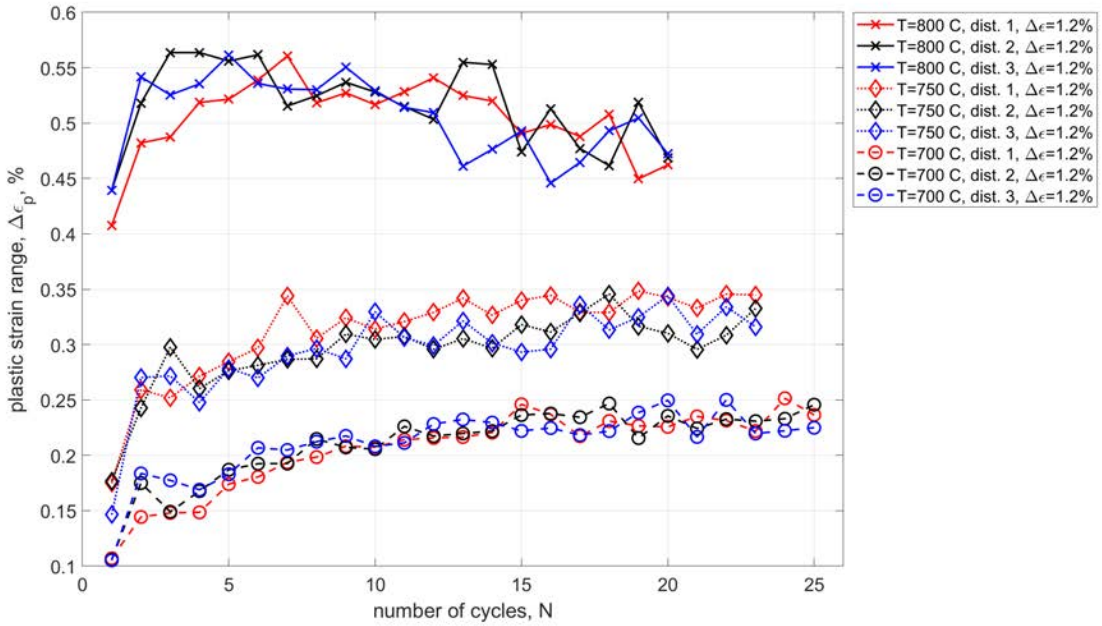

Figure 7.5.2: Comparison of plastic strain range per cycle by distribution at all temperatures for $\Delta\epsilon = 1.2\%$ fatigue

A closer look at the plastic strain range results for the individual distributions at all temperatures for $\Delta\epsilon = 1.2\%$ reveals in more detail how the different precipitate distributions differ at each temperature in Figure 7.5.2. The distributions follow similar trajectories at each temperature but the influence of particle position clearly impacts the shear events and the individual flow stress behaviour. At a given temperature the plastic strain range evolution is not consistently lower for one distribution over another, for example at 700°C distribution 3 has the largest plastic strain range for the first 10 cycles then begins to alternate between having the highest and lowest strain range for following cycles.

7.6 Discussion

Full field simulations within a single grain under uniaxial cyclic loading conditions have been carried out at three temperatures between 700-800°C and two strain range amplitudes. The stress-strain response for the single grain was calculated through homogenisation of the microscale mechanical fields. The influence of γ' variations on the predicted stress-strain loops was investigated by running simulations on three different instances of the precipitate dispersion at each temperature.

It was found that on initial loading, activation of the Frank-Read sources occurred at stresses (60 MPa) well below the yield stress of the grain, which was found to be of the order of 3-4 times greater than that required to activate sources. This was shown to be associated with dislocation-precipitate interactions, where propagation of the dislocated field is limited by their intersection with the γ' particles. At this point the local stress state ahead of the dislocation pile up is not sufficient to overcome the APB energy required to shear the precipitate and results in the formation a dislocation pile-up. The accumulated plastic strain is not sufficient to deviate the material response from elastic behaviour. Continual loading will in the dislocation density along the pile up, thereby increasing the stress on the dislocations at the particle interface. This continues until the stress is sufficient to cut the particle, at which point, the dislocation field continues to propagate and as it does so the stress on the leading dislocation decreases. Depending on the size of the next particle intercepted by the developing slip band, the dislocation field will become pinned or continue to move across the grain. These interactions result in complex variations in the slip band which are dependent on the details of the γ' dispersions. The full field simulations show that scatter of the predicted stress-strain curves of a single grain are due to variations in the slip band evolution which are induced by the details of the precipitate distribution. It has been suggested that the inhomogeneous microstructure may act as local stress concentrators, contributing

to cyclic strain localization [97]. It was found these interactions also resulted in variations in the predicted cyclic loading behaviour when comparing simulations carried out initially under tension or compression. These are referred to as 'forward' and 'reverse' conditions, respectively.

Under the cyclic loading conditions yield due to plastic deformation was observed for both 'forward' and 'reverse' loading directions, this was a result of modified dislocation mobility equations and the inclusion of dislocation sources that activated under the reverse load. The yield due to shearing of γ' for both loading directions resulted in generation of symmetrical fatigue loops when analysing the stress-strain evolution for the domain. Hysteresis behaviour was predicted due to plastic deformation of the shear created by mobile dislocations moving back and forth across the domain shearing the precipitate distributions forming slip bands.

7.6.1 Case 1 - 700°C distributions 1 and 3

From Figure 7.3.1 the difference between the first and last cycles are not completely evident given the slight variations in the flow stress per cycle. A direct comparison of the initial cycle versus the final cycle for distribution 1 and 3 at 700°C for $\Delta\epsilon = 1.2\%$ in Figure 7.6.1 shows clearly how curves have changed throughout the simulations. The last complete cycle for distribution 1 has a minimum stress approximately 50 MPa lower than the minimum stress of the first cycle. Whereas for distribution 3 the compressive peak stress of the final loop sits about 80 MPa higher. Although the drift of the loops is different the loop dimensions are very similar in Figure 7.4.1.

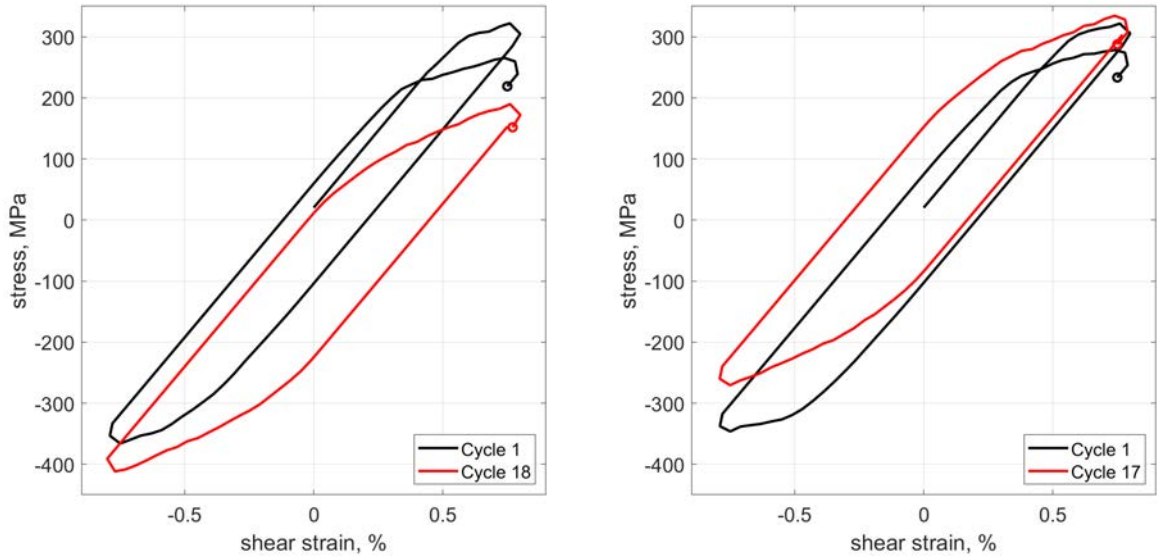

(a) Distribution 1 (b) Distribution 3

Figure 7.6.1: First and last cycle for distributions 1 and 3 at 700°C at strain range $\Delta\epsilon = 1.6\%$

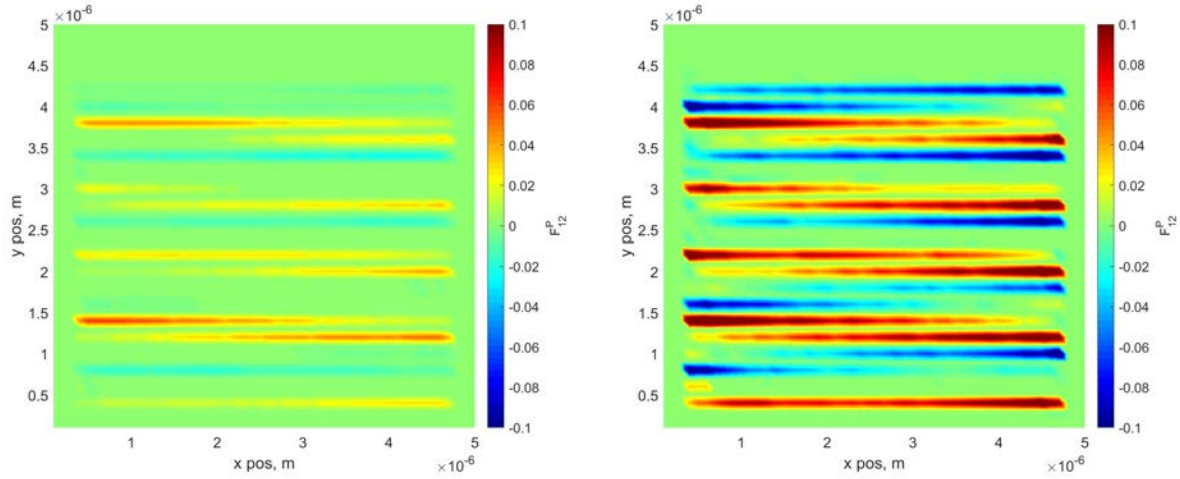

(a) Cycle 1 (b) Cycle 18

Figure 7.6.2: Deformation gradient component, F^p_{12}, for 700°C distribution 1 for strain range $\Delta\epsilon = 1.6\%$

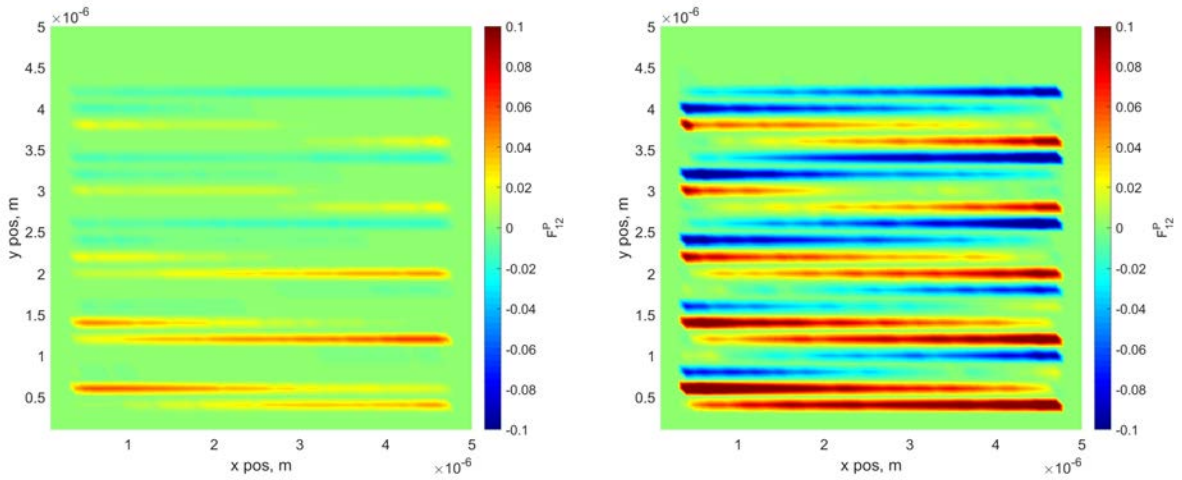

(a) Cycle 1 (b) Cycle 17

Figure 7.6.3: Deformation gradient component, F^p_{12}, for 700°C distribution 3 for strain range $\Delta\epsilon = 1.6\%$

Maps of the plastic deformation gradient component F^P_{12} at the initial and cycles 16/17 are shown in Figure 7.6.2 and Figure 7.6.3 for near the peak forward (initial tensile load) conditions $\epsilon = 0.8\%$. The change in intensity of F^p_{12} on the slip bands is clear between the first and last cycles for both distributions. By the end of the first cycle, these simulations show that not all slip bands have fully propagated across the grain. Figure 7.6.2b and Figure 7.6.3b show the deformation gradient for the last cycle in Figure 7.6.1 look very similar at a first glance, having shear along the same y-positions given both simulations have the same dislocation source positions. There is a slight imbalance in Figure 7.6.2b with more positive deformation gradients than negative, comparatively to Figure 7.6.3b, and more intense positive dislocation density across the full length. Some examples of these differences are seen at the $y = 3.8$, 3.2 and 0.6 μm. As the only difference in these simulation parameters is the distribution of the particles the influence it has on slip events is apparent.

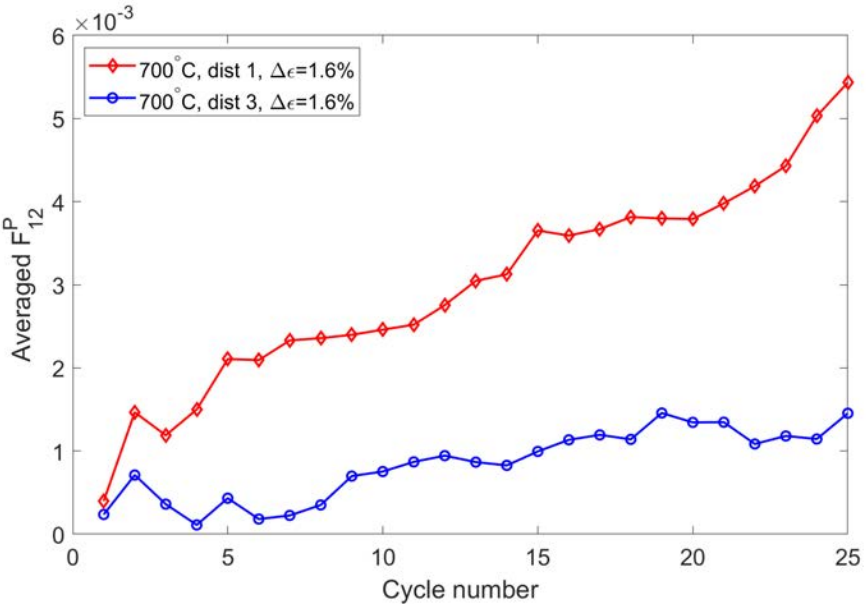

Figure 7.6.4: Average F_{12}^{p} across the whole domain per cycle for distributions 1 and 3 at 700°C for $\Delta\epsilon = 1.6\%$

The average of the total plastic deformation gradient tensor component, F_{12}^{p}, from Figure 7.6.2 will be used as an indicator of the number of slip events within the computational domain. The evolution of F_{12}^{p} as a function of the number of cycles plotted in Figure 7.6.4, shows that γ' distribution 1 recorded a larger number of slip events than distribution 3. It follows that kinematic back stresses will be greatest for distribution 1, thereby resulting in a large shift in the yield surface for this case than that predicted for distribution 3, see Figure 7.6.1a.

7.6.2 Case 2 - 800°C distribution 1 forward and reverse load

Another case to examine the differences in shear events are forward and reverse loads of $\Delta\epsilon = 1.2\%$ for 800°C distribution 1 which created very different looking flow stress curves in Figure 7.3.4. Due to the amount of overlap of the fatigue loops, the first and last cycles from were extracted to show the cyclic drift of the fatigue loops in Figure 7.6.5. For the forward simulation there is very little change from the first to last cycle, almost matching

when comparing at the yield on the second forward load of the first cycle. Looking at the shear events in the domain provided an insight into what is causing these changes in the fatigue behaviour for an identical γ' distribution.

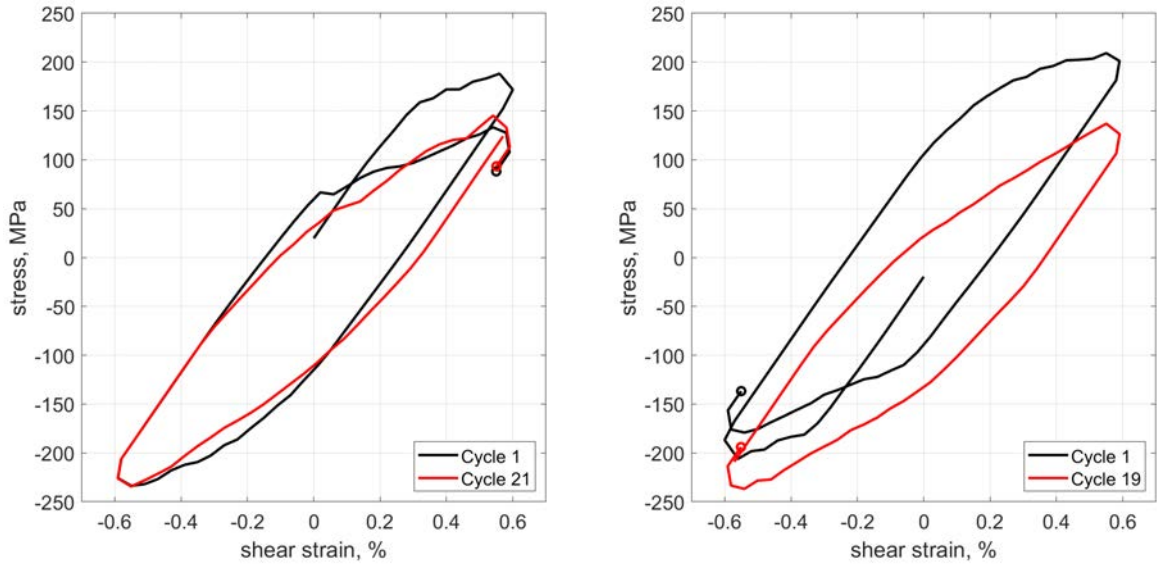

(a) Forward (b) Reverse

Figure 7.6.5: First and last cycle for distributions 1 at 800°C at strain range $\Delta\epsilon = 1.2\%$ comparing initial forward and reverse load directions

Firstly the plastic deformation gradient maps look different at the end of the first loading cycle, Figure 7.6.6a, as the forward map was taken at 90 MPa and reverse map, Figure 7.6.7a, was taken near the peak negative stress at -190 y =MPa. The forward simulation has generated dislocations creating more positive deformation gradients, and the reverse experiencing more negative shear. At the end of the last cycle both deformation gradient maps, Figure 7.6.6b and Figure 7.6.7b, look very similar with shear visible across the domain at the same y positions and little to no shear at the same positions (3.2, 2.4 and 0.6 μm). The magnitude of shear is larger across the full length of the domain in Figure 7.6.7b but the cyclic drift lowering the average stress must stem from regular imbalances in the shear happening between each loading cycle. The maps in Figure 7.6.6 were taken at a near identical

stress and strain values 17 loading cycles apart.

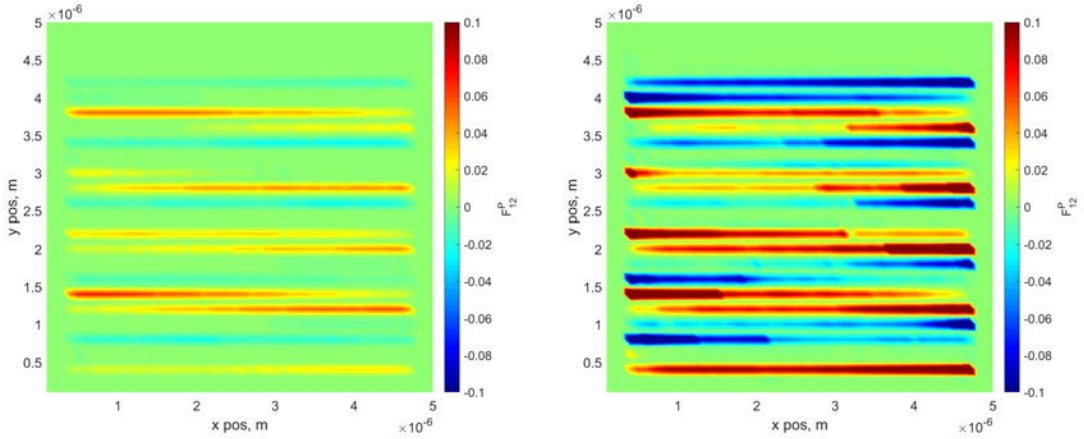

(a) Cycle 1 (b) Cycle 18

Figure 7.6.6: Deformation gradient component, F^p, for 800°C distributions 1 for strain range $\Delta\epsilon = 1.2\%$ for initial forward load fatigue

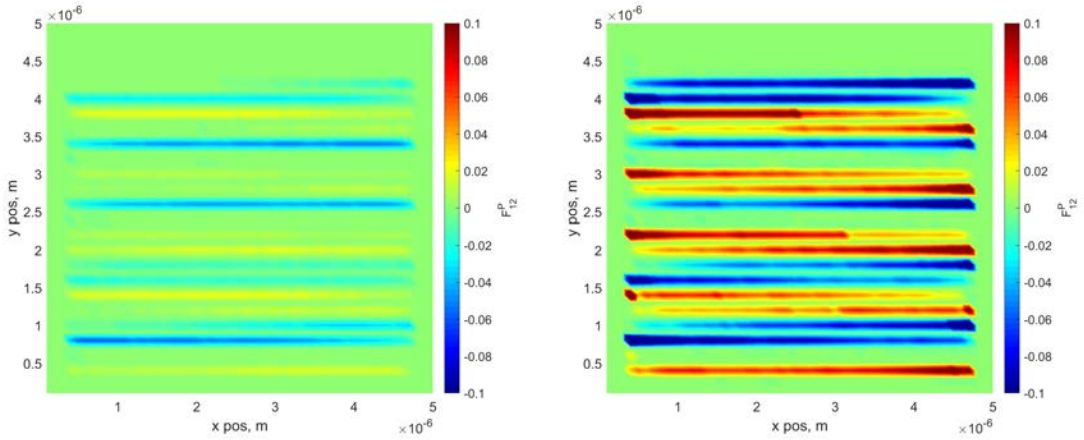

(a) Cycle 1 (b) Cycle 17

Figure 7.6.7: Deformation gradient component, F^p, for 800°C distributions 1 for strain range $\Delta\epsilon = 1.2\%$ for initial reverse load fatigue

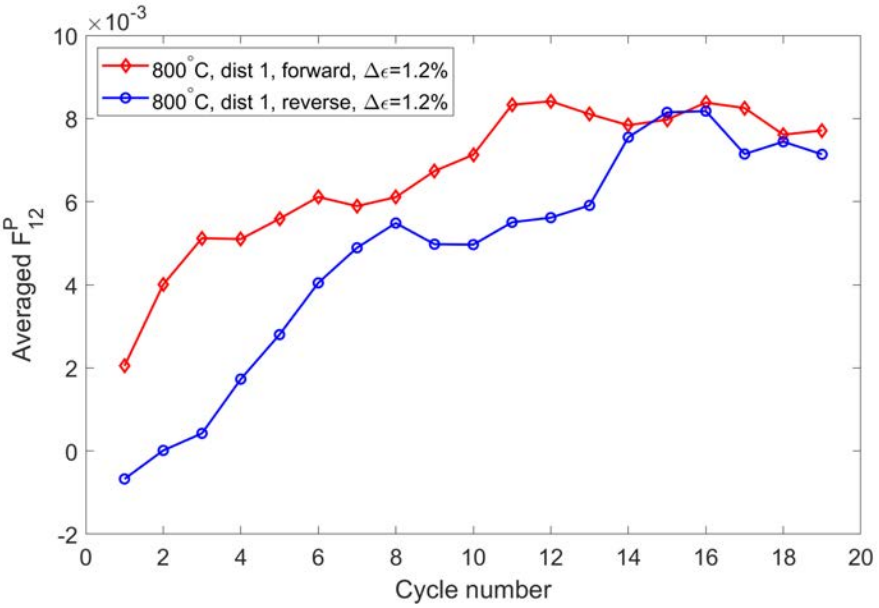

Figure 7.6.8: Average F^p across the whole domain per cycle for distributions 1, forward and reverse at 800°C for $\Delta\epsilon = 1.2\%$

In summary the plastic deformation maps reveal how the final cycles for these two simulations in Figure 7.6.5 have differences between their first and last stress-strain fatigue loops. The accumulation of shear events per cycle in Figure 7.6.8 varied within the same distribution due to the initial load direction. The first cycle sees on average more negative plastic deformation than positive for the reverse simulation. After this both forward and reverse simulations show an increase in positive shear events, the reverse simulation seeing a larger change per cycle causing the increased cyclic drift relative to the forward simulation. Observed different amounts of accumulated plasticity on different slip bands for the distributions at each temperature; linked to dislocations and the γ' interactions. In the current framework, ratchetting may be explained in terms of this asymmetry in activation of sources on load reversal due to interactions with the microstructure. It has been shown the hysteresis loops shift downwards slightly in stress with the increase of the number of cycles in LCF tests but after an initial hardening of the domain [96].

The plots of plastic strain range and stress range per cycle indicate the differences in the amount of localized plastic flow taking place with each load. The change in these values represents the ability to absorb the irreversible deformation energy. The 700°C and 750°C microstructures demonstrated a softening over the first 10 cycles tending towards a steady state fatigue loop. Similar Nickel-based alloys tend to present hardening at room temperature and softening at elevated temperatures of approximately 700°C [93]. Bimodal microstructures are known to show more resistance to cyclic softening at high temperatures, these tests have shown initial hardening followed by softening late rinto the fatigue test [98, 99]. Cyclic softening has been attributed to dislocations cutting orderly γ' precipitates in associated with the development of heterogeneous slip bands by shearing the hardening phase from repeated dislocation cutting [93, 96].

It was expected that the higher temperature simulations (lower volume fraction) to produce much softer flow stress curves yielding at lower stresses. An increase in temperature leads to a reduction of the strength and dissolution of tertiary γ' precipitates and induction of the cyclic-slip irreversibility, resulting in microstructural damage of the alloy [99]. In the FDM fatigue model the increased space in the γ matrix and the absence of tertiary particles had significant effect on dislocations mobility causing large shear events. More dislocations were generated in these 800°C microstructures, as the dislocations could travel more easily once generated due to reduced back-stress acting on the sources.

The FDM model currently only simulates for parallel edge dislocations for a single slip system limiting the number of dislocation interaction events occurring. The motion of dislocations on other slip systems play a large role in dislocation structure formation. The introduction of new rotated internal stress field contributions from a new slip system would greatly impact mobility. This would allow cross cross slip, formation of sessile dislocations similar to Lomer-Cotrell locks [15] and create more complicated dislocation stress fields.

Cyclic hardening is attributed to increase in the dislocation density, extensive cross-slip at higher temperatures, and the formation of complicated networks, all of which restrict the motion of mobile dislocations [16,99]. Only the 800° microstructures displayed some hardening after an initial softening which must have been due to the increasing dislocation density creating back-stresses impacting the mobility of dislocations more in later cycles.

Chapter 8

Conclusion

The objective of this study was to understand the influence of microstructure variations of the flow stress behaviour of γ' strengthened Nickel-based superalloys subject to elevated temperature fatigue loading conditions. A computational material modelling approach has been developed that explicitly models the transport of dislocation within a crystallographic grain and accounts for dislocation-microstructure interactions. The governing field equations for the dislocation field are based on a field dislocation mechanics (FDM) theory proposed by Basoalto [80], which is able to simulate the development of dislocation slip bands. The governing equation for transport of the dislocation field is an elliptical partial differential equation (3.2.17), which was solved using an implicit upwind Gauss-Seidel finite difference scheme. The FDM numerical solver was coupled with the commercial finite element solver ABAQUS to predict the evolution of micromechanical fields within a Nickel-based superalloy microstructure.

An in-house discrete dislocation dynamics (DDD) code was used to determine the minimum size of the computational domain for which the proposed FDM equations may be used. By comparing DDD pile-up simulations with analytical solutions a minimum grid spacing limit to describe a continuous dislocation density field was determined at $dx = 50$nm. It was

found the analytical solutions of a continuous dislocation distribution broke down for domain size, L, less than 900nm, where it deviated from discrete dislocation positions. Below this limit the continuous description of the dislocation field cannot be used. DDD simulations were also used to characterise a power relation between the annihilation rate, $\dot{A}^{-}(\boldsymbol{x}, t)$ and the product of the dislocation densities, $\rho^{+}(\boldsymbol{x}, t)\rho^{-}(\boldsymbol{x}, t)$ in Equation (5.4.7) for interaction of opposite sign dislocations in the continuum model. The transport equation for the continuous dislocation field was solved and accurately matched the analytical solutions for pile-up distributions, given by Equation (2.2.4) and Equation (2.2.5), for a single slip plane. This verified the velocity field calculated from the FDM theory, and gave consistent mobility and pile-up behaviour for the dislocation field. Unlike previous pile-up comparisons for other continuum models [79] the dislocation density was generated from sources rather than advecting an initial dislocation distribution.

Chapter 6 considered stochastic stress fluctuations associated with spatial arrangements of individual dislocations which cannot be accounted for directly a a field formulation of dislocation dynamics. The local stress fluctuations were obtained from DDD simulations and were found to be by the Gaussian probability distribution function, given by Equation (6.2.3). These stress fluctuations were then translated into a fluctuation in the dislocation force per unit length, which was used to calculate the dislocation velocities required to solve Equation (6.2.4). Simulations of the flow stress under uniaxial loading based on the stochastic FDM model were found to have little effect when compared to solutions without the fluctuation force term. The average absolute difference in stress for the stochastic model was around 5 MPa for the 30% volume fraction microstructure and 3 MPa for the 33% microstructure, for both single sign and mixed sign dislocations. Thus these local stress fluctuation terms were omitted to focus on the influence of the microstructure for the fatigue simulations. The FDM model showed the formation of slip bands through the unimodal particle distributions generating different plastic response measured by the flow stress, the lower volume fraction of

secondary γ' particles yielding at lower stress. Slip band development showed that the yield occurs when there is sufficient stress for slip bands to shear the γ' particles across the full domain length. This yield is preceded by a micro-yield where the dislocations first generate but quickly pile-up behind obstacles. The negative dislocation population lowered the yield stress as more γ' particles were sheared simultaneously, reducing the linear hardening rates in comparison to the simulations with only positive dislocations.

The FDM fatigue simulations successfully captured differences in the flow stress behaviour for the temperature dependant γ' distributions. Despite the short number of cycles simulated the FDM fatigue analysis indicated the stress range, $\Delta\sigma$, and the plastic strain range $\Delta\epsilon_p$, were both converging quickly to a steady-state fatigue loop for the 700°C and 750°C distributions. The FDM simulations predict more localised deformation within the unimodal distributions at 800°C, and the high volume fraction bi-modal distributions at 700°C had the least dislocation shear events at this early stage of fatigue.

Fatigue behaviour was found to be directly correlated with dislocation interaction with the γ' distributions. Bauschinger effects were predicted showing the reduction in yield stress on reversal of the load direction due to the accumulation of dislocations with each loading cycle. Asymmetry in slip events observed on load reversal influence yield dependant on load direction. Slip bands forming on the forward load developed differently to slip bands generated during reverse load due to the γ' distribution. The differences in the number of slip events on load reversal influence yield. The FDM model predicted flow response differences with temperature dependent microstructure, the lower volume fraction distributions exhibiting more plastic deformation due to increased dislocation mobility and magnitude of shear events due to increased average spacing between particles and reduced line tension. Variation of flow behaviour was observed between distributions at each temperature, the heterogeneous distributions of γ' particles, which mathematically have the same cutting stress

and dislocation line tension, effecting dislocation mobility and slip band formation. This displayed a scatter of predicted fatigue behaviour at each temperature due to differences in slip events demonstrating the fidelity of the model. The 800°C particle distributions had the largest plastic strain range and scatter in fatigue behaviour, a result of having no tertiary γ' particles increasing dislocation mobility and allowing larger shear events to occur between the low volume fraction secondary γ' particles.

8.1 Future work

The approach has been successfully simulated the evolution of slip bands and their interactions with γ' particle dispersions representative of a Nickel-based superalloy. However, there is potential for further development to better capture the physics of deformation and fatigue using this FDM theory. Further simulations of more heterogeneous γ' particle dispersions at each temperature would give better averages of scatter of predicted properties for associated particle radii and volume fractions. The simulations are currently limited by the stable yet slow finite differencing method, which limits the number of loading cycles which can simulated within available HPC resource limit. The current simulations could be set-up to be restarted from their last ABAQUS restart file to observe how fatigue behaviour continues to develop. Alternatively developing a new numerical method to improve the efficiency of the FDM calculations would help complete more loading cycles and increase the size of the simulation domain to start simulating larger or multiple neighbouring grains for more polycrystalline like simulations.

The next major development step is to introduce another intersecting {1 1 1} slip system to promote cross-slip and formation of dislocation junctions accounting for more accurate dislocation behaviour. The challenge presented here is how to introduce a second slip system at an appropriate angle when the finite difference method used to update the dislocation

density is restricted to estimates in the direction of the grid axis. Cross-slip would induce the widening of slip bands, and the formation sessile dislocations would contribute to dislocation forest interactions and an initial hardening of the simulation domain. The addition of a rotated slip system will introduce the rotated stress fields of the dislocation field on the second slip system and potentially promote dislocation patterning.

The shear loading scenario applied to the finite element mesh is an idealised scenario. For a polycrystal the boundary effects would differ with the surrounding grains. Some initial tests have been carried out to see the effect of boundary conditions on fatigue.

8.1.1 Boundary conditions

The FDM was designed for use in a closed domain with impenetrable boundaries to be representative of a single grain in a polycrystal. Note that in the pure shear set up this is not ideal representation as the boundary conditions experienced by grains within a polycrystal thus a method is required to improve this. To handle more complex boundary conditions sub-modelling approach is proposed. This approach involves solving two boundary-value problems: that for the global configuration and the grain (sub-model). This is illustrated in Figure 8.1.1. Then another for a contained sub-domain which will align with the FDM domain. Deformation of the global model will result in complex boundary conditions on the sub-model that are more representative of those found in the deformation of real materials.

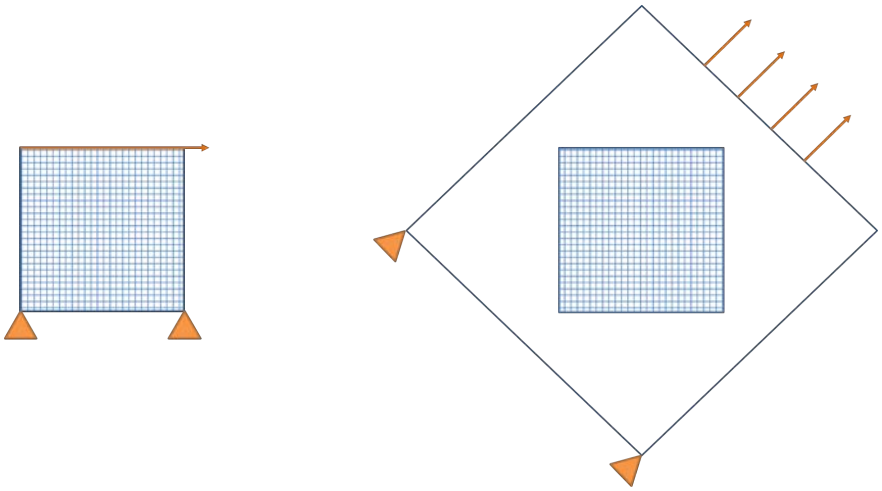

Figure 8.1.1: Comparison of fatigue loading conditions with pure shear (left) and tension sub-model (right)

The global domain was oriented at 45° to the sub-model to resolve the stress created under tension in the slip direction. The difference in stress acting on the slip plane influenced generation at dislocation sources and dislocation velocity. The loading amplitude applied to the global tension model, which was applied to the shear model, resolved a larger strain range in the sub-model domain in Figure 8.1.2. Both the tension and shear simulations exhibit the same decrease in range between the peak stresses, with a large drop in the maximum peak stress in the first few cycles. The plastic strain differs however with 800°C having the smallest plastic strain range and 750°C the largest, see Figure 8.1.3, for the small number of fatigue cycles simulated. There is a significant impact due to the boundary conditions on the model and presents opportunity to explore further. The sub-modelling technique also gives the ability to rotate domain relative to the load direction which will prove very useful in future simulations for this research.

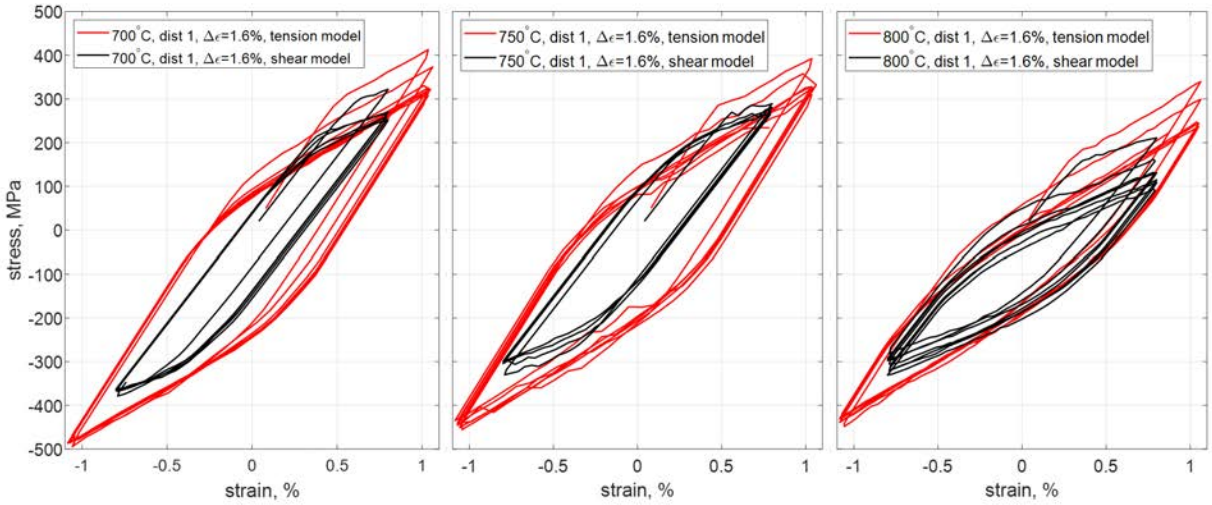

Figure 8.1.2: Tension and shear stress strain comparison for applied loading amplitude $\Delta\epsilon = 1.6\%$. Distribution 1 for each temperature.

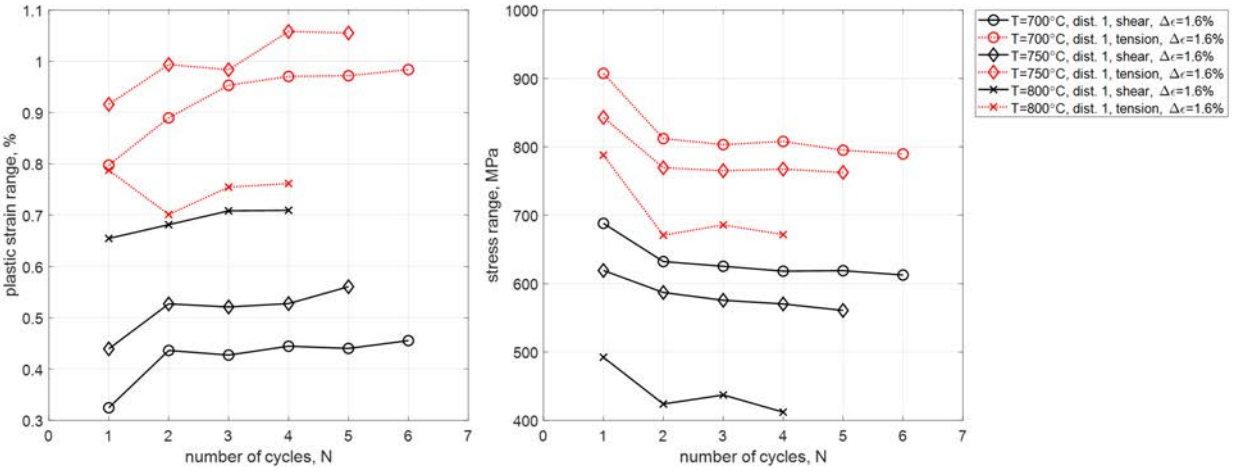

Figure 8.1.3: Tension and shear comparison of plastic strain range (left) and stress range (right). Distribution 1 for each temperature.

References

[1] J. Nye, "Some geometrical relations in dislocated crystals," *Acta Metallurgica*, vol. 1, pp. 153–162, mar 1953.

[2] J. Hirth and J. Lothe, *Theory of Dislocations*. Krieger Publishing Company, 1982.

[3] M. McLean, G. A. Webster, F. R. N. Nabarro, and A. Cottrell, "Nickel-Base Superalloys: Current Status and Potential [and Discussion]," *Philosophical Transactions: Physical Sciences and Engineering*, vol. 351, no. 1697, pp. 419–433, 1995.

[4] R. Royce, *The Jet Engine*. Wiley, 2015.

[5] S. Suresh, *Fatigue of Materials*. Cambridge solid state science series, Cambridge University Press, 1998.

[6] R. Reed, *The Superalloys: Fundamentals and Applications*. Cambridge University Press, 2006.

[7] A. W. Thompson and W. A. Backofen, "The effect of grain size on fatigue," *Acta Metallurgica*, vol. 19, no. 7, pp. 597–606, 1971.

[8] K. S. Chan, "Roles of microstructure in fatigue crack initiation," *International Journal of Fatigue*, vol. 32, pp. 1428–1447, sep 2010.

[9] H. Flower, *High Performance Materials in Aerospace*. Springer Netherlands, 2012.

[10] M. Segersäll, *Nickel-Based Single-Crystal Superalloys - the crystal orientation influence on high temperature properties*. PhD dissertation, Department of Management and Engineering, Linköping University, 3 2013.

[11] M. Bache, J. O'Hanlon, D. Child, and M. Hardy, "High temperature fatigue behaviour in an advanced nickel based superalloy: The effects of oxidation and stress relaxation at notches," *Theoretical and Applied Fracture Mechanics*, vol. 84, pp. 64–71, aug 2016.

[12] A. J. Goodfellow, "Strengthening mechanisms in polycrystalline nickel-based superalloys," *Materials Science and Technology*, vol. 34, no. 15, pp. 1793–1808, 2018.

[13] J. Coakley, H. Basoalto, and D. Dye, "Coarsening of a multimodal nickel-base superalloy," *Acta Materialia*, vol. 58, pp. 4019–4028, jun 2010.

[14] M. J. Anderson, F. Schulz, Y. Lu, H. S. Kitaguchi, P. Bowen, C. Argyrakis, and H. C. Basoalto, "On the modelling of precipitation kinetics in a turbine disc nickel based superalloy," *Acta Materialia*, vol. 191, pp. 81–100, 2020.

[15] D. Hull and D. Bacon, *Introduction to Dislocations*. Elsevier Science, 2001.

[16] A. Pineau and S. D. Antolovich, "High temperature fatigue of nickel-base superalloys A review with special emphasis on deformation modes and oxidation," *Engineering Failure Analysis*, vol. 16, pp. 2668–2697, dec 2009.

[17] F. Nabarro and J. Hirth, *Dislocations in Solids*. No. v. 13 in DIS/Dislocations in Solids Series, Elsevier Science, 2007.

[18] T. Mura, *Micromechanics of Defects in Solids*. Mechanics of Elastic and Inelastic Solids, Springer Netherlands, 1987.

[19] J. Eshelby, X. Markenscoff, and A. Gupta, *Collected works of J.D. Eshelby: the mechanics of defects and inhomogeneities*. Solid mechanics and its applications, Springer, 2006.

[20] G. Leibfried, "Verteilung von Versetzungen im statischen Gleichgewicht," *Zeitschrift für Physik*, vol. 130, no. 2, pp. 214–226, 1951.

[21] B. M. Grant, E. M. Francis, J. Q. da Fonseca, M. Preuss, and M. R. Daymond, "The effect of size and alloy chemistry on dynamic strain ageing in advanced polycrystalline nickel base superalloys," *Materials Science and Engineering: A*, vol. 573, no. 0, pp. 54 – 61, 2013.

[22] L. M. Brown, "Dislocation pile-ups, slip-bands, ellipsoids, and cracks," *Materials Science and Engineering: A*, vol. 400-401, pp. 2–6, jul 2005.

[23] M. D. Sangid, "The physics of fatigue crack initiation," *International Journal of Fatigue*, vol. 57, pp. 58–72, Dec. 2013.

[24] P. Lukáš and L. Kunz, "Role of persistent slip bands in fatigue," *Philosophical Magazine*, vol. 84, no. 3-5, pp. 317–330, 2004.

[25] M. D. Sangid, H. J. Maier, and H. Sehitoglu, "A physically based fatigue model for prediction of crack initiation from persistent slip bands in polycrystals," *Acta Materialia*, vol. 59, pp. 328–341, Jan. 2011.

[26] K. Tanaka and T. Mura, "A dislocation model for fatigue crack initiation," vol. 48, 03 1981.

[27] A. N. Stroh, "The Formation of Cracks as a Result of Plastic Flow," vol. 223, no. 1154, pp. 404–414, 1954.

[28] A. N. Stroh, "The Formation of Cracks in Plastic Flow. II," vol. 246, no. 1247, pp. 539–555, 1955.

[29] S. Manson, *Behavior of Materials Under Conditions of Thermal Stress*. National Advisory Committee for Aeronautics, 1953.

[30] H. Mughrabi, "Microstructural mechanisms of cyclic deformation, fatigue crack initiation and early crack growth," *Philosophical Transactions of the Royal Society A: Mathematical, Physical and Engineering Sciences*, vol. 373, no. 2038, 2015.

[31] Y. Xiang and J. Vlassak, "Bauschinger effect in thin metal films," *Scripta Materialia*, vol. 53, pp. 177–182, jul 2005.

[32] J. Lemaitre and J. Chaboche, *Mechanics of Solid Materials*. Cambridge University Press, 1994.

[33] T. Mura, "A theory of fatigue crack initiation," *Materials Science and Engineering: A*, vol. 176, pp. 61–70, mar 1994.

[34] H. Mughrabi, "Microstructural fatigue mechanisms: Cyclic slip irreversibility, crack initiation, non-linear elastic damage analysis," *International Journal of Fatigue*, vol. 57, pp. 2–8, dec 2013.

[35] M. D. Sangid, H. J. Maier, and H. Sehitoglu, "The role of grain boundaries on fatigue crack initiation An energy approach," *International Journal of Plasticity*, vol. 27, pp. 801–821, May 2011.

[36] S.-T. Tu and X.-C. Zhang, "Fatigue Crack Initiation Mechanisms," *Reference Module in Materials Science and Materials Engineering*, no. December, pp. 0–23, 2016.

[37] B. Larrouy, P. Villechaise, J. Cormier, and O. Berteaux, "Grain boundaryslip bands interactions: Impact on the fatigue crack initiation in a polycrystalline forged Ni-based superalloy," *Acta Materialia*, vol. 99, pp. 325–336, oct 2015.

[38] L. Llanes and C. Laird, "The role of annealing twin boundaries in the cyclic deformation of f.c.c. materials," *Materials Science and Engineering: A*, vol. 157, pp. 21–27, sep 1992.

[39] S. Qu, P. Zhang, S. Wu, Q. Zang, and Z. Zhang, "Twin boundaries: Strong or weak?," *Scripta Materialia*, vol. 59, pp. 1131–1134, Nov. 2008.

[40] C. Blochwitz and W. Tirschler, "Twin boundaries as crack nucleation sites," *Crystal Research and Technology*, vol. 40, pp. 32–41, Jan. 2005.

[41] S. Brinckmann and E. Van der Giessen, "Towards understanding fatigue crack initiation: a discrete dislocation dynamics study," *Proceedings of ICM9, ...*, 2003.

[42] H. Mughrabi, R. Wang, K. Differt, and C. Fatigue, "Fatigue Crack Initiation by Cyclic Slip Irreversibilities in High-Cycle Fatigue," 1983.

[43] M. D. Sangid, T. Ezaz, H. Sehitoglu, and I. M. Robertson, "Energy of slip transmission and nucleation at grain boundaries," *Acta Materialia*, vol. 59, pp. 283–296, jan 2011.

[44] M. D. Sangid, H. Sehitoglu, H. J. Maier, and T. Niendorf, "Grain boundary characterization and energetics of superalloys," *Materials Science and Engineering: A*, vol. 527, pp. 7115–7125, oct 2010.

[45] A. Heinz and P. Neumann, "Crack initiation during high cycle fatigue of an austenitic steel," *Acta Metallurgica et Materialia*, vol. 38, pp. 1933–1940, oct 1990.

[46] M. Shenoy, J. Zhang, and D. McDowell, "Estimating fatigue sensitivity to polycrystalline ni-base superalloy microstructures using a computational approach," *Fatigue & Fracture of Engineering Materials & Structures*, vol. 30, no. 10, pp. 889–904.

[47] M. Shenoy, Y. Tjiptowidjojo, and D. McDowell, "Microstructure-sensitive modeling of polycrystalline IN 100," *International Journal of Plasticity*, vol. 24, pp. 1694–1730, oct 2008.

[48] A. Manonukul and F. P. E. Dunne, "High– and low–cycle fatigue crack initiation using polycrystal plasticity," *Proceedings of the Royal Society of London A: Mathematical, Physical and Engineering Sciences*, vol. 460, no. 2047, pp. 1881–1903, 2004.

[49] A. M. Kosevich, "Dynamical Theory of Dislocations," *Soviet Physics Uspekhi*, vol. 7, no. 6, p. 837, 1965.

[50] D. Walgraef and E. C. Aifantis, "On the formation and stability of dislocation patternsI: One-dimensional considerations," *International Journal of Engineering Science*, vol. 23, pp. 1351–1358, Jan. 1985.

[51] D. Walgraef and E. C. Aifantis, "On the formation and stability of dislocation patternsII: Two-dimensional considerations," *International Journal of Engineering Science*, vol. 23, pp. 1359–1364, Jan. 1985.

[52] D. Walgraef and E. C. Aifantis, "On the formation and stability of dislocation patternsIII: Three-dimensional considerations," *International Journal of Engineering Science*, vol. 23, pp. 1365–1372, jan 1985.

[53] I. Groma and P. Balogh, "Link between the individual and continuum approaches of the description of the collective behavior of dislocations," *Materials Science and Engineering: A*, 1997.

[54] I. Groma, B. Bakó, and V. D. Merve, "Stochastic approach for modeling dislocation patterning," *Physical Review B*, vol. 60, no. 1, pp. 122–127, 1999.

[55] I. Groma and B. Bakó, "Linking different scales: discrete, self-consistent field, and stochastic dislocation dynamics," *Materials Science and Engineering: A*, vol. 309-310, pp. 356–359, July 2001.

[56] T. Hochrainer, S. Sandfeld, M. Zaiser, and P. Gumbsch, "Continuum dislocation dynamics: Towards a physical theory of crystal plasticity," *Journal of the Mechanics and Physics of Solids*, vol. 63, pp. 167–178, Feb. 2014.

[57] A. Acharya, "A model of crystal plasticity based on the theory of continuously distributed dislocations," *Journal of the Mechanics and Physics of Solids*, vol. 49, pp. 761–784, Apr. 2001.

[58] S. Sandfeld, T. Hochrainer, M. Zaiser, and P. Gumbsch, "Continuum modeling of dislocation plasticity: Theory, numerical implementation, and validation by discrete dislocation simulations," *Journal of Materials Research*, vol. 26, pp. 623–632, mar 2011.

[59] E. Kröner, "Berechnung der elastischen konstanten des vielkristalls aus den konstanten des einkristalls," *Zeitschrift für Physik*, vol. 151, pp. 504–518, Aug 1958.

[60] P. Gumbsch and R. Pippan, *Multiscale Modelling of Plasticity and Fracture by Means of Dislocation Mechanics*. CISM International Centre for Mechanical Sciences, Springer Vienna, 2011.

[61] S. Sandfeld, T. Hochrainer, P. Gumbsch, and M. Zaiser, "Numerical implementation of a 3D continuum theory of dislocation dynamics and application to micro-bending," *Philosophical Magazine*, vol. 90, pp. 3697–3728, sep 2010.

[62] D. Walgraef and E. C. Aifantis, "Dislocation patterning in fatigued metals as a result of dynamical instabilities," *Journal of Applied Physics*, vol. 58, no. 2, p. 688, 1985.

[63] E. Aifantis, "Pattern formation in plasticity," *International Journal of Engineering Science*, vol. 33, pp. 2161–2178, Dec. 1995.

[64] G. Ananthakrishna, "Current theoretical approaches to collective behavior of dislocations," *Physics Reports*, vol. 440, pp. 113–259, Mar. 2007.

[65] P. Hähner, "Statistical mechanics approach to dislocation cell patterning," *Scripta Materialia*, vol. 47, pp. 705–711, nov 2002.

[66] P. Hähner, "A theory of dislocation cell formation based on stochastic dislocation dynamics," *Acta Materialia*, vol. 44, no. 6, pp. 2345–2352, 1996.

[67] P. Hähner, "On the foundations of stochastic dislocation dynamics," *Applied Physics A Materials Science and Processing*, vol. 62, no. 5, pp. 473–481, 1996.

[68] I. Groma and B. Bakó, "Probability distribution of internal stresses in parallel straight dislocation systems," *Physical Review B*, vol. 58, no. 6, pp. 2969–2974, 1998.

[69] I. Groma and P. Balogh, "Investigation of dislocation pattern formation in a two-dimensional self-consistent field approximation," *Acta Materialia*, vol. 47, pp. 3647–3654, Oct. 1999.

[70] I. Groma, F. Csikor, and M. Zaiser, "Spatial correlations and higher-order gradient terms in a continuum description of dislocation dynamics," *Acta Materialia*, vol. 51, pp. 1271–1281, Mar. 2003.

[71] S. Chandrasekhar, "Stochastic Problems in Physics and Astronomy," *Reviews of Modern Physics*, vol. 15, pp. 1–89, Jan. 1943.

[72] S. Yefimov and E. Van der Giessen, "Multiple slip in a strain-gradient plasticity model motivated by a statistical-mechanics description of dislocations," *International Journal of Solids and Structures*, vol. 42, pp. 3375–3394, jun 2004.

[73] M. Zaiser, M. C. Miguel, and I. Groma, "Statistical dynamics of dislocation systems: The influence of dislocation-dislocation correlations," *Physical Review B - Condensed Matter and Materials Physics*, vol. 64, no. 22, pp. 2241021–2241029, 2001.

[74] S. Yefimov, I. Groma, and E. van der Giessen, "A comparison of a statistical-mechanics based plasticity model with discrete dislocation plasticity calculations," *Journal of the Mechanics and Physics of Solids*, vol. 52, pp. 279–300, feb 2003.

[75] A. Acharya, "Driving forces and boundary conditions in continuum dislocation mechanics," *Proceedings of the Royal Society A: Mathematical, Physical and Engineering Sciences*, vol. 459, no. 2034, pp. 1343–1363, 2003.

[76] A. Acharya, "From dislocation motion to an additive velocity gradient decomposition , and some simple models of dislocation dynamics," pp. 1–17, 2014.

[77] A. Roy and A. Acharya, "Finite element approximation of field dislocation mechanics," *Journal of the Mechanics and Physics of Solids*, vol. 53, pp. 143–170, jan 2005.

[78] T. Hochrainer, M. Zaiser, and P. Gumbsch, "A three-dimensional continuum theory of dislocation systems: kinematics and mean-field formulation," *Philosophical Magazine*, vol. 87, no. 8-9, pp. 1261–1282, 2007.

[79] K. Schulz, D. Dickel, S. Schmitt, S. Sandfeld, D. Weygand, and P. Gumbsch, "Analysis of dislocation pile-ups using a dislocation-based continuum theory," *Modelling and Simulation in Materials Science and Engineering*, vol. 22, no. 2, p. 25008, 2014.

[80] H. Basoalto and J. Little, "On plasticity of two-phase alloys as emergent behaviour." pre-submission, 2019.

[81] A. Khan and S. Huang, *Continuum Theory of Plasticity*. Wiley-Interscience publication, Wiley, 1995.

[82] H. Basoalto, "On a heterogeneous theory of crystal plasticity," Report P-41, PRISMM, Univeristy of Birmingham, 2016. PRISMM report.

[83] F. Dunne and N. Petrinic, *Introduction to Computational Plasticity*. Oxford series on materials modelling, OUP Oxford, 2005.

[84] S. Mazumder, *Numerical Methods for Partial Differential Equations: Finite Difference and Finite Volume Methods*. Elsevier Science, 2015.

[85] F. Schulz, H. Y. Li, H. Kitaguchi, D. Child, S. Williams, and P. Bowen, "Influence of Tertiary Gamma Prime (γ) Size Evolution on Dwell Fatigue Crack Growth Behavior in CG RR1000," *Metallurgical and Materials Transactions A: Physical Metallurgy and Materials Science*, vol. 49, no. 9, pp. 3874–3884, 2018.

[86] L. Di Masso, B. Coluzzi, and F. M. Mazzolai, "Ultrasonic investigation of CMSX-6 superalloy at low and high temperatures," *Journal De Physique. IV : JP*, vol. 6, no. 8, 1996.

[87] S. V. Prikhodko, J. D. Carnes, D. G. Isaak, H. Yang, and A. J. Ardell, "Temperature and composition dependence of the elastic constants of Ni3Al," *Metallurgical and Materials Transactions A: Physical Metallurgy and Materials Science*, vol. 30, no. 9, pp. 2403–2408, 1999.

[88] "Determination of the high temperature elastic properties and diffraction elastic constants of Ni-base superalloys," *Materials and Design*, vol. 89, pp. 856–863, 2016.

[89] N. Tian, S. Tian, H. Yu, Y. Li, and X. Meng, "Microstructure and Creep Behavior of a Directional Solidification Nickel-based Superalloy," *High Temperature Materials and Processes*, vol. 34, no. 4, pp. 299–309, 2015.

[90] V. Deshpande, A. Needleman, and E. Van der Giessen, "Dislocation dynamics is chaotic," *Scripta Materialia*, vol. 45, pp. 1047–1053, nov 2001.

[91] E. Van der Giessen and A. Needleman, "Discrete dislocation plasticity: a simple planar model," *Modelling and Simulation in ...*, vol. 689, 1995.

[92] S. D. Antolovich, "Microstructural aspects of fatigue in nickel-base superalloys," *Phil. Trans. R. Soc. A*, vol. 373, p. 20140128, 2015.

[93] P. Phillips, R. Unocic, and M. Mills, "Low cycle fatigue of a polycrystalline Ni-based superalloy: Deformation substructure analysis," *International Journal of Fatigue*, vol. 57, pp. 50–57, dec 2013.

[94] K. Prasad, R. Sarkar, P. Ghosal, V. Kumar, and M. Sundararaman, "High temperature low cycle fatigue deformation behaviour of forged IN 718 superalloy turbine disc," *Materials Science and Engineering A*, vol. 568, no. April, pp. 239–245, 2013.

[95] C. Stöcker, M. Zimmermann, H.-J. Christ, Z.-L. Zhan, C. Cornet, L. Zhao, M. Hardy, and J. Tong, "Microstructural characterisation and constitutive behaviour of alloy RR1000 under fatigue and creepfatigue loading conditions," *Materials Science and Engineering: A*, vol. 518, pp. 27–34, aug 2009.

[96] P. Zhang, Q. Zhu, G. Chen, H. Qin, and C. Wang, "Fatigue Behavior and Life Prediction Model of a Nickel-Base Superalloy under Different Strain Conditions," *Materials Transactions*, vol. 57, no. 1, pp. 25–32, 2016.

[97] J. Miao, T. M. Pollock, and J. Wayne Jones, "Microstructural extremes and the transition from fatigue crack initiation to small crack growth in a polycrystalline nickel-base superalloy," *Acta Materialia*, vol. 60, pp. 2840–2854, apr 2012.

[98] M. Petrenec, K. Obrtlík, and J. Polák, "High Temperature Low Cycle Fatigue of Superalloys Inconel 713LC and Inconel 792-5A," *Key Engineering Materials*, vol. 348-349, no. May 2015, pp. 101–104, 2007.

[99] L. Zhang, L. G. Zhao, A. Roy, V. V. Silberschmidt, and G. McColvin, "Low-cycle fatigue of single crystal nickel-based superalloy mechanical testing and TEM characterisation," *Materials Science and Engineering A*, vol. 744, no. November 2018, pp. 538–547, 2019.